Alexander Gorski

Applications of polarized spectroscopy and matrix isolation techniques

Ph.D. thesis carried out under supervision of Professor dr. Jacek Waluk.

Department of Photochemistry and Spectroscopy, Institute of Physical Chemistry, Polish Academy of Sciences, Warsaw, Poland

Warsaw 2005

Mojemu promotorowi, Panu Profesorowi Jackowi Walukowi, składam serdeczne podziękowania za wskazanie interesującego tematu pracy oraz wszechstronną pomoc w trakcie jej wykonywania.

Pragnę także wyrazić swoją wdzięczność koleżankom i kolegom z zakładu, za wiele ciekawych dyskusji oraz za pomoc w trakcie pracy doświadczalnej. Z całego serca dziękuję również moim najbliższym i przyjaciołom za ich wsparcie.

Preface
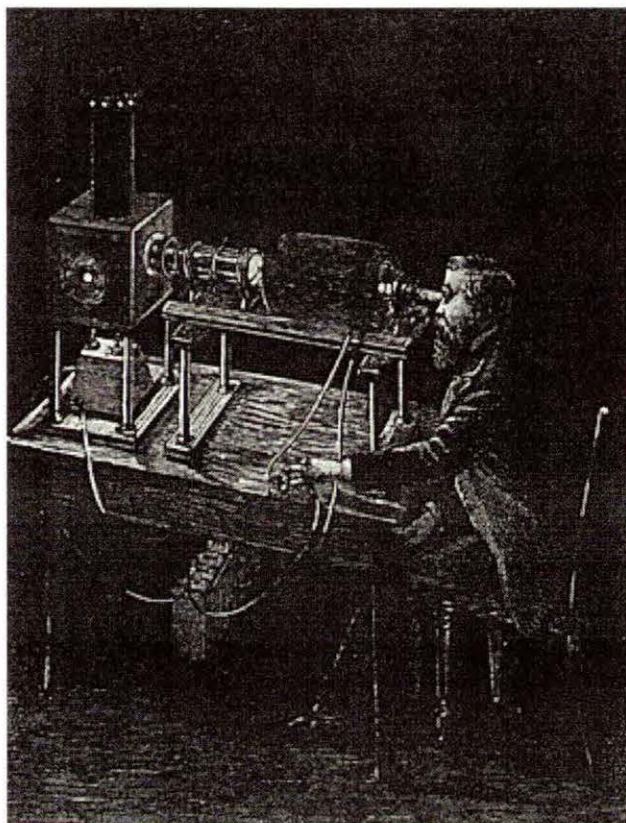
ФАРАДЕЙ (Faraday) Майкл (1791 - 1867), английский физик, основоположник современной концепции поля в электродинамике, автор ряда фундаментальных открытий, в том числе закона электромагнитной индукции, законов электролиза, явления вращения плоскости поляризации света в магнитном поле, один из первых исследователей воздействия магнитного поля на среды.

"Фарадей своим мысленным оком видел силовые линии, принизывающие все пространство. Там, где математики видели центры напряжения сил дальнодействия, Фарадей видел промежуточный агент. Где они не видели ничего, кроме расстояния, удовлетворяясь тем, что находили закон распределения сил, действующих на электрические флюиды, Фарадей искал сущность реальных явлений, протекающих в среде."

Д. К. Максвелл

Table of Contents

Acronyms and abbreviations

A_i, B_i, and C_i	Faraday terms of an i-th transition
B_1, B_2	Two high-energy electronic states in Platt's terminology
CD	Circular Dichroism
Corrphycene	2,3,6,7,11,12,17,18-octaethylcorrphycene
Cyclo[6]pyrrole	Dihydrogen[2,3,6,7,10,11,14,15,18,19,22,23,-dodecanethyl-[22]hexaphyrin(0.0.0.0.0.0)
Cyclo[7]pyrrole	Dihydrogen[2,3,6,7,10,11,14,15,18,19,22,23,26,27,-tetradecanethyl-[26]heptaphyrin(0.0.0.0.0.0.0)
Cyclo[8]pyrrole	Dihydrogen[2,7,10,15,18,23,26,31,-octaethyl-3,6,11,14,19,22,27,30-octamethyl-[30]octaphyrin(0.0.0.0.0.0.0.0)]
D_i	The dipole strength of an i-th transition
DHT	Double Hydrogen Transfer
FEMO	Free-electron molecular orbital
Hemiporphycene	2,3,6,7,11,12,16,17-octaethylhemiporphycene
HOMO	The highest occupied molecular orbitals
IS	16,20-dibutyl-2,3,6,7,10,11,15,21-octamethyl-[22]pentaphyrin(1.1.0.1.0)
L_1, L_2	Two low-energy electronic states in Platt's terminology
LD	Linear Dichroism
LCAO MO	Molecular orbitals as linear combination of atomic orbitals
LUMO	The lowest unoccupied molecular orbitals
MCD	Magnetic Circular Dichroism
MOIS	16,20-dibutyl-2,3,6,7,10,11,15,21-octamethyl-5-oxo-[22]pentaphyrin(1.1.1.0.0)
TD-DFT	Time-Dependent Density Functional Theory

Index of charts

Index of figures

Index of tables

Chapter 1. Literature Review

1.1. Introduction

Electronic Transition Dipole Moment

The theoretical description of the evolution in time of a quantum-mechanical system is obtained by solving the time-dependent Schrödinger equation:

$$\hat{H}\Psi = i\hbar\frac{\partial\Psi}{\partial t} \qquad (1.1)$$

where $\hat{H}$ is the Hamiltonian of the system and Ψ is the wavefunction. This equation is an analogue of the equation of motion in classical mechanics:

$$\vec{F} = m\vec{a} = m\frac{\partial^2\vec{S}(t)}{\partial t^2} \qquad (1.2)$$

The solution of the latter equation yields a trajectory of the particle, $\vec{S}(t)$, in other words, position of the particle at any moment of time. In the case of quantum mechanics, a solution is the wavefunction, which defines a probability of finding the particle at any point in space at any time.

In general, the states of a quantum-mechanical system can change in time in a very complicated manner. However, in the midst of all states, there are the so-called stationary states, whose wavefunctions change in a simple manner and the observable properties do not change in time. There is no time dependence in the Schrödinger equation for stationary states and the equation can be written as:

$$\hat{H}(\vec{q},\vec{Q})\Psi(\vec{q},\vec{Q}) = E\Psi(\vec{q},\vec{Q}) \qquad (1.3)$$

Both $\hat{H}(q,Q)$ and $\Psi(q,Q)$ depend on the electron coordinates represented by the vector $\vec{q}$ and the coordinates of the nuclei, depicted by the vector $\vec{Q}$. The solutions of the equation are wavefunctions and energies of the system, which are eigenfunctions and eigenvalues of the Schrödinger equation, respectively.

i. *Adiabatic Approximation*

The exact solution of the Schrödinger equation is known for a very simple system containing not more than three particles. Therefore, for systems that are more complicated the solution is possible after including some approximations. One of the more general of them is the *adiabatic approximation* based on separating the electron motion from motion of the nuclei. Consequently, in this approximation the stationary state wavefunction is written as:

$$\Psi_{j,v}(\vec{q},\vec{Q}) = \varphi_j(\vec{q},\vec{Q})\chi_{j,v}(\vec{Q}) \tag{1.4}$$

where j characterizes the electronic state and v describes the vibrational structure of that state.

The electronic wavefunction $\varphi_j(\vec{q},\vec{Q})$ depends on the electron coordinates and contains $\vec{Q}$ as a parameter. This wavefunction is an eigenfunction of the electronic Hamiltonian:

$$\hat{H}_{el}(\vec{q},\vec{Q}) = \hat{H}_{kin\_el} + \hat{V}_{el-nuc} + \hat{V}_{el-el} + \hat{V}_{nuc-nuc} \tag{1.5}$$

defined as an operator containing the potential energy of electrostatic electron-nuclear attraction, electron-electron and nuclear-nuclear repulsion, and the kinetic energy of the electrons. The solutions of the time-independent Schrödinger equation with the electronic Hamiltonian are wavefunctions $\varphi_j(\vec{q},\vec{Q})$ and energies $E_j(\vec{Q})$ representing a j-th electronic state for fixed nuclei positions $\vec{Q}$.

ii. *Born-Oppenheimer approximation*

The vibrational wavefunction $\chi_{j,v}(\vec{Q})$ depends on the nuclear coordinates. This wavefunction is an eigenfunction of a vibrational Hamiltonian:

$$\hat{H}_{vib}(j,\vec{Q}) = \hat{H}_{kin\_nuc} + \hat{E}_j^0(\vec{Q}) + \hat{H}_{jj}^{'}(\vec{Q}) \tag{1.6}$$

which includes the kinetic energy of the nuclei and the potential energy for the slow motion of the nuclei. The latter is represented by two parts, which describe the whole energy of the

system, $\hat{E}_j^0(\vec{Q}) + \hat{H}_{jj}'(\vec{Q})$, averaged over the fast electronic motion. The first term, $\hat{E}_j^0(\vec{Q})$, is the electronic energy obtained for a defined position of the nuclei. The second part, $\hat{H}_{jj}'(\vec{Q})$, is a small correction to the whole energy.

The next important approximation in quantum chemistry, known as *Born-Oppenheimer approximation*, is based on negligence of the small correction part $\hat{H}_{jj}'(\vec{Q})$. In the *Born-Oppenheimer approximation*, the solutions of time independent Schrödinger equation with vibrational Hamiltonian are wavefunctions $\chi_{j,v}(\vec{Q})$ and energies $E_{j,v}$, which describe nuclei motion in the *j*-th electronic state.

The electric dipole transition moment, one of the most important spectroscopic quantities of interest to us, can be obtained from the wavefunctions of the initial state $\Psi_{j,v}(\vec{q},\vec{Q})$ and from the final state $\Psi_{j',v'}(\vec{q},\vec{Q})$ by calculating an average value:

$$M\ (\ jv,\ j'v') = \int \Psi_{j,v}^*(\vec{q},\vec{Q})\hat{M}\Psi_{j',v'}(\vec{q},\vec{Q})d\vec{q}d\vec{Q} \qquad (1.7)$$

for the electric dipole moment operator $\hat{M}$ which is defined by the following equation:

$$\hat{M} = -|e|\sum_{l=1}^{n}\hat{r}_l + |e|\sum_{k=1}^{N}Z_k\hat{R}_k \qquad (1.8)$$

where *e* is the charge of the electron, Z_k is the atomic number of nucleus *k*, *n* is the number of electrons, *N* is the number of nuclei, r_l is the position vector of the *l*-th electron, and R_k is the position vector of the *k*-th nucleus.

A simple interpretation of the electronic transition dipole moment is the following: if a molecule interacts with electromagnetic field, it behaves like an oscillating dipole due to a promotion of an electron from one orbital to another. The magnitude of this dipole depends on the dipole moment of the overlap charge density of the initial and final orbitals.

In an experimental measurement, a quantitative value which can be related to the electric dipole moment transition is the oscillator strength *f*. Oscillator strength is

proportional to the area under the band corresponding to the electronic transition in the absorption spectrum, and thus can be obtained by integration over the corresponding band:

$$f = (\frac{m_e c}{\pi e^2 n_0}) \int \varepsilon(\tilde{v}) d\tilde{v} = \frac{4.319 \times 10^{-9}}{n_0} \int \varepsilon(\tilde{v}) d\tilde{v} \qquad (1.9)$$

where n_0 is the refractive index of the solution in the region of the absorption band, m_e and e are mass and charge of electron, respectively, and c is the velocity of light in vacuum.

The proportionality exists between the oscillator strength and the electric dipole strength of an i-th electronic transition, if the contribution of the higher transition moments (magnetic dipole, electric quadrupole or octupole) to absorption is negligible:

$$f_i \sim D_i = 9.188 \cdot 10^{-3} \int_i \frac{\varepsilon(\tilde{v})}{\tilde{v}} d\tilde{v} \qquad (1.10)$$

where the dipole strength may be written using the definition of the operator of the electric dipole moment:

$$D_i = \sum_{\alpha\gamma} \langle \Psi_{0\gamma} | \hat{M} | \Psi_{i\alpha} \rangle \cdot \langle \Psi_{i\alpha} | \hat{M} | \Psi_{0\gamma} \rangle \qquad (1.11)$$

Here, Ψ_0 is the wavefunction of the ground state, Ψ_i is the wavefunction of the final state. α and γ are indices used to separate different components of degenerate electronic states.

1.2. Advantages of polarized spectroscopy

The most useful methods of classical molecular spectroscopy are based on measurements that use light for probing the investigated structure or process. Such experiments may involve absorption, luminescence or light scattering by the investigated objects. In principle, the experimental results reveal changes of the probing function F during penetration of radiation through the investigated substance. This quantity may be represented as a function of three variables:

$$F = F(E, I, p) \qquad (1.12)$$

where E is the energy of the photon of light, I is the light intensity and p is the light polarization.

The changes of the initial function induced by a substance depend, in general, on its internal properties. It became a habit to call them the spectroscopic properties of the substance.

The knowledge of the spectral properties of the substance allows us to predict the response of the substance to an external perturbation.

In the case of an isotropic sample, i. e., a sample without any distinguished internal directions, it is natural to simplify the probing function to a function of two variables:

$$F = F(E, I) \qquad (1.13)$$

In vacuum, the electric vector of a linearly polarized electromagnetic wave propagating along the x axis in a positive direction is given by:

$$E(t, x) = E_0 \sin(2\pi\nu(t - x/c) + \theta) = E_0 \sin(\omega(t - x/c) + \theta) \qquad (1.14)$$

where E_0 is a constant vector, $2\pi\nu t + \theta$ is the phase at time t, θ is the phase at time 0, and ν is the frequency in cycles per seconds (cps, Hz). $\hbar\omega$ is the energy of the photon. The angular frequency in radians per seconds is $\omega = 2\pi\nu$. $\hbar$ is smaller than the Planck constant h by a factor 2π. $c = 3 \times 10^8 \ m/s$ stands for the speed of light in vacuum.

The other component of the electromagnetic field, the magnetic field, is given by:

$$H(t, x) = H_0 \sin(2\pi\nu(t - x/c) + \theta) \qquad (1.15)$$

The range from 380 to 780 nm is the visible region that corresponds to wavenumbers between 12821 cm^{-1} and 26316 cm^{-1}, where wavenumber is defined as $\bar{\nu} = \nu/c = 1/\lambda$. Infrared radiation (IR) and ultraviolet (UV) light are found at shorter and longer wavenumbers, respectively.

1.2.1 Linear Dichroism

The Lambert-Beer Law

i. *Isotropic Sample*

When collimated light passes through an absorbing homogeneous isotropic sample it is attenuated. If light absorption is the only attenuation mechanism (there is no scattering or another mechanism decreasing the light intensity), after passage through a sample l cm thick, the light intensity $I(\tilde{v})$ is described by the Lambert-Beer law:

$$I(\tilde{v}) = I_0(\tilde{v})10^{-\varepsilon(\tilde{v})cl} = I_0(\tilde{v})10^{-E(\tilde{v})} = I_0(\tilde{v})e^{-\sigma(\tilde{v})n'l} = I_0(\tilde{v})e^{-\alpha(\tilde{v})l} \qquad (1.16)$$

where $\varepsilon(\tilde{v})$ is the decadic molar absorption coefficient, $\sigma(\tilde{v})$ is the absorption cross section of the solute in the particular solvent used, and $\alpha(\tilde{v})$ is the absorption coefficient of the sample. Traditionally, the result of the absorption experiment is the optical density:

$$E(\tilde{v}) = D(\tilde{v}) = \varepsilon(\tilde{v})cl = -\log \frac{I(\tilde{v})}{I_0(\tilde{v})} \qquad (1.17)$$

The decadic molar absorption coefficient $\varepsilon(\tilde{v})$ is usually referred to simply as "the absorption coefficient". Its units are $L\ mol^{-1}\ cm^{-1}$ and it shows how the beam of light will be attenuated by a solution 1 *cm* thick and containing 1 *mol/L* of the substance.

For practical application of the Lambert-Beer law, it is important to keep in mind the assumptions under which it is valid, because in practice, light absorbance by the solvent is not the only attenuation mechanism, since scattering, reflections and absorbance of the solvent also lead to intensity losses.

ii. *Anisotropic Samples*

In the case of an isotropic sample only one independent absorption spectrum can be obtained. The situation is completely different for an anisotropic sample. The simplest

example is the sample with one selected axis, a so-called uniaxial sample. There are many

possibilities to obtain uniaxial samples, for instance:

1. Stretching polymer sheets and aligning guest molecules along the stretching direction.

2. Photoorientation of molecules in a rigid medium: rare gas matrices at low
   temperatures, polymers sheets. For example, photoorientation of different tautomers
   of photochromic compounds isolated in rare gas matrix at low temperature.

3. Orientation of molecules in an electric field.

4. Anisotropy of molecules dissolved in liquid crystals or in streaming solutions, etc.

The probing function $F = F(E, I)$ that depends on two variables is not sufficient for

a full description of an anisotropic sample. The resolution of this problem is introducing

polarization of exciting light, an additional parameter included in the initial function.

Two linearly independent spectra can be measured for an anisotropic uniaxial sample,

one with the electric vector of light parallel to the Z-axis, $E_Z(\tilde{v})$ and one in which this vector

is perpendicular to the Z-axis, $E_Y(\tilde{v})$. Usually, the Z-axis is the axis of anisotropy, the

direction of polymer stretching or the direction of polarization of the exciting light in the case

of photoorientation. The polarized spectra thus obtained resemble those of an isotropic

sample, but the relative intensities of absorption bands are clearly different. An explanation

of this difference is that the molecules are partially oriented in an anisotropic medium. As is

well known, absorption probabilities depend on the angle between the direction of the

electric field ε and the direction of the transition moment M. The physical nature of the

transition moment is related to transient oscillations in the molecular charge density induced

by the electric field of the exciting light. In addition, proportionality exists between the

probability of the absorption W and the square of the projection of the dipole moment

transition on the direction of ε, electric field of the light.

$$W \propto (M \cdot \varepsilon)^2 = |M|^2 \cos^2(M, \varepsilon) \qquad (1.18)$$

where (M,ε) is the angle between M and ε. Taking into account that the electric field is a unit vector with components ε_x, ε_y, ε_z and from the geometrical properties of projections on a selected axis it is possible to obtain that:

$$\cos^2(M,\varepsilon_x)+\cos^2(M,\varepsilon_y)+\cos^2(M,\varepsilon_z)=1 \tag{1.19}$$

Thus, for a uniaxial sample, the average values of $\langle\cos^2(M,\varepsilon_x)\rangle$ and $\langle\cos^2(M,\varepsilon_y)\rangle$ are equal and the direction of the transition moment M can by described by a single parameter K which is called in the polarization spectroscopy the *orientation factor*:[1]

$$K=\langle\cos^2(M,\varepsilon_z)\rangle, \tag{1.20}$$

and for other averages:

$$\langle\cos^2(M,\varepsilon_x)\rangle=\langle\cos^2(M,\varepsilon_y)\rangle=(1-K)/2 \tag{1.21}$$

The absorption is maximized when M and ε are parallel and vanishes for a mutually perpendicular orientation. Consequently, the absorptions of isotropic and anisotropic samples are related:[1]

$$E^{iso}(\tilde{v})=\left(E_Z(\tilde{v})+2E_Y(\tilde{v})\right)/3 \tag{1.22}$$

The ratio between $E_Z(\tilde{v})$ and $E_Y(\tilde{v})$ is known as the dichroic ratio $d(\tilde{v})$:

$$d(\tilde{v})=E_Z(\tilde{v})/E_Y(\tilde{v})=2K/(1-K) \tag{1.23}$$

It is common to refer to positive $(d>1)$ dichroism and negative $(d<1)$ dichroism. For nonoverlapping transitions the dichroic ratio and the orientation factor have simple interpretation, allowing a straightforward determination of the orientation of the transition dipole moment in the molecular frame from the absorption spectrum, in addition to the energy and the intensity of the transition. The information about the orientation of molecular framework in a laboratory system of coordinates is required for such applications. Usually,

the sample has a unique axis Z, due to some kind of alignment determined in the laboratory system of coordinates, e. g. by polymer stretching or by photoorientation. In an isotropic sample $d = 1$, and $K = 1/3$, and the average alignment angle is 54.5^0. In other simple cases when the *i-th* dipole moment transition of all molecules is oriented parallel or perpendicular to the Z-axis K is 1 or 0, and the average alignment angle is 0^0 or 90^0, respectively.

This analysis is also possible for overlapping transitions, using Thulstrup, Eggers, Michl (TEM) methodology.[1] The partial absorbance of the *i*-th transition for an overlapping band $A_i(\tilde{v})$ is defined as the contribution of the *i-th* transition to the absorbance measured on a sample of molecules with their *i-th* transition oriented parallel to the electric vector of the light. The result for the three components of optical density can be written as a single matrix equation:

$$\begin{pmatrix} E_X(\tilde{v}) \\ E_Y(\tilde{v}) \\ E_Z(\tilde{v}) \end{pmatrix} = \sum_i A_i(\tilde{v}) \begin{pmatrix} (1-K_i)/2 \\ (1-K_i)/2 \\ K_i \end{pmatrix} \qquad (1.24)$$

According to this equation, in $E_Y(\tilde{v})$ the *i-th* transition appears with the weight $(1-K_i)/2$, in $E_Z(\tilde{v})$ with the weight K_i. In a linear combination $E_Z(\tilde{v}) - gE_Y(\tilde{v})$ the *i-th* transition appears with the weight $K_i - g(1-K_i)/2$. The value of g, for which the spectral contribution from the *i-th* transition disappears from the linear combination, is called the reduction factor, d_i:

$$d_i = 2K_i/(1-K_i) \qquad (1.25)$$

The procedure of searching for a linear combination in which the contribution of a particular transition to the spectrum just disappears is known as "stepwise reduction procedure" and allows us to determine the orientation factor and thus, the orientation of the *i-th* dipole moment transition in the molecular framework, for overlapping transitions.

1.2.2. Natural Circular Dichroism

An interesting example of the effect that is based on an inherent property of the molecule and used by polarization spectroscopy is natural circular dichroism (CD). While the LD is an effect induced by applying external forces, the CD effect is due to an intrinsic property of molecules, known as chirality. An object is chiral if it can not be superimposed onto its mirror image. The optical activity is explained in terms of the circular polarizations, as due to the difference in absorption coefficients for left-handed and right-handed circularly polarized light.

Linearly polarized light can be represented, in terms of circularly polarized light, as a sum of right-handed and left-handed polarized components of identical frequency and vice versa, circularly polarized light is a sum of two linear polarizations with a $\pm \pi / 2$ shift in phase and the same amplitudes. Consequently, the plane of polarization of linearly polarized light passing through the optically active sample is rotated by an angle α because of different refractive indices n_L and n_R and the expression for the velocity of light in a medium $c = c_o / n$ gives the phase shift. If, in addition, at a wavelength that is being absorbed by the sample, not only phases, but also amplitudes of circularly polarized light are changed the incident light becomes elliptically polarized. Such situation occurs for isotropic optically active samples, whereas for anisotropic samples, it becomes more complicated.

The optical activity of a chiral substance is simple to investigate by measuring the rotation angle of the plane of polarization after passing linearly polarized light through the sample. The dependence of the rotation angle $\alpha(\tilde{\nu})$ on different refractive indices n_L and n_R is given by:

$$\alpha(\tilde{\nu}) = 1800\tilde{\nu}[n_L - n_R] \tag{1.26}$$

The equipment for CD measurements is a little bit more complicated than an ordinary spectrometer, the monochromatic light being modulated between two purely circular

polarizations. Different ε_L and ε_R produce intensity modulation which can be described as a so-called molar ellipticity:

$$[\theta]_M = 3298\,(\varepsilon_L - \varepsilon_R) \tag{1.27}$$

Two molecules differing from each other as an object differs form its mirror image are called enantiomers. They show the same degree of the optical activity but with the opposite sign. Therefore, the most successful applications of CD spectroscopy are related to structure elucidations.

A quantitative value of the optical activity of an electronic transition is provided by the rotational strength $\Re$, which can by obtained from a CD spectrum by integration over the corresponding band:

$$\Re = 7.51 \times 10^{-5} \int \frac{[\Theta]_M}{\tilde{v}}\,d\tilde{v} = 0.248 \int \frac{(\varepsilon_L - \varepsilon_R)}{\tilde{v}}\,d\tilde{v} \tag{1.28}$$

Theoretically, the rotational strength is described by the Rosenfeld formula:

$$\Re(jv, j'v') = \mathrm{Im}\{\langle \Psi^*_{j,v}(\vec{q},\vec{Q}) | \hat{M} | \Psi_{j',v}(\vec{q},\vec{Q}) \rangle \cdot \langle \Psi^*_{j,v}(\vec{q},\vec{Q}) | \hat{\mathrm{M}} | \Psi_{j',v}(\vec{q},\vec{Q}) \rangle\} \tag{1.29}$$

where $\hat{\mathrm{M}}$ is the magnetic transition moment operator:

$$\hat{\mathrm{M}} = \frac{-|e|}{2m_e c} \sum_j (\hat{r}_j \times \hat{p}_j) \tag{1.30}$$

Here $\hat{p}_j = -i\hbar\hat{\nabla}_j$ is the linear momentum operator, $\hat{r}_j$ is the position operator of the electron j. In the case when the wavefunctions of the initial and the final states are real the formula may by written as:

$$\Re(jv, j'v') = \langle \Psi^*_{j,v}(\vec{q},\vec{Q}) | \hat{M} | \Psi_{j',v}(\vec{q},\vec{Q}) \rangle \cdot \langle \Psi^*_{j,v}(\vec{q},\vec{Q}) | \hat{\mathrm{M}} | \Psi_{j',v}(\vec{q},\vec{Q}) \rangle = |\hat{M}||\hat{\mathrm{M}}|\cos(\hat{M},\hat{\mathrm{M}}) \tag{1.31}$$

Therefore, the rotational strength is present when both magnetic and electric dipole transition moments have non-vanishing values and when both moments are not perpendicular to each other.

1.2.3. Magnetic Circular Dichroism

In the presence of a longitudinal magnetic field, electronic transitions of molecules acquire circular polarization, even for molecules which have been not optically active before. This phenomenon is referred to as the Faraday effect and has been investigated during many decades. The spectroscopic method which appeared as a tool for such investigations is magnetic circular dichroism (MCD). The effect of MCD is similar to the effect of natural circular dichroism and is defined as the difference of the extinction coefficients between left-handed and right-handed circularly polarized light in the presence of the magnetic field directed parallel to the light beam propagation. Optical transitions to electronic excited states become active towards right-handed or left-handed circularly polarized light depending on the selection rules for MCD. Briefly, the change in the electronic angular momentum in a transition ($\Delta M_J = \pm 1$) determines whether a right-handed or left-handed photon is preferentially absorbed. Moreover, the sum over two polarizations or the total absorption remains constant, even when the relative population of the ground state sublevels is perturbed at high magnetic fields and low temperatures.

While one scalar quantity - the rotatory strength - is sufficient to describe the CD spectrum, the theoretical description of MCD is a bit more complicated. In general, three scalar numbers are engaged in the explanation of the contribution of each electronic transition to the MCD spectra of an isotropic sample. These quantities are A_i, B_i, and C_i, known as Faraday terms of the *i-th* electronic transition.

The shapes of a band corresponding to B_i or C_i terms in the MCD spectrum are the same. These bands in a simplest case can be described by a Gaussian profile. The sign of an MCD band can be positive or negative just as in CD spectra. According to the convention, a *B* or *C* term is called positive if it corresponds to a negative band in the MCD spectrum, and

negative if it corresponds to a positive one. If nonzero B and C terms are present, a temperature dependence experiment is needed for their separation.

The shape of the A term does not look like that of an absorption band, but rather as a derivative of an absorption peak. The A term is called positive if the molar ellipticity $[\theta]_M(\tilde{\nu})$ is negative at lower wavenumbers and it is called negative if $[\theta]_M(\tilde{\nu})$ is positive at lower wavenumbers.

The total MCD spectrum can be written as a sum over all electronic transitions:

$$[\theta]_M(\tilde{\nu}) = -21.3458 \sum_i [A_i f_i(\tilde{\nu}) + (B_i + C_i / kT) g_i(\tilde{\nu})] \tag{1.32}$$

Here $g_i(\tilde{\nu})$ is a normalized line shape function and its derivative is labeled $f_i(\tilde{\nu})$, k is the Boltzmann constant and T is the absolute temperature. The units are $D^2\beta_e$ for A_i and $D^2\beta_e/cm^{-1}$ for B_i and for C_i/kT, where D stands for Debye and β_e for Bohr magneton.

Differences in relative intensities between various bands observed in absorption and MCD spectra enable using MCD measurements for the assignment and the description of electronic transitions undetected in absorption. In addition, MCD may be complementary to polarized spectroscopy, for example LD spectroscopy, when the parallel transitions have different B term signs or, on the contrary, there are B terms of equal sign for transitions perpendicular to each other.

The values of A_i, B_i, and C_i terms are most easily obtained from an MCD spectrum using the moment analysis. The following expressions for Faraday terms, involving integration over the experimentally obtained bands, have been obtained for an i-th electronic transition:

$$A_i = 33.53^{-1} \int_i [\theta]_M(\tilde{\nu}) \frac{(\tilde{\nu} - \tilde{\nu}_0)}{\tilde{\nu}} d\tilde{\nu} \tag{1.33}$$

$$B_i + C_i / kT = \int_i \frac{[\theta]_M(\tilde{\nu})}{\tilde{\nu}} d\tilde{\nu} \tag{1.34}$$

$$D_i = 9.188 \cdot 10^{-3} \int_i \frac{\varepsilon(\tilde{v})}{\tilde{v}} d\tilde{v} \qquad (1.35)$$

where D_i is the dipole strength, obtained by integration over a corresponding absorption band.

The knowledge of the dipole strength D_i and A_i leads us to another spectroscopic application of MCD, important for molecules of high symmetry, calculation of the magnetic moment of the excited state. The magnetic moment may be derived from the following relationship:

$$\mu_i = -2A_i / D_i \qquad (1.36)$$

The physical interpretation of the B term contribution appears from the interaction between different energy levels perturbed by applying the magnetic field and occurs both for degenerate and nonedegenerate states. The interpretation of the A and C terms is more obvious and the contribution of these terms appears only for a degenerate ground or excited state, respectively.

The theoretical description of MCD

In quantum chemistry terms the expressions for A_i, B_i, and C_i may by written as:

$$A_i = \frac{1}{2g} \sum_{\alpha\gamma} (\langle \Psi_{i\alpha} | \hat{M} | \Psi_{i\alpha} \rangle - \langle \Psi_{0\alpha} | \hat{M} | \Psi_{0\alpha} \rangle) \cdot \mathrm{Im}(\langle \Psi_{i\alpha} | \hat{M} | \Psi_{i\alpha} \rangle \times \langle \Psi_{0\alpha} | \hat{M} | \Psi_{0\alpha} \rangle) \qquad (1.37)$$

$$B_i = \frac{1}{g} \sum_{\alpha\gamma} \mathrm{Im}\{ \sum_{k\chi,k\neq 0} [\langle \Psi_{k\chi} | \hat{M} | \Psi_{0\gamma} \rangle \cdot \langle \Psi_{0\gamma} | \hat{M} | \Psi_{i\alpha} \rangle \times \langle \Psi_{i\alpha} | \hat{M} | \Psi_{k\chi} \rangle] / [E_k - E_0] +$$
$$\sum_{k\chi,k\neq i} [\langle \Psi_{i\alpha} | \hat{M} | \Psi_{k\chi} \rangle \cdot \langle \Psi_{0\gamma} | \hat{M} | \Psi_{i\alpha} \rangle \times \langle \Psi_{k\chi} | \hat{M} | \Psi_{0\gamma} \rangle] / [E_k - E_i] \} \qquad (1.38)$$

$$C_i = \frac{1}{2g} \sum_{\alpha\gamma} (\langle \Psi_{0\gamma} | \hat{M} | \Psi_{0\gamma} \rangle \cdot \mathrm{Im}(\langle \Psi_{0\gamma} | \hat{M} | \Psi_{i\alpha} \rangle \times \langle \Psi_{i\alpha} | \hat{M} | \Psi_{0\gamma} \rangle) \qquad (1.39)$$

where g is the degree of degeneracy of an electronic state. $\hat{M}$ and $\hat{M}$ are the operators of the electric and magnetic moment, respectively. Ψ_0, Ψ_i, and Ψ_k are unperturbed wave functions of the ground, the final, and the intermediate states defined in the absence of magnetic field. The indices α and γ are used to separate different components of degenerate electronic states.

The contribution from the C term appears for molecules with a degenerate ground state when degeneracy is removed by the presence of the magnetic field. The A term contributes to MCD if excited states of the molecules are degenerate and this leads to splitting of the energy levels due to Zeeman effect in the magnetic field. While the interpretation of A and C terms is rather simple, the origin of B terms is more complex. The perturbation of molecules by magnetic field is described by two infinite sums, which express mixing of the initial state as well as the final state with all intermediate states. A possible way to resolve this problem is bringing into consideration a simple model which can introduce the MCD effect more clearly. The perimeter model has been successfully used for this goal during last decades.

The perimeter model

(i) *Introduction*

The perimeter model, introduced by Platt[2] (1949), extended and reformulated in terms of molecular orbitals as linear combination of atomic orbitals (LCAO MO) by Moffitt[3] (1954) and Gouterman[4] (1961), and Michl[5] (1978), turned out to be very useful in the explanation and understanding of the electronic spectra of cyclic π-electron systems.

Platt's original perimeter model was a free-electron molecular orbital (FEMO) model based on a one-dimensional circular potential along which π electrons can move freely. An orbital in this model can be represented by:

$$\phi_l = (1/\sqrt{2\pi})e^{il h}, \quad l = 0, \pm 1, \pm 2... \tag{1.40}$$

These FEMOs are degenerate, except for $l = 0$. $l h$ is the angular momentum of an electron on a circular orbit, and the degeneracy can be described by an electron moving counterclockwise or clockwise along the perimeter.

The next important step in the adaptation of the perimeter model was representing the perimeter orbitals as linear combinations of n atomic orbitals (AOs) χ_μ. These LCAO MOs are determined completely by symmetry for regular polygons and may be written as:

$$\phi_l = (1/\sqrt{n})\sum_{\mu=0}^{n-1}\exp(\pm 2\pi i k\mu / n)\chi_\mu = (1/\sqrt{n})\sum_{\mu=0}^{n-1}[\cos(2\pi k\mu / n) \pm i\sin(2\pi k\mu / n)]\chi_\mu \qquad (1.41)$$

where k is a non-negative integer and $l = \pm k$ may be treated as the angular momentum quantum number. In the Hückel molecular orbital (HMO) model these MOs have energies

$$\varepsilon_{\pm k} = \alpha + 2\cos(2\pi k / n)\beta, \quad k = 0, 1, 2... \qquad (1.42)$$

In contrast to the FEMOs the total number of LCAO MOs is limited to the number n of perimeter AOs χ_μ. The most stable MO ϕ_0 is real. The orbitals of highest energy are degenerate for an odd number of atoms. If the number of atoms n in the perimeter is even, the last MO is not degenerate and can be equally well labeled by $\phi_{n/2}$ or $\phi_{-n/2}$.

An electron has a positive z component of the orbital angular momentum if it moves counterclockwise along the perimeter when viewed from the positive end of the z axis. Since the electron is negatively charged, it produces a negative z component of the magnetic moment μ_z. The situation for the electron moving clockwise along the perimeter is the opposite. Such an electron produces a positive z component of the magnetic moment. The magnitude of the magnetic moment is the function of the number of atoms n in the perimeter and of the orbital subscript k. The magnetic moment is 0 for $k=0$, increases with k until $k=n/4$ and then decreases again. The behavior of the magnetic moment is schematically illustrated in Figure 1.1.
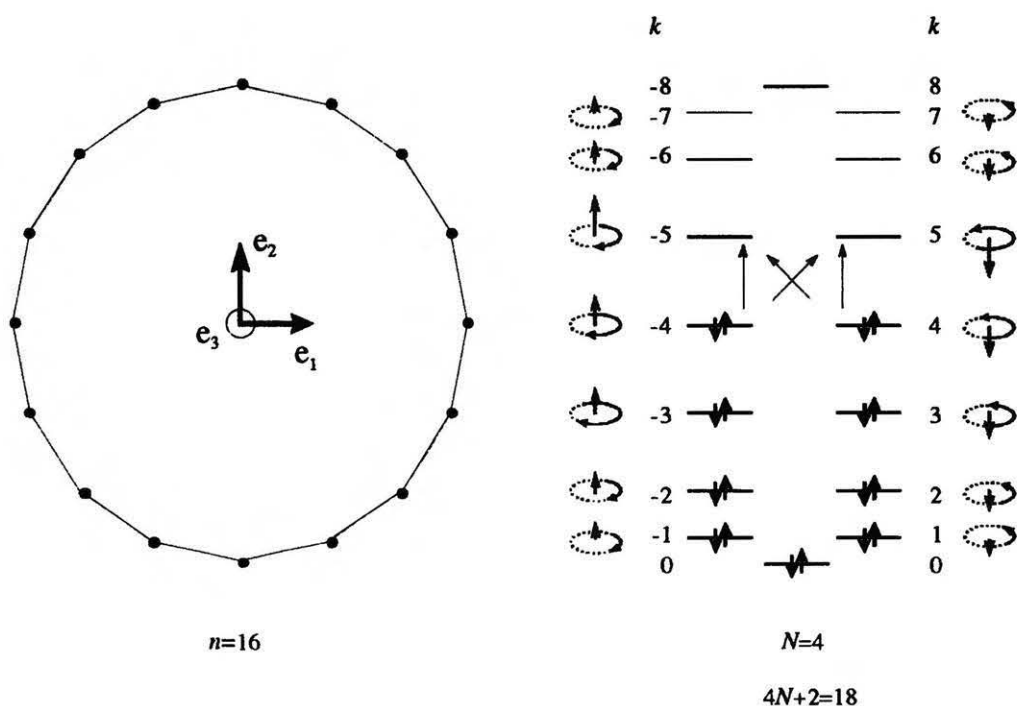
Figure 1.1. The perimeter model of a (4N+2)-electron [n]annulene, geometry on the left and energies of the MOs ϕ_k on the right.

The magnetic moment in the perimeter model reveals periodical behavior which differs from the FEMO model. The reason for this behavior is the n-fold symmetry of the perimeter which is represented by a polygon consisting of n atoms. The fact that the value of the magnetic moment can increase or decrease for electron promotion from an orbital k to an orbital $k+1$, has a huge importance for understanding of the MCD effect in π-electron systems.

All the above considerations refer to singlet states, which play an important role in ordinary spectroscopy.

If the molecule is described by the base n-atom perimeter with $4N+2$ electrons the orbitals up to and including ϕ_N and ϕ_{-N} will be degenerate and fully occupied. Among those, the pair of orbitals of highest energy are the highest occupied molecular orbitals (HOMO). The orbitals ϕ_{-N-1} and ϕ_{N+1} will be free and also degenerate, yielding the pair of the lowest

unoccupied molecular orbitals (LUMO). If only $HOMO \to LUMO$ excitations are taken into account, four excited configurations $\phi_1 \equiv \phi_{N \to N+1} = \phi_N^{N+1}$, $\phi_2 \equiv \phi_{-N \to -N-1} = \phi_{-N}^{-N-1}$, $\phi_3 \equiv \phi_{-N \to N+1} = \phi_{-N}^{N+1}$, $\phi_4 \equiv \phi_{N \to -N-1} = \phi_N^{-N-1}$ are produced in addition to the ground state configuration ϕ_0, see Figure 1.2.
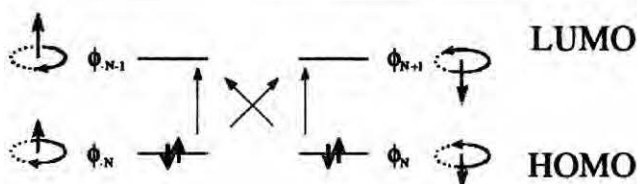
Figure 1.2. HOMO and LUMO of [n]annulene with (4N+2)-electrons. Orbital occupancy in the ground configuration and four one-electron $HOMO \to LUMO$ excitations are indicated.

If the perimeter is charged, i.e. $n \neq 4N + 2$, the five configurations have a different symmetry behavior and the Hamiltonian $\hat{H}$, which is symmetric, cannot mix the configurations with each other ($\langle \phi_i | \hat{H} | \phi_k \rangle = 0$, for $i \neq k$), so the state wave functions are identical with the configuration wave functions.

In the case of an uncharged perimeter, $n = 4N + 2$, the two configurations ϕ_3 and ϕ_4 have the same space symmetry and differ only in two spinorbitals. The Hamiltonian can mix them ($\langle \phi_3 | \hat{H} | \phi_4 \rangle \neq 0$) and two new states appear due to configuration interaction (CI):

$$\Psi(B_{2u}) = (\phi_3 - \phi_4)/(i\sqrt{2})$$
$$\Psi(B_{1u}) = (\phi_3 + \phi_4)/(\sqrt{2})$$

(1.43)

where the nomenclature of the D_{nh} group of symmetry is used. In addition, the configurations ϕ_1 and ϕ_2 are degenerate ($\Psi(E_{1u})$). These, following Platt are called the ^{1}B states. In the case of uncharged perimeter the states composed from ϕ_3 and ϕ_4 are referred to as ^{1}L states. If these states are not degenerate, one of them is called ^{1}L$_a$ and the other is ^{1}L$_b$. Physically, the

states differ in the distribution of the transition density between the ground state and the excited state. For ^1L_b its maxima are in the middle of bonds and its nodes pass through the atoms, whereas for ^1L_a the situation is the opposite, and the maxima of the transition density are located at atoms.

In terms of the perimeter model the MCD effect has a perfect physical sense. Let us consider the excitation from the ground state to one of the configurations ϕ_N^{N+1} or ϕ_{-N}^{-N-1}. The configuration ϕ_N^{N+1}, with an extra electron in the ϕ_{N+1} orbital is promoted from the ϕ_N orbital and a photon of left-handed polarization is needed for the excitation. Similarly, the ϕ_{-N}^{-N-1} configuration is populated by a photon of right-handed polarization. Both of these configurations preserve the sense of circulation of the promoted electron and can be called "sense-preserving".

The two other configurations ϕ_{-N}^{N+1} and ϕ_N^{-N-1} are forbidden, because to undergo excitation, the quantum number of an electron has to be changed by $2N+1$. The sense of an electron circulation is being reversed upon excitation and such configurations are referred to as "sense-reversing".

The MCD is explained not only by the electric dipole moment changes but by the changes in the magnetic moment, too. The magnetic moment of the ground configuration is zero because all electrons circulating counterclockwise in orbitals ϕ_k are compensated by clockwise circulations of electrons in orbitals ϕ_{-k}. This cancellation will be broken upon excitation and the magnetic moment of an excited configuration will be given by the difference between the magnetic moment of the excited electron before and after excitation. For "sense-preserving" excitations, this difference in magnetic moment $\mu^-(n,N)$ will be very small, because the magnetic moments before and after excitation will have the same sign and differ only a little in the magnitude. The situation for "sense-reversing" configurations is

described by $\mu^+(n,N)$, which will be quite large, because the magnetic moments of the excited electron will differ in sign before and after excitation. The magnetic moment of the perimeter corresponding to one of the excited configurations described above is given by magnitudes $\mu^\pm(n,N)$, which can be written in units of Bohr magneton, β_e as:

$$\mu^\pm(n,N) = \mu_1^\pm(n,N) + \mu_2^\pm(n,N)$$
$$\mu_1^-(n,N) = -0.26|\beta|l_0^2 \cos(\pi/n)\sin(\pi q/2n)$$
$$\mu_2^-(n,N) = -0.078|\beta|l_0^2 \cos^2(\pi/n)\cos(\pi q/n) \qquad (1.44)$$
$$\mu_1^+(n,N) = -0.26|\beta|l_0^2 \cot(\pi/n)\cos(\pi/n)\cos(\pi q/2n)$$
$$\mu_2^+(n,N) = 0.039|\beta|l_0^2 \cot(\pi/n)\cos(2\pi/n)\sin(\pi q/n)$$

where the minus and plus signs refer to "sense-reversing" or "sense-preserving" configurations, respectively. q is the net charge of the π system, $q=n-(4N+2)$. l_0 (in Å) is the distance between neighboring atoms and β (in eV) is the resonance integral between these atoms.

(ii) *The generalization of the perimeter model and the experimental applications.*

The most important advantage of the perimeter model is that it can be easily extended to real systems that may by derived from a regular n-atom perimeter by introducing structural perturbations. Different types of structural perturbations have been put below in the sequence, in the order of increasing influence on the unperturbed perimeter:
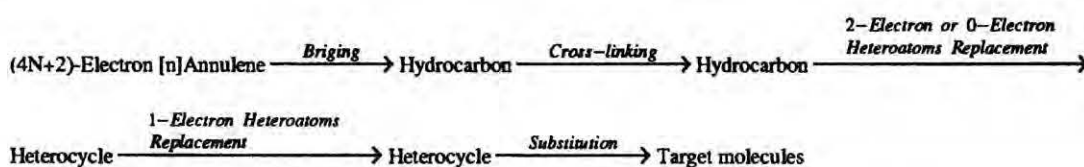
These structural perturbations will lower the symmetry and remove the degeneracy of the perimeter MOs, which is why it is comfortable to write the perturbation in terms of the energy splitting of the HOMO and LUMO pairs.

The CI matrix for the four excited configurations ϕ_1 to ϕ_4 can be written as:

$$
\begin{array}{c}
\begin{array}{cccc}
\phi_N^{N+1} & \phi_{-N}^{-N-1} & \phi_{-N}^{N+1} & \phi_N^{-N-1}
\end{array}\\
\begin{array}{c}
\phi_N^{N+1}\\
\phi_{-N}^{-N-1}\\
\phi_{-N}^{N+1}\\
\phi_N^{-N-1}
\end{array}
\left(
\begin{array}{cccc}
E(B) & 0 & a^* & b^*\\
0 & E(B) & b & a\\
a & b^* & E(L) & Q\\
b & a^* & Q & E(L)
\end{array}
\right)
\end{array}
\tag{1.45}
$$

where interaction matrix elements appear due to the structural perturbation:

$$
\begin{aligned}
a &= \langle \phi_3 | \hat{H}' | \phi_1 \rangle = -\langle \phi_N | \hat{h}' | \phi_{-N} \rangle\\
b &= \langle \phi_4 | \hat{H}' | \phi_1 \rangle = \langle \phi_{-N-1} | \hat{h}' | \phi_{N+1} \rangle
\end{aligned}
\tag{1.46}
$$

$Q = \langle \phi_3 | \hat{H} | \phi_4 \rangle$ is the interaction matrix element between configurations ϕ_3 and ϕ_4.

The perturbation is considered as a sum of one-electron perturbations:

$$
\hat{H}' = \sum_i \hat{h}'(i)
\tag{1.47}
$$

In order to write the perturbations in terms of the ΔHOMO and ΔLUMO, the complex quantities a and b are presented in the following form:

$$
\begin{aligned}
a &= |a| e^{i\alpha}\\
b &= |b| e^{i\beta}
\end{aligned}
\tag{1.48}
$$

Here,

$$
2|a| = \Delta HOMO
\tag{1.49}
$$

$$
2|b| = \Delta LUMO
\tag{1.50}
$$

The phases α and β determine the orientation of the nodes of the perturbed MOs with respect to the molecular framework and can be written as:

$$
\tan(2\alpha) = 2(|a| + |b|)/[E(B) - E(L)]
\tag{1.51}
$$

$$
\tan(2\beta) = 2(|a| - |b|)/[E(B) - E(L)]
\tag{1.52}
$$

where E(B)-E(L) is the energy difference between the L and B states in the parent perimeter.

The relative magnitude of $\Delta HOMO$ and $\Delta LUMO$ determines the sign of the B terms of the ^{1}L and ^{1}B states of aromatic molecules. Therefore, according to the perimeter model, the chromophores can be divided into three different types:

(a) $\Delta HOMO \gg \Delta LUMO$, the signs of the four B terms are $+,-,+,-$ in order of increasing transition energy and such chromophores are referred to as "positive-hard" ("positive" and "negative" refer to the sign of the B term corresponding to the ^{1}L$_1$ states (B(L$_1$)). The values of the B terms can be written as:

$$\frac{B(\text{B})}{D(\text{B})} = (\sin^2 \alpha)\frac{\mu^-(n,N)-\mu^+(n,N)}{E(B)-E(L)} \qquad (1.53)$$

$$\frac{B(\text{L})}{D(\text{L})} = (-\cos^2 \alpha)\frac{\mu^-(n,N)-\mu^+(n,N)}{E(B)-E(L)} \qquad (1.54)$$

where D(B) and D(L) are the dipole strengths in the parent perimeter.

(b) $\Delta HOMO \ll \Delta LUMO$, this irregularity is characterized by the $-,+,+,-$ or $-,+,-,+$ sequences of signs for a weak or strong perturbation, respectively, and corresponds to the so-called "negative-hard" chromophore. The algebraic expressions for the B terms of the "negative-hard" chromophore are:

$$\frac{B(\text{B})}{D(\text{B})} = (\sin^2 \beta)\frac{\mu^-(n,N)+\mu^+(n,N)}{E(B)-E(L)} \qquad (1.55)$$

$$\frac{B(\text{L})}{D(\text{L})} = (-\cos^2 \beta)\frac{\mu^-(n,N)+\mu^+(n,N)}{E(B)-E(L)} \qquad (1.56)$$

If A terms are present, the expression for these MCD parameters, corresponding to different states, of "negative-hard" chromophore can be written as:

$$\frac{A(\text{L})}{D(\text{L})} = -\frac{1}{2}[\frac{\mu^-(n,N)\sin^2 \beta-\mu^+(n,N)\cos^2 \beta}{E(B)-E(L)}] \qquad (1.57)$$

$$\frac{A(\text{B})}{D(\text{B})} = -\frac{1}{2}[\frac{\mu^-(n,N)\cos^2 \beta-\mu^+(n,N)\sin^2 \beta}{E(B)-E(L)}] \qquad (1.58)$$

In general, the signs of the B terms in such chromophores are determined by the magnetic mixing of the $^1L_1$ with the $^1L_2$ state and the $^1B_1$ with the $^1B_2$ state. The additional changes of the perimeter, which lower its symmetry, have only a small influence on the relative values of $\Delta HOMO$ and $\Delta LUMO$. Therefore, the MCD signal of such chromophores is very hard to modify by introducing structural perturbations.

(c) $\Delta HOMO = \Delta LUMO$, the third type, defines a "soft" chromophore. Such a chromophore is characterized by a $+, +, +, -$ sequence of the B term signs, which may be changed by minor perturbations that break the equality of $\Delta HOMO$ and $\Delta LUMO$.

For our further purposes, it is helpful to assume that ΔL, the energy separation between the two ^1L states and ΔB, the separation between the two ^1B states are much smaller than the L-B spacing. This corresponds to a situation observed in the aromatic molecules investigated by us and leads to the following equations for the four B terms:

$$B(L_1) = -B(L_2) = -[m^2/(2\Delta L)](4\mu^- \sin^2 \alpha \sin^2 \beta + \mu^+ \sin 2\alpha \sin 2\beta) \qquad (1.59)$$

$$B(B_1) = -B(B_2) = -[m^2/(2\Delta B)](4\mu^- \cos^2 \alpha \cos^2 \beta + \mu^+ \sin 2\alpha \sin 2\beta) \qquad (1.60)$$

The quantity m, electric transition dipole contribution, is a simple function of N and of the perimeter size, n. Similarly, magnetic moment contributions μ^+ and μ^- also depend on N and n. The μ^+ contributions are negative and about a magnitude larger than the μ^- terms, usually also negative.

Formulas 1.59-1.60 show that the crucial quantity that determines the sign of the MCD B terms is the parameter β, which can be approximated as $(\Delta HOMO - \Delta LUMO)/(2[E(B) - E(L)])$. Thus, for a positive value of $\Delta HOMO - \Delta LUMO$ difference, a sequence of signs $+, -, +, -$ of the B terms for the L_1, L_2, B_1 and B_2 transitions should be expected. For a negative value of $\Delta HOMO - \Delta LUMO$, a $-, +, +, -$ sequence is expected for weak perturbations, since in this case the sign of the B terms for B transitions is

dictated by μ^- contributions. For larger perturbations, the μ^+ terms will dominate, and the sequence of B terms will change to $-,+,-,+$ The border limit between the "weak" and "strong" perturbation can be expressed by the ratio of dipole strengths of the L and B transitions:

$$\frac{D(L)}{D(B)} = -\frac{[\ \Delta HOMO^2\ - \Delta LUMO^2\ ]}{4[E(B) - E(L)]^2} \tag{1.61}$$

It was estimated that for a $C_{20}H_{20}^{2+}$ this border limit corresponds *to D(L)/D(B)* ≈ 0.1.[6]

1.3. Methods of matrix isolation spectroscopy

The possibility of using rare gas matrices in spectroscopy has been introduced by Pimentel and his co-workers.[7] Matrix samples are prepared by vapor condensation of a matrix gas and the vapor of guest molecules on a target kept at low temperatures, usually 5-55 K. The deposition temperature of the guest molecules depends on a particular substance and is usually chosen as 2/3 of the melting point. The target temperature is below 1/3 of the matrix material melting point which allows to neglect the diffusion of the host molecules. The targets, in the case of spectroscopic investigation, are optically transparent windows. The window materials depend on the spectral region of interest. CsI, KBr, MgF_2, CaF_2 windows have been used in the infrared (IR) region. Quartz and sapphire are good materials for ultraviolet and visible (UV/VIS) measurements.

One of the most important parameters in matrix spectroscopy is the matrix molecules to the guest molecules ratio (M/R). Its value is usually in the range of 10^2-10^5, sufficient to minimize guest-guest molecules interactions. The sample thickness depends on the oscillator strength of the optical transition that is to be observed. The guest molecules concentration for an allowed electronic transition is of the order of micromole. For observation of the IR transitions or the forbidden electronic transitions about ten times higher concentration is recommended. Any molecule that evaporates without decomposition may be embedded into the matrix. The molecules can be synthesized in the matrix *in situ* by photolysis (decomposition of the precursor molecules by light irradiation) or pyrolysis (the precursor molecules decomposed by heat) of vaporizable component during deposition. This makes matrices good media for synthesis and investigation of unstable species, such as, e.g., free radicals. The photoorientation or photolysis by polarized light induces the anisotropic distribution of the guest molecules in the matrix. The LD experiments can then be performed on such samples. The weak interaction of the host molecules with guests makes matrices

suitable for detailed studies of big organic molecules, for example, porphyrins[8]. The first matrices with even lager molecules - phthalocyanine and its derivatives - were obtained by Gouterman and co-workers.[9-10]

Several features of the behavior of molecules isolated in low-temperature matrices are characteristic of matrix spectroscopy:

1. Spectral shifts are observed in the spectra in comparison with the gas phase. These shifts are explained by weak interactions between host and guest molecules.

2. The line structure often appears in vibronic absorption or emission spectra of isolated molecules. There is no strong interaction of host molecules with each other, due to low concentration and rigid fixation of host molecules in a matrix. The interaction between guest and host molecules is very weak. These factors result in decreasing of the inhomogeneous line broadening.

3. The guest molecules can be built into the host matrix in different manners. The variety of possible molecular microenvironments in the matrix is known as sites. The molecules belonging to one site remain in a local environment which differs a little from that of another site. Therefore, matrix spectra often contain a multiple fine structure due to absorption from different sites.

Typical gas materials are the rare gases, H_2, lighter hydrocarbons, and nitrogen. The rare gases are most often used in matrix spectroscopy.[11-12] There are some reasons for this. Neon, argon, xenon, krypton are chemically inert. Their intermolecular forces in crystals are small. To a good approximation, the forces in rare gases can be described by the Lennard-Jones potential that can by written as:

$$V = 4\varepsilon[(\frac{\delta}{r})^{12} - (\frac{\delta}{r})^6]$$

(1.62)

where ε and δ are numerical constants determined by experiment. This potential has two terms. The attractive force is an induced dipole – induced dipole interaction, r^{-6} term, whereas the repulsion is given by an r^{-12} term.

The rare gas crystals are all optically transparent[12-13] from the far infrared to the vacuum ultraviolet. The lattice frequencies only appear in the IR and these are below 100 cm^{-1}. The ultraviolet absorption of vapor deposited krypton and xenon samples occurs in the region below 200 nm. No argon absorption is observed in this region.[14]

Chapter 2. Goals

This work presents results of spectroscopic, photophysical, and photochemical studies of molecules belonging to three different classes of compounds. In order to describe molecular properties as widely as possible, different methods of polarized spectroscopy have been involved into investigations.

In a general sense, the work can be divided into three parts:

1. The goals of the first one are the description and assignment of the excited states of porphyrin-like molecules and the so-called expanded porphyrins, molecules which contain more than four pyrrole rings.

The investigated molecules included constitutional isomers of porphyrins: corrphycene and hemiporphycene, and expanded porphyrins: isomers of smarygdyrin and alkylated cyclo[6]pyrrole, cyclo[7]pyrrole, cyclo[8]pyrrole. The emphasis was put on MCD spectroscopy. In addition, techniques of LD and anisotropy of fluorescence excitation were also used. The selection of compounds of gradually increasing size was dictated by the intention to check the applicability and limits of the perimeter model in the studies of large aromatic molecules.

2. The second part is devoted to the investigations of photochromic properties of β-thioxoketones. These molecules have been the objects of intense studies due to their photochromic properties. The assignments of tautomeric forms and conformational equilibria have provoked curiosity and led to controversies during last decades. The photoreaction is explained as a hydrogen transfer between sulfur and oxygen upon irradiation whit UV/VIS light. The assignments of molecular structures corresponding to different tautomeric and rotameric forms and the determination of the conformational equilibria, which should

ultimately allow us to propose the mechanism of the photoreaction, are paramount aims in this part of the present work. The presented results include four different β-thioxoketones. The assignments of the final (photoproduct) and the initial forms are based on LD polarization experiments in the IR region, combined with electronic spectroscopy and theoretical predictions.

3. Similarly to the case of single proton transfer that takes a place in β-thioxoketones, the dynamics of double hydrogen transfer which occurs in porphyrin and its isomers are still not completely understood. In this part, the mechanism of the proton double transfer in excited corrphycene is studied by polarized spectroscopy and matrix isolation techniques in combination with theoretical calculations.

Chapter 3. Experimental and computational methods.

3.1. Objects of our investigations.
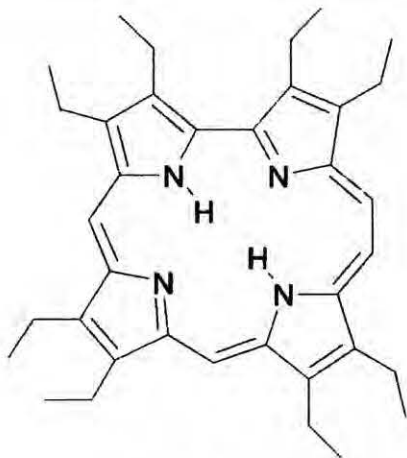
1
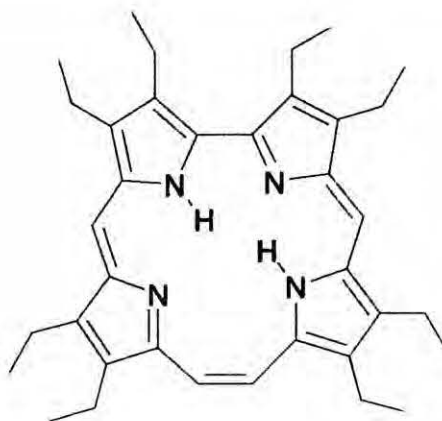
2

| 1 | 2,3,6,7,11,12,16,17-octaethylhemiporphycene (**hemiporphycene**) |

| 2 | 2,3,6,7,11,12,17,18-octaethylcorrphycene (**corrphycene**) |

These compounds were kindly given to us by Professor Emanuel Vogel (University of Cologne). The synthesis and purification of **1** and **2** have been described elsewhere.[15-16]

3   4

---
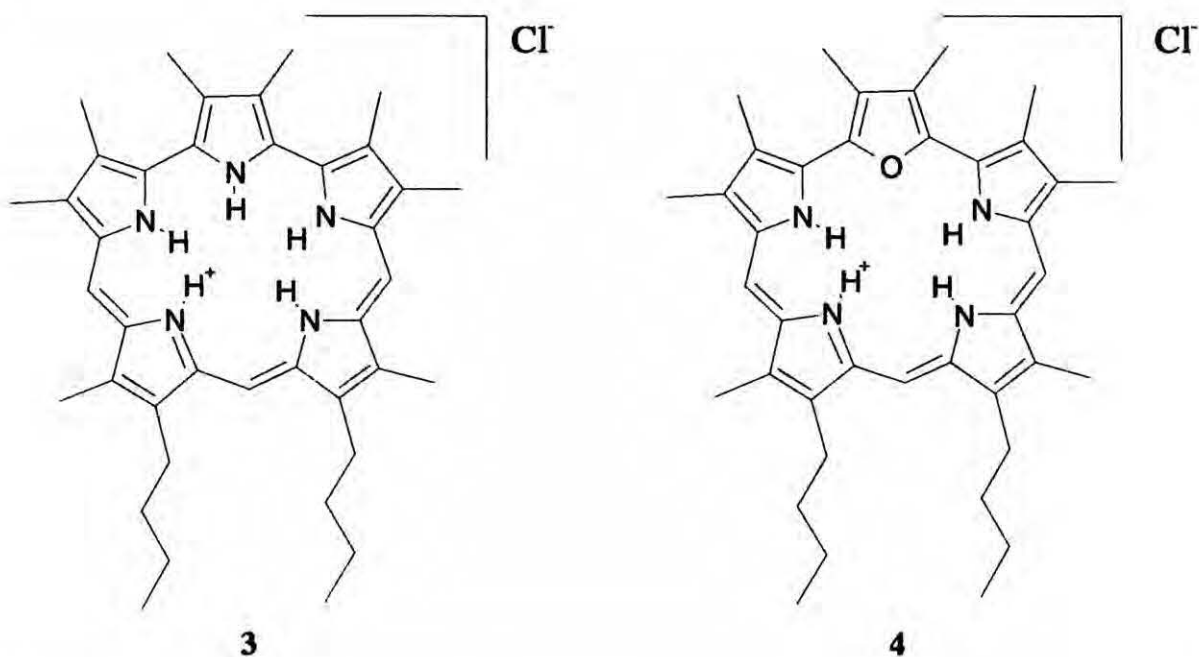
3   16,20-dibutyl-2,3,6,7,10,11,15,21-octamethyl-[22]pentaphyrin(1.1.0.1.0) (isosmaragdyrin - **IS**)

4   16,20-dibutyl-2,3,6,7,10,11,15,21-octamethyl-5-oxo-[22]pentaphyrin(1.1.1.0.0) (monoxoisosmaragdyrin - **MOIS**)

---

3 and **4** have been synthesized and purified in the group of Professor Jonathan L. Sessler (The University of Austin, Texas) using the procedure described previously.[17]
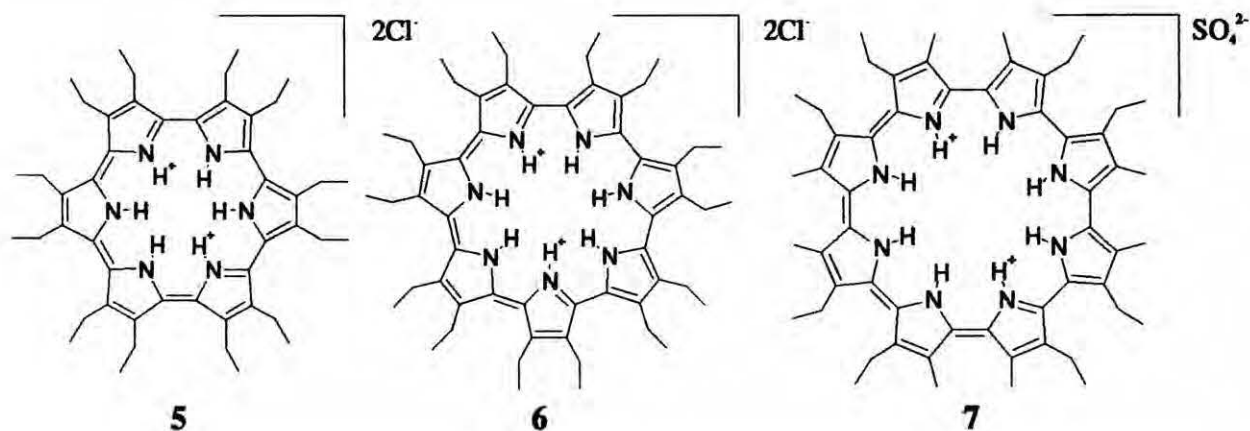
5   dihydrogen[2,3,6,7,10,11,14,15,18,19,22,23-dodecanethyl-[22]hexaphyrin(0.0.0.0.0.0) (**cyclo[6]pyrrole**)

6   dihydrogen[2,3,6,7,10,11,14,15,18,19,22,23,26,27-tetradecanethyl-[26]heptaphyrin(0.0.0.0.0.0.0) (**cyclo[7]pyrrole**)

7   dihydrogen[2,7,10,15,18,23,26,31-octaethyl-3,6,11,14,19,22,27,30-octamethyl-[30]octaphyrin(0.0.0.0.0.0.0.0)] (**cyclo[8]pyrrole**)

These isomers have been obtained from Professor J. Sessler. The synthesis and purification of **5-7** have been described previously.[18]
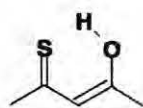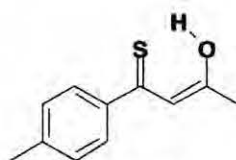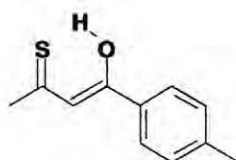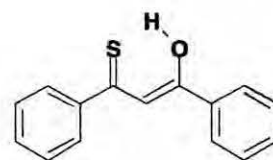
8	**9**	**10**	**11**

8	thioacetylacetone
9	*p*-methylbenzoylthioacetone
10	thio(*p*-methylbenzoyl)acetone
11	monothiodibenzoylmethane

8-10 were prepared and purified by Dr. Fritz Duus (University of Roskilde) using procedures described earlier.[19-20]

3.2. Spectral equipment

i. *Spectrophotometers*

The IR spectra in matrices, KBr tablets and solutions were recorded on a NICOLET SX 170, Fourier transform infrared spectrometer (FTIR).

Shimadzu UV 3100 spectrometer, equipped with a home-made temperature control system and an attachment for LD measurements was used for recording both LD and the electronic absorption spectra. The electronic absorption spectra were measured in solutions as well in cryogenic matrices and polymer sheets (LD).

ii. *Spectrofluorimeters*

Steady-state fluorescence and emission anisotropy spectra were obtained using an Edinburgh FS 900 CDT spectrofluorimeter (Edinburgh Analytic Instruments). Fluorescence excitation spectra were recorded at concentrations sufficiently low to ensure correspondence with the absorption. Fluorescence anisotropy was additionally measured on a Jasny spectrofluorimeter.[21] The emission quantum yields were determined using quinine sulfate in 0.1 N H_2SO_4 (ϕ_{fl}=0.51) as a standard.[22]

Fluorescence decays were obtained on an Edinburgh FL 900 CDT time-resolved spectrofluorometer (Edinburgh Analytic Instruments).

Transient absorption spectra were recorded on a home-built instrument[23] allowing a time resolution of 1 ns.

iii. *Spectropolarimeters*

MCD spectra were measured on a JASCO J-715 spectropolarimeter, equipped with a home-built permanent magnet (magnetic field 2.8 kG) or electromagnet (up to 5.0 kG) or on an OLIS DSM 17 CD spectropolarimeter with a permanent magnet (magnetic field 9.2 kG).

The basic components of an MCD spectrometer, shown in a Figure 3, are a photon source (L), a dispersive element (prism (Pr) or grating), a slit (S) that defines the spectral bandwidth, a polarizer (P) producing linearly polarized (LP) light which is converted by the photoelastic modulator (PEM) operating at 50 kHz into circularly polarized (CP) light.
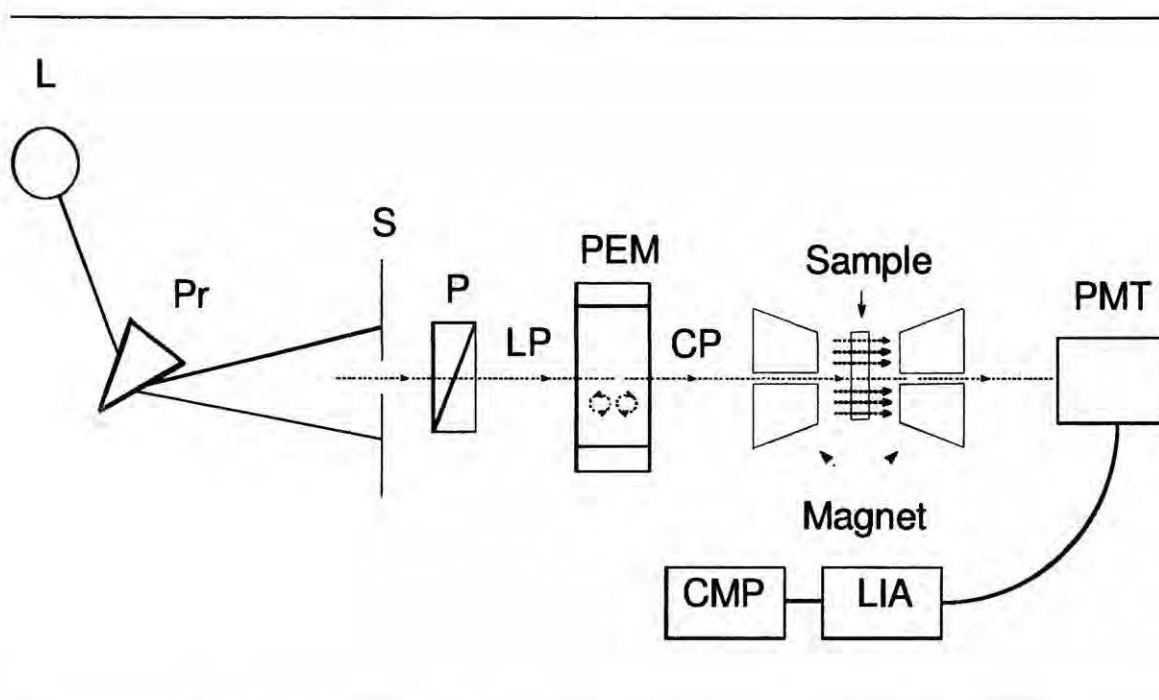
Figure 3.1.   The simple scheme of the classical MCD spectropolarimeter.

This CP light is incident on the sample (Sample), placed in a permanent magnet (Magnet) and the transmitted radiation is registered on a photodetector (PMT). If the sample is not optically active, both right- and left-handed photons are absorbed equally and the output of the detector is unmodulated. If, however, the sample is optically active, the detector current will be modulated at the PEM frequency with an amplitude proportional to the CD intensity:

$$CD = k(I_{AC} / I_{DC})$$ (3.1)

Here, k is the calibration constant, I_{AC} is intensity of the modulated signal, I_{DC} is the DC (direct current) level.

The modulated signal is extracted from the raw PMT output using a lock-in amplifier (LIA) whose output is digitized and transferred to a computer (CMP). For MCD measurements, the sample is placed in a longitudinal permanent magnetic field (coaxial with the light beam).

The dual beam OLIS DSM 17 CD MCD spectropolarimeter is based on a modified Cary 17 optics bench that provides a broad spectral range from 185 nm in the UV to 2600 nm in the near infrared (NIR), a range particularly important for spectroscopy of cyclic π-conjugated systems. Moreover, two-beam spectropolarimeter has some advantages in comparison with a single beam one. The most important one is that the absorption for right and left-handed polarized light is measured simultaneously. The signal obtained for right circularly polarized light is directly subtracted from that for left circularly polarized light:

$$CD = abs_L - abs_R$$ (3.2)

Therefore, both, the calibration against a standard and LIA are not required.

The sample is placed in a permanent magnet of about 9 kG (0.9 Tesla) magnetic field strenght. The value of the magnetic field strength was determined using the MCD signal of aqueous $CoSO_4$ solution as a standard.[24] The spectrometer is completely interfaced to a PC for data collection and analysis.

iv. *Light sources*

The photooriented samples for LD measurements in the IR region were obtained using a Coherent Innova 300 argon laser or a 300 W xenon lamp (ILC), equipped with a home-built monochromator and polarizer.

Samples preparation for linear dichroism

LD measurements in the UV/VIS region were performed on uniaxially oriented stretched samples of polyethylene (PE), containing a small amount of the investigated species. The compounds were embedded into PE by placing the powder sample on a polymer sheet and gradually adding droplets of chloroform. After several hours, the film was carefully washed by methanol to avoid formation of microcrystals on the surface.

LD experiments in the IR region were made on photochromic compounds isolated in rare gas matrices at low temperatures, usually 10-20 K. If the lifetime of a photoproduct of a photochromic molecule is much longer then the time of experiment (for β-thioxoketones the estimated lifetime of the photoproduct at 20 K is more than thousands years), the sample uniaxially oriented by polarized light is easy to obtain. The rare gas matrix is a medium with an isotropic orientation of guests. Upon polarized light irradiation, the light attenuated by the matrix is absorbed mostly by molecules with the same direction of the dipole moment transition as the direction of the light polarization. Therefore, a photoreaction occurs in a selected group of molecules and, subsequently, there are two kinds of molecules present in a matrix after the irradiation and phototransformation: the oriented photoproduct and the partially aligned initial form.

3.2. Cryogenic techniques

i. *Close-cycle helium cryostats*

Rare gas matrices were produced using close-cycle cryostats Displex 202 or Displex DE-204S and a home-built matrix deposition vacuum system.

ii. *Liquid nitrogen cryostat*

The anisotropy of fluorescence at a liquid nitrogen temperature was recorded in a liquid helium cryostat, produced by the Institute of Physics of the Polish Academy of Sciences.

Sample preparation for matrix deposition

Matrices are formed by condensation of a gas stream on a cold window. The gas stream consists of guest and host molecules in the appropriate mixture. Sample preparation involves the gas flow and vaporization of materials. The gas is admitted through a controlled valve. The gases effuse from an orifice which is situated close to the deposition window. The gas beam characteristics are defined by the size of the orifice and the distance between the orifice and the target window.

The crystalline substances are placed during deposition into a glass heater, which is warmed up to about 2/3 of the substance melting point. The vapor of the substance is mixed with a stream of matrix gas and deposited onto the target window held at appropriate temperature. The temperature of the target window depends on the matrix gas and deposition speed or the type of the experiment.

The deposition of liquid samples is more complicated. Rare gas matrices were produced by mixing the substance, contained in a glass tube at the appropriate temperature, with matrix gas. The liquid sample must be cooled down to about 2/3 of the substance melting point. Prior to deposition, the compound is cooled with liquid nitrogen and degassed several times under vacuum by a standard freeze-thaw technique in order to remove oxygen from the sample. The following procedure of the deposition remains the same as for a crystalline sample. For example, thioacetylacetone, one of the of β-thioxoketones, which is a liquid at room temperature, was cooled down to 258 K and mixed with a stream of matrix

gas; this was followed by deposition onto a KBr window held at 25 K (argon) or 45 - 55 K (xenon) in a Displex 202 cryostat.

Rare gas matrices of the rest of β-thioxoketones were produced by deposition of the sample into a stream of gas onto a KBr window held at 25 K (argon) or 45-55 K (xenon) in a Displex 202 cryostat. The compounds, contained in a glass heater, were heated in a range of 320-350 K, depending on their melting points.

Concentration and deposition speed

The goals of spectroscopic experiments are to determine the inherent properties of molecules such as lifetimes, transition energies and polarizations, vibrational frequencies and so on. The presence of chemical or physical interactions between guest molecules influences the properties being observed. Therefore, good isolation of the excited species is required.

The rate of gas deposition depends on many factors, such as cooling capacity of the refrigerator, condensation characteristics of the gas, matrix thickness, and type of the experiment. In most cases the rate has been empirically established as a compromise between opposite goals to obtain: a well-annealed sample with minimum solute diffusion, a sample with a good optical quality or with a defined spectral property (the minimum of sites or the fine spectral structure). For emission studies, sometimes a "snowy" matrix is preferred due to its ability to scatter efficiently the exciting light.

At the start and at the end of matrix preparation the deposition of a thin layer of pure rare gas is recommended. Therefore, the matrix is sandwiched between two layers of pure crystal. This suppresses surface effects due to guest diffusion, impurity absorption or premature matrix evaporation.

3.4. Calculations

Molecular ground-state equilibrium geometries, harmonic force-fields, and vibrational IR spectra were predicted by B3LYP/cc-pVDZ and B3LYP/cc-pVTZ (hybrid density functional[25] in combination with the Lee-Yang-Parr correlation functional (B3LYP)[26]) density functional theory (DFT)[27-28] using Gaussian 98[29] and Gaussian 03[30] suites of programs.

Calculations of excited-state energies, oscillator strengths, and Faraday *A* and *B* terms for expanded and isomeric porphyrins were performed using the INDO/S method[31] (DZDO program, kindly provided by Josef Michl and John Downing). Here, the X-ray results or the AM1[32] optimized geometries were used as input.

Chapter 4. Characterization of excited states of constitutional isomers of porphyrin and expanded porphyrins

4.1. Hemiporphycene and corrphycene

In this part of the work the results of the investigation of two molecules, octaethyl derivatives of hemiporphycene (porphyrin-(2.1.1.0)) and corrphycene (porphyrin-(2.1.0.1)) (1 and 2, respectively, see Chart 4.1) are presented.

1   2
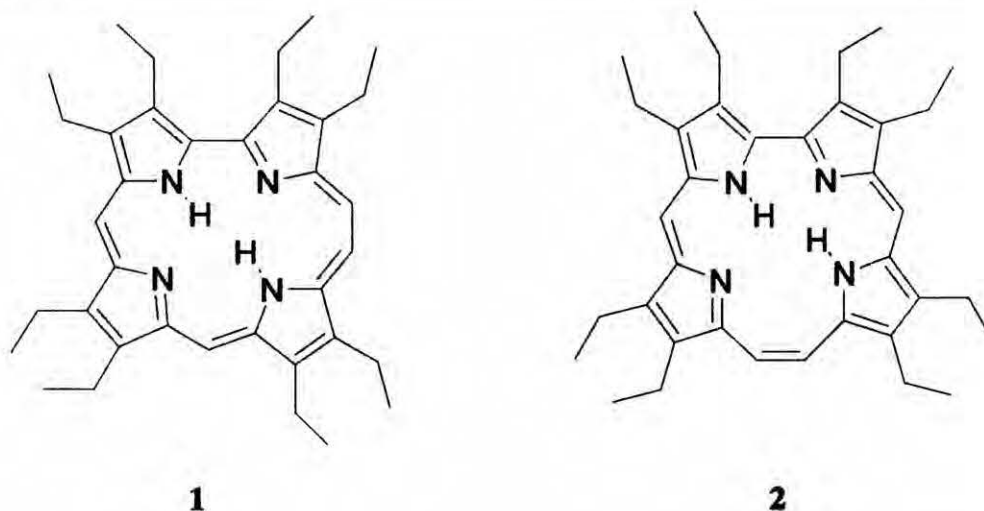
Chart 4.1.   Octaethyl derivatives of hemiporphycene (left) and corrphycene.

These molecules, along with porphycene (porphyrin-(2.0.2.0)) and isoporphycene (porphyrin-(3.0.1.1)) are constitutional isomers of porphyrin (porphyrin-(1.1.1.1)) (Chart 4.2) which have been synthesized in the last decade.
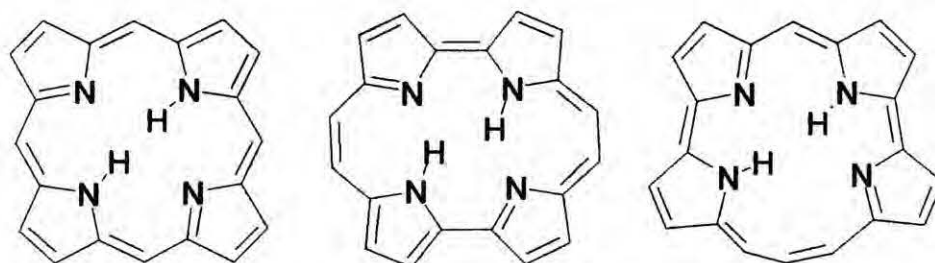
Chart 4.2.   Left to right: porphyrin, porphycene and isoporphycene.

The spectral and electronic properties of such species are a subject of much study due to the importance for fundamental research. In addition, investigations of porphyrin isomers are also promoted by prospects of use in various areas, ranging from the design of artificial photosynthetic systems,[33-34] sensors,[35] molecular optoelectronic devices,[36] photoswitches,[37] optical memories[38] and conductive polymers,[39] to applications in photodynamic therapy.[40] In fact, porphycene has already been shown to be a very promising candidate as a phototherapeutic agent.[41] Since all these techniques are based on using a chemical substance and its interactions with light, a prerequisite for a successful application is a detailed understanding of the spectroscopy and photophysics of the lowest excited electronic states.

In addition to experimental measurements, the investigations included calculations of relative stabilities, geometries, as well as predictions of spectral and electronic properties.[42]

The electronic transitions assignment is based on the perimeter model predictions,[43-44] followed by high-level calculation. This procedure allows us to deal with both absorption as well as MCD spectra. In this work, we investigated the electronic absorption spectra of neutral, doubly protonated and doubly deprotonated forms of 1 and 2. Using the nomenclature of the perimeter model, 1 belongs to "negative hard" chromophores and should therefore exhibit porphycene-like behavior. On the contrary, 2 is similar to porphyrin and can be classified as a "soft" chromophore.

The absorption and MCD spectra for neutral, doubly protonated and doubly deprotonated forms of 1 and 2 are presented in Figures 4.1-4.6, respectively. Included in the Figures are also the INDO/S theoretical predictions regarding the transition energies and MCD B terms.

The TD-DFT calculated values of excited state energies for the neutral and charged forms of the unsubstituted compounds are shown in Tables 4.1-4.8, along with the experimentally obtained values for the octaalkylated compounds.
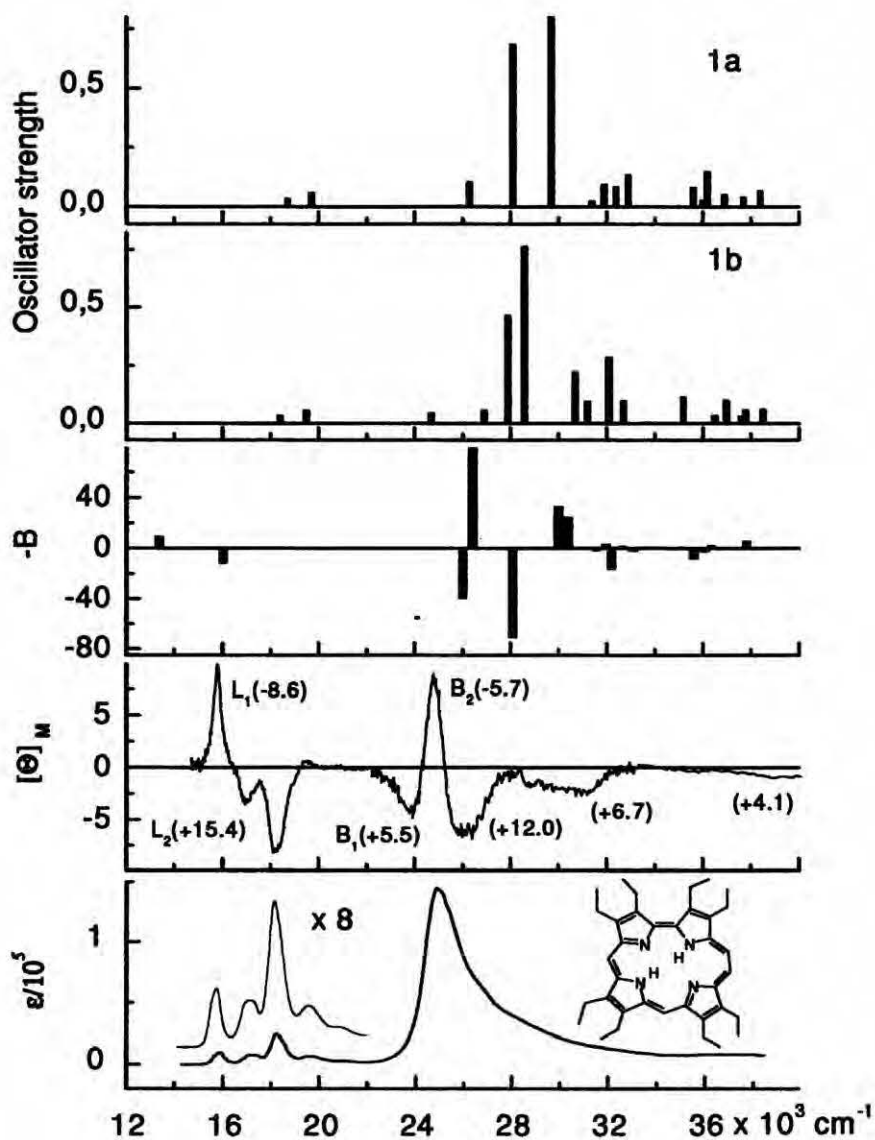
Figure 4.1. Bottom, electronic absorption; middle, MCD spectra (B term values $(D^2\mu_B/cm^{-1})$ in parentheses); top, the results of INDO/S calculations for the tautomeric form **1a** (cf. Chart 4.3). The calculated values of B terms and oscillator strength are indicated by the bars. The spectra were recorded in acetonitrile at 293 K.
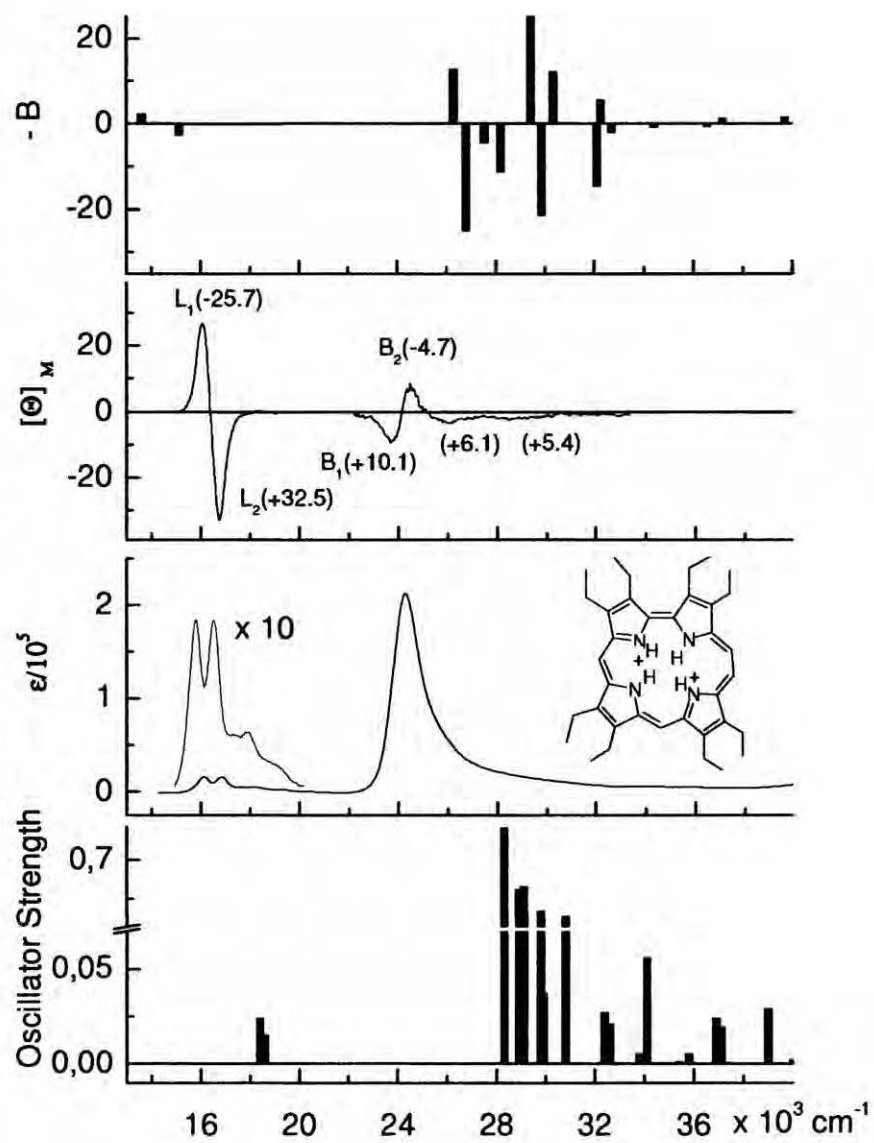
Figure 4.2. Bottom, electronic absorption; middle, MCD spectra; top, the results of INDO/S calculations for the doubly protonated form of **1**. The spectra were recorded in acetonitrile solution containing perchloric acid at 293 K. See caption to Figure 4.1 for details.
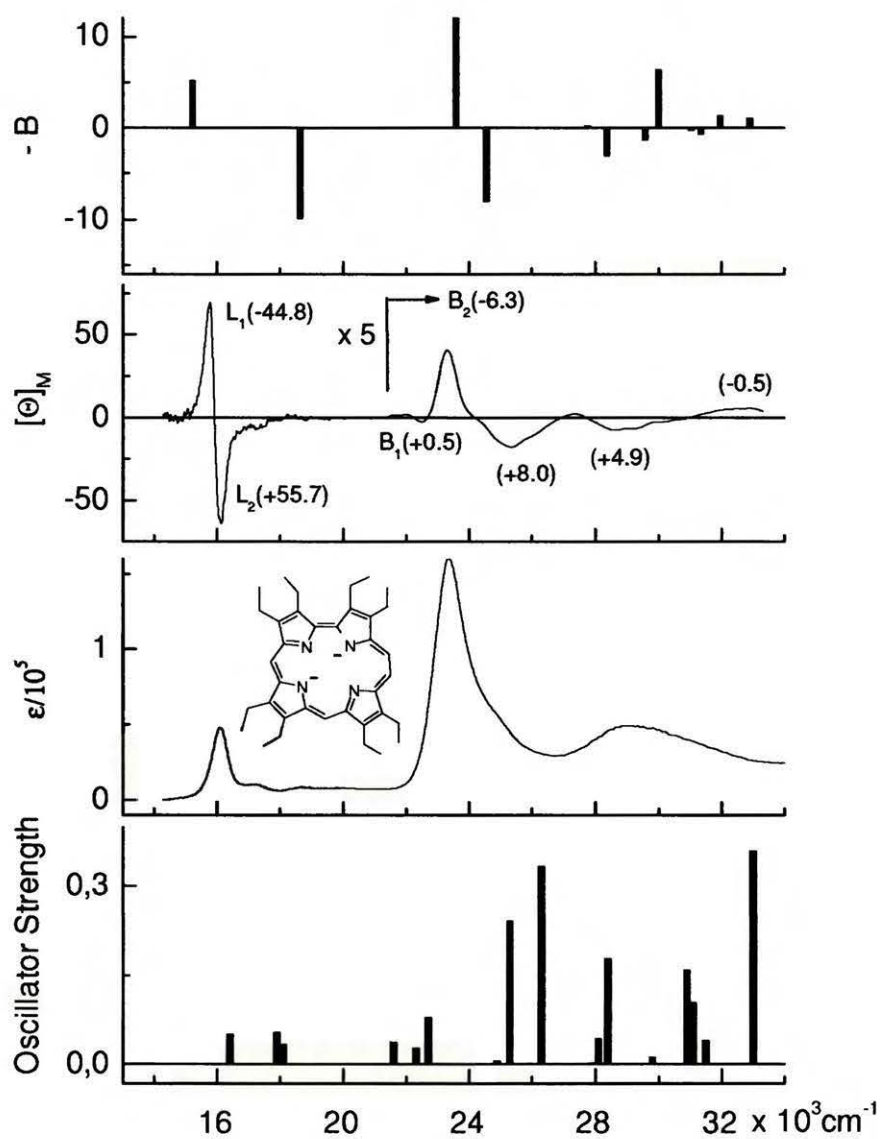
Figure 4.3. Bottom, electronic absorption; middle, MCD spectra; top, the results of INDO/S calculations for the doubly deprotonated form of **1**. The spectra were recorded in a KOH-saturated DMSO solution at 293 K. See caption to Figure 4.1 for details.
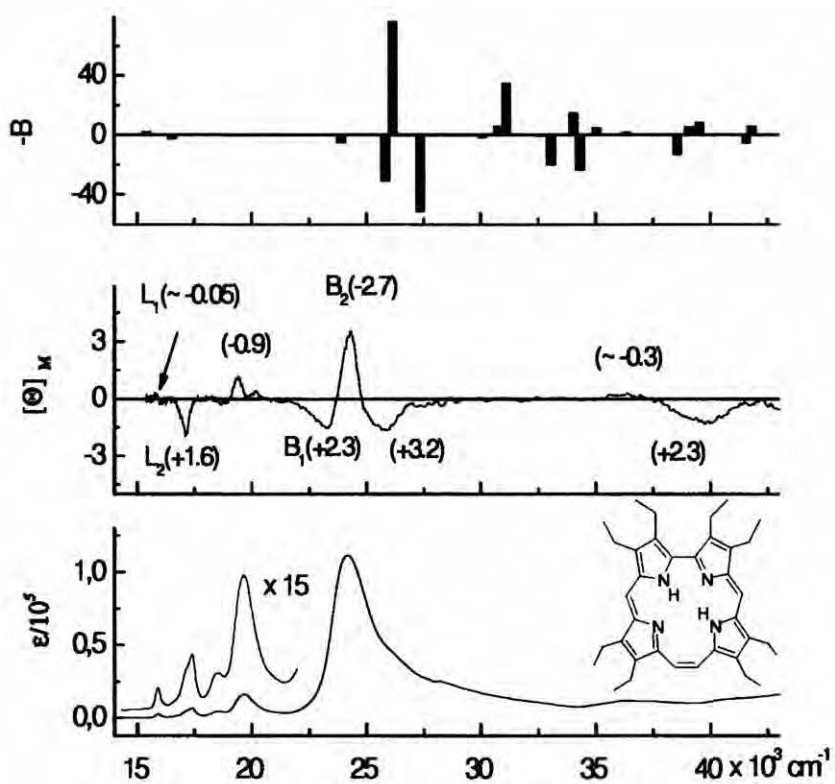
Figure 4.4. Bottom, electronic absorption; middle, MCD spectra, the values of B terms ($D^2\mu_B/cm^{-1}$) given in parentheses; top, the results of INDO/S calculations for **2**. The heights of the bars reflect the calculated values of B terms and oscillator strengths. The spectra were recorded in acetonitrile at 293 K.
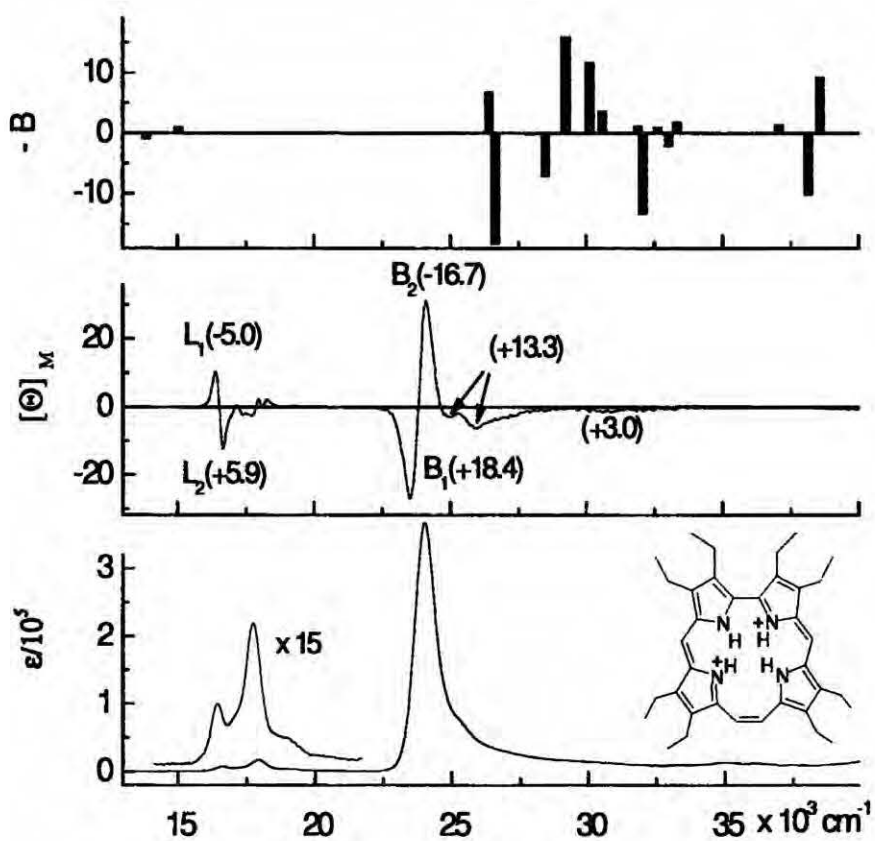
Figure 4.5. Bottom, electronic absorption; middle, MCD spectra, top, the results of INDO/S calculations for the doubly protonated form of **2**. The spectra were recorded in acetonitrile containing perchloric acid at 293 K. See caption to Figure 4.4 for details.
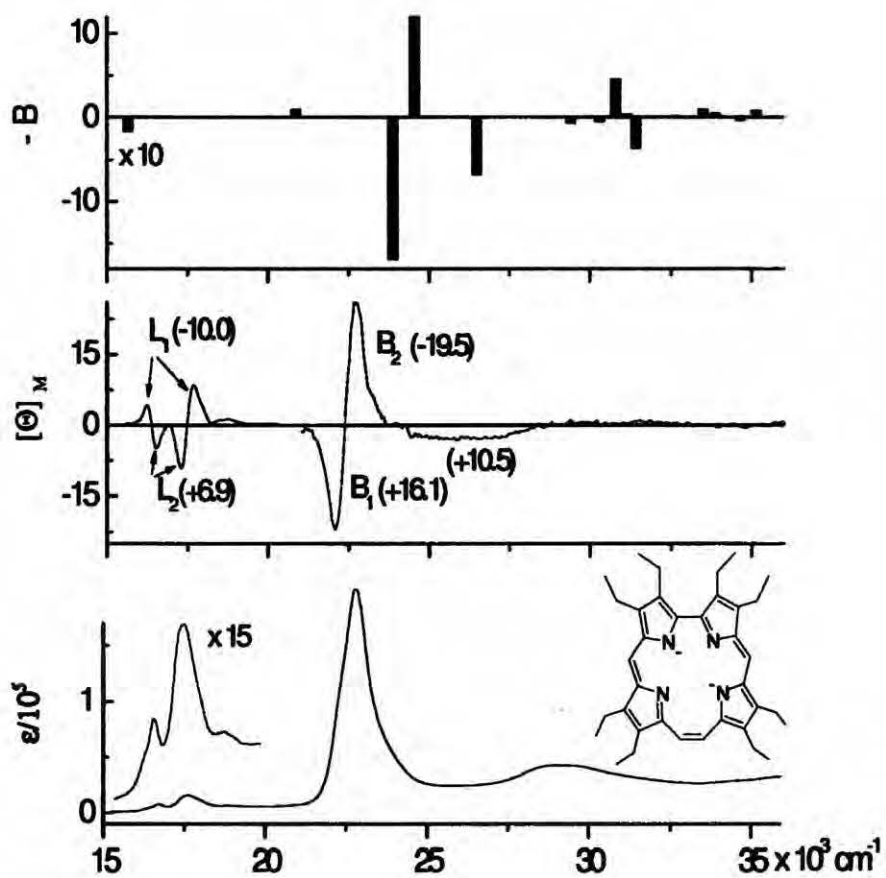
Figure 4.6. Bottom, electronic absorption; middle, MCD spectra; top, the results of INDO/S calculations for the doubly deprotonated form of **2**. The spectra were recorded in KOH-saturated DMSO solution at 293 K. See caption to Figure 4.4 for details.

Table 4.1. Calculated (TD-B3LYP/6-31G**) electronic states of the tautomer **1a** of neutral parent hemiporphycene and the experimental values obtained for the octaethyl derivative.

	Calc. Energy[a] $[10^3 \text{ cm}^{-1}]$	Oscillator strength	Dominant configuration[b]	Exp. Energy[c] $[10^3 \text{ cm}^{-1}]$
1	18.7	0.037	0.57 (1 −1)	15.8
2	19.7	0.061	0.55 (2 −1)	16.9
3	25.9	0.006	0.67 (3 −1)	
4	26.3	0.106	0.57 (4 −1)	23.9
5	28.1	0.684	0.46 (1 −2)	24.8
6	29.7	0.801	0.36 (2 −2)	26.1
7	31.2	0.000	0.64 (7 −1)	
8	31.4	0.026	0.59 (5 −1)	
9	31.4	0.000	0.64 (6 −1)	
10	31.9	0.095	0.59 (3 −2)	
11	32.4	0.085	0.67 (4 −2)	
12	32.9	0.136	0.66 (6 −1)	31.2
13	35.6	0.083	0.44 (9 −1), 0.43(2 −2)	
14	36.0	0.027	0.44 (6 −2), 0.41(5 −2)	
15	36.2	0.001	0.69 (7 −2)	
16	36.2	0.150	0.57 (1 −3)	35.8
17	36.4	0.001	0.69 (8 −2)	
18	36.9	0.053	0.49 (6 −2)	39.4
19	37.7	0.041	0.46 (10 −1)	
20	38.4	0.069	0.40 (2 −3)	

[a] calculated for the unsubstituted molecule; [b]the occupied orbitals are numbered 1, 2, ... downwards, the unoccupied ones, -1, -2...upwards; [c]experimental results for room temperature solution of **1**, with the **1a:1b** ratio of about 7:3.[46]

Table 4.2. Calculated (TD-B3LYP/6-31G**) electronic states of the tautomer **1b** of neutral parent hemiporphycene and the experimental values obtained for the octaethyl derivative. See captions to Table 4.1 for details.

	Calc. Energy $[10^3 \text{ cm}^{-1}]$	Oscillator strength	Dominant configuration	Exp. Energy $[10^3 \text{ cm}^{-1}]$
1	18.4	0.035	0.55 (2 −1)	15.8
2	19.5	0.057	0.55 (1 −1)	16.9
3	24.7	0.045	0.61 (3 −1)	
4	26.9	0.056	0.62 (4 −1)	
5	27.9	0.465	0.33 (4 −1), 0.32 (1 −2)	23.9
6	28.6	0.763	0.46 (2 −2)	24.8
7	30.7	0.222	0.50 (4 −2)	26.1
8	31.0	0.000	0.69 (6 −1)	
9	31.2	0.093	0.57 (3 −2)	
10	32.0	0.000	0.70 (8 −1)	
11	32.1	0.285	0.55 (5 −1)	31.2
12	32.7	0.096	0.65 (6 −1)	
13	34.6	0.000	0.68 (7 −2)	
14	35.2	0.116	0.52 (1 −3)	35.8
15	36.5	0.034	0.55 (2 −3)	
16	36.7	0.001	0.67 (8 -2)	
17	37.0	0.102	0.61 (5 −2)	
18	37.6	0.030	0.45 (6 −2)	
19	37.8	0.058	0.42 (10 −1)	
20	38.5	0.063	0.49 (6 −2)	39.4

Table 4.3. Calculated (TD-B3LYP/6-31G**) electronic states of the doubly protonated form of parent hemiporphycene and the experimental values obtained for the octaethyl derivative. See captions to Table 4.1 for details.

	Calc. Energy $[10^3 \text{ cm}^{-1}]$	Oscillator strength	Dominant configuration	Exp. Energy[a] $[10^3 \text{ cm}^{-1}]$
1	18.4	0.024	0.48 (1 –1)	16.1
2	18.6	0.015	0.43 (1 –2)	16.7
3	28.3	0.989	0.41 (1 –2)	23.7
4	28.9	0.429	0.52 (3 –1)	24.5
5	29.1	0.460	0.43 (3 –1)	26.1
6	29.8	0.232	0.57 (5 –1)	28.6
7	29.9	0.037	0.64 (6 –1)	
8	30.8	0.193	0.59 (4 –1)	
9	32.4	0.027	0.65 (4 –2)	
10	32.6	0.021	0.67 (3 –2)	
11	33.8	0.005	0.64 (5 –2)	
12	34.1	0.056	0.67 (6 –2)	
13	35.4	0.001	0.54 (7 –1)	
14	35.8	0.005	0.50 (8 –1)	
15	36.9	0.024	0.42 (7 –2)	
16	37.1	0.019	0.38 (1 –3)	
17	39.0	0.029	0.39 (1 –4)	
18	40.0	0.002	0.50 (8 –2)	
19	44.1	0.031	0.30 (1 –4)	
20	44.8	0.005	0.61 (9 –1)	

[a]room temperature solution of **1** in acetonitrile containing perchloric acid.

Table 4.4. Calculated (TD-B3LYP/6-31G**) and observed electronic states of the hemiporphycene dianion and the experimental values obtained for the octaethyl derivative. See captions to Table 4.1 for details.

	Calc. Energy $[10^3 \text{ cm}^{-1}]$	Oscillator strength	Dominant configuration	Exp. Energy[a] $[10^3 \text{ cm}^{-1}]$
1	16.4	0.051	0.49 (1 -1)	15.8
2	17.9	0.054	0.41 (1 -2)	16.1
3	18.1	0.034	0.56 (3 -1)	
4	21.6	0.037	0.44 (4 -1)	
5	22.7	0.079	0.42 (4 -1), 0.38 (5 -1)	
6	22.3	0.027	0.46 (3 -2)	
7	24.9	0.006	0.65 (6 -1)	
8	25.3	0.242	0.41 (4 -1)	22.5
9	26.3	0.334	0.45 (2 -2)	23.3
10	27.9	0.003	0.60 (4 -2)	
11	28.1	0.043	0.58 (8 -1)	
12	28.4	0.179	0.48 (7 -1)	25.3
13	29.8	0.012	0.52 (6 -2)	
14	30.9	0.160	0.58 (5 -2)	
15	31.1	0.105	0.53 (9 -1)	
16	31.3	0.001	0.47 (10 -1)	
17	31.5	0.040	0.51 (6 -2), 0.36 (1 -3)	
18	33.0	0.360	0.48 (1 -3)	28.9
19	34.3	0.005	0.67 (7 -2)	
20	35.1	0.222	0.55 (2 -4)	

[a] room temperature solution of **1** in KOH-saturated dimethylsulfoxide.

Table 4.5. Calculated (TD-B3LYP/6-31G**) electronic states of neutral parent corrphycene and the energies observed for the octaethyl derivative.

	Calc. Energy[a] $[10^3\ cm^{-1}]$	Oscillator strength	Dominant configuration[b]	Exp. Energy[c] $[10^3\ cm^{-1}]$
1	18.7	0.037	0.57 (1 –1)	15.8
2	19.7	0.061	0.55 (2 –1)	17.2
3	25.9	0.006	0.67 (3 –1)	
4	26.3	0.106	0.57 (4 –1)	23.3
5	28.1	0.684	0.46 (1 –2)	24.2
6	29.7	0.801	0.36 (2 –2)	25.8
7	31.2	0.000	0.64 (7 –1)	
8	31.4	0.026	0.59 (5 –1)	
9	31.4	0.000	0.64 (6 –1)	
10	31.9	0.095	0.59 (3 –2)	
11	32.4	0.085	0.67 (4 –2)	
12	32.9	0.136	0.66 (6 –1)	~31.0 (sh)
13	35.6	0.083	0.44 (9 –1), 0.43(2 –2)	
14	36.0	0.027	0.44 (6 –2), 0.41 (5 –2)	
15	36.2	0.001	0.69 (7 –2)	
16	36.2	0.150	0.57 (1 –3)	~36.0
17	36.4	0.001	0.69 (8 –2)	
18	36.9	0.053	0.49 (6 –2)	
19	37.7	0.041	0.46 (10 –1)	
20	38.4	0.069	0.40 (2 –3)	39.9

[a] calculated for the unsubstituted molecule; [b] the occupied orbitals are numbered 1, 2, ... downwards, the unoccupied ones, -1, -2...upwards; [c] experimental results for room temperature solution of **2**.

Table 4.6.   Calculated (TD-B3LYP/6-31G**) electronic states of the parent corrphycene dianion and the observed values for the octaethyl derivative. See captions to Table 4.5 for details.

	Calc. Energy [10^3 cm^{-1}]	Oscillator strength	Dominant configuration	Exp. Energy [10^3 cm^{-1}]
1	18.4	0.035	0.55 (2 –1)	16.2
2	19.5	0.057	0.55 (1 –1)	16.6
3	24.7	0.045	0.61 (3 –1)	
4	26.9	0.056	0.62 (4 –1)	
5	27.9	0.465	0.33 (4 –1), 0.32 (1 –2)	22.10
6	28.6	0.763	0.46 (2 –2)	22.7
7	30.7	0.222	0.50 (4 –2)	~26
8	31.0	0.000	0.69 (6 –1)	
9	31.2	0.093	0.57 (3 –2)	
10	32.0	0.000	0.70 (8 –1)	
11	32.1	0.285	0.55 (5 –1)	~29
12	32.7	0.096	0.65 (6 –1)	
13	34.6	0.000	0.68 (7 –2)	
14	35.2	0.116	0.52 (1 –3)	
15	36.5	0.034	0.55 (2 –3)	
16	36.7	0.001	0.67 (8 -2)	
17	37.0	0.102	0.61 (5 –2)	
18	37.6	0.030	0.45 (6 –2)	
19	37.8	0.058	0.42 (10 –1)	
20	38.5	0.063	0.49 (6 –2)	

Table 4.7. Calculated (TD-B3LYP/6-31G**) electronic states of the more stable energetically form, (a), of doubly protonated parent corrphycene (see Figure 4.11) and the experimental values obtained for the octaethyl derivative. See captions to Table 4.5 for details.

	Calc. Energy $[10^3 \text{ cm}^{-1}]$	Oscillator strength	Dominant configuration	Exp. Energy[a] $[10^3 \text{ cm}^{-1}]$
1	18.4	0.024	0.48 (1 –1)	16.4
2	18.6	0.015	0.43 (1 –2)	16.7
3	28.3	0.989	0.41 (1 –2)	23.5
4	28.9	0.429	0.52 (3 –1)	24.1
5	29.1	0.460	0.43 (3 –1)	25.9
6	29.8	0.232	0.57 (5 –1)	
7	29.9	0.037	0.64 (6 –1)	
8	30.8	0.193	0.59 (4 –1)	~31
9	32.4	0.027	0.65 (4 –2)	
10	32.6	0.021	0.67 (3 –2)	
11	33.8	0.005	0.64 (5 –2)	
12	34.1	0.056	0.67 (6 –2)	
13	35.4	0.001	0.54 (7 –1)	
14	35.8	0.005	0.50 (8 –1)	
15	36.9	0.024	0.42 (7 –2)	
16	37.1	0.019	0.38 (1 –3)	
17	39.0	0.029	0.39 (1 –4)	
18	40.0	0.002	0.50 (8 –2)	
19	44.1	0.031	0.30 (1 –4)	
20	44.8	0.005	0.61 (9 –1)	

[a]room temperature solution of **2** in acetonitrile containing perchloric acid.

Table 4.8.   Calculated (TD-B3LYP/6-31G**) electronic states of the less stable energetically form, (b), of doubly protonated corrphycene (see Figure 4.11) and the experimental values obtained for the octaethyl derivative. See captions to Table 4.5 for details.

	Calc. Energy $[10^3 \text{ cm}^{-1}]$	Oscillator strength	Dominant configuration	Exp. Energy[a] $[10^3 \text{ cm}^{-1}]$
1	18.4	0.024	0.48 (1 −1)	16.4
2	18.6	0.015	0.43 (1 −2)	16.7
3	28.3	0.989	0.41 (1 −2)	23.5
4	28.9	0.429	0.52 (3 −1)	24.1
5	29.1	0.460	0.43 (3 −1)	25.9
6	29.8	0.232	0.57 (5 −1)	
7	29.9	0.037	0.64 (6 −1)	
8	30.8	0.193	0.59 (4 −1)	~31
9	32.4	0.027	0.65 (4 −2)	
10	32.6	0.021	0.67 (3 −2)	
11	33.8	0.005	0.64 (5 −2)	
12	34.1	0.056	0.67 (6 −2)	
13	35.4	0.001	0.54 (7 −1)	
14	35.8	0.005	0.50 (8 −1)	
15	36.9	0.024	0.42 (7 −2)	
16	37.1	0.019	0.38 (1 −3)	
17	39.0	0.029	0.39 (1 −4)	
18	40.0	0.002	0.50 (8 −2)	
19	44.1	0.031	0.30 (1 −4)	
20	44.8	0.005	0.61 (9 −1)	

[a]room temperature solution of **2** in acetonitrile containing perchloric acid.

The absorption spectra of the investigated molecules reveal a pattern which is characteristic for porphyrin and its derivatives: weak bands in the low-energy range (so-called Q-region), followed at higher energies by an intense band (named Soret region). The Q/Soret intensity ratio is significantly higher than in porphyrin, but lower than in porphycene.[6] The MCD spectra reveal the presence of two electronic transitions in the Q region, with the same -,+ sign pattern for all forms (it should be recalled that a positive MCD sign corresponds to a negative value of the B term, and *vice versa*). In the Soret region, MCD curves reveal a presence of an additional electronic transition, located to the blue of the two Soret bands.

The sequence of the signs of B terms observed for all forms of corrphycene is -, +, +, - The MCD intensity is very weak in the region of Q bands and much stronger in the Soret region. This pattern is characteristic of porphyrin[45] and completely opposite to that observed for porphycene[6] and hemiporphycene, in which the MCD signals of the first two excited states are much stronger than those for the Soret bands. The relative absorption intensities of the Q *vs.* Soret bands are much stronger for hemiporphycene and, in particular, porphycene, while corrphycene resembles porphyrin also in this respect. Finally, regular changes in the pattern of vibronic activity are observed along the series. In porphyrin and corrphycene, weak 0-0 bands for both Q transitions are followed by much stronger vibronic components. On the contrary, in porphycene the 0-0 bands dominate. Hemiporphycene represents an intermediate case, with intensities of 0-0 transitions comparable to those of the strongest vibronic components.

Before analyzing the spectra using the perimeter model,[43-44] it makes a sense to briefly recall its main features relevant for the present case. Hemiporphycene as well as corrphycene chromophores can formally be derived from a [20]annulene dication, $C_{20}H_{20}^{2+}$ perimeter containing $4N+2=18$ π-electrons. The two molecules are obtained from unperturbed

perimeter by bridging with two -NH- groups and two -N⁻ groups (Figures 4.7 and 4.8). The choice of a doubly positively charged 18-electron [20]annulene as a starting point is dictated by the fact that charged 4N+2 perimeters have a degenerate pair of low lying L_1, L_2 states, whereas another possible selection is a neutral [18]annulene, which exhibits a large splitting between these states. Since the L_1 and L_2 states lie very close in porphyrin, and even closer in porphycene[6], the derivation of our chromophore from a charged [20]annulene perimeter represents a much smaller perturbation than the alternative case of starting from an uncharged [18]annulene.
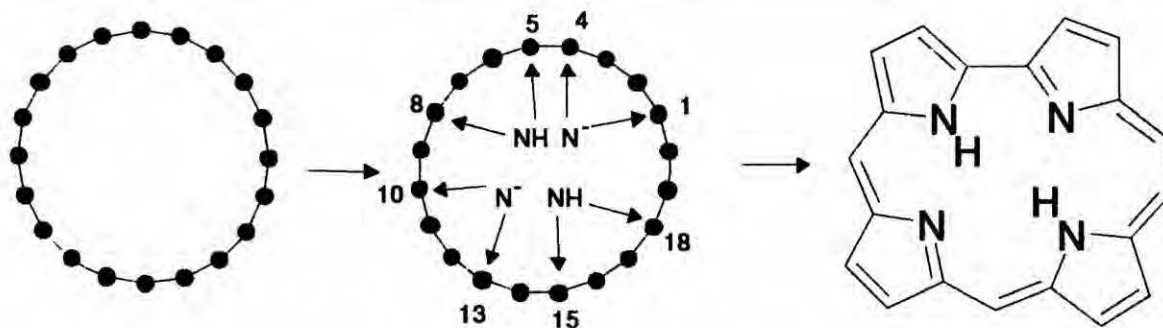
Figure 4.7. Formal derivation of hemiporphycene from an 18 π electron perimeter, the [20]annulene dication ($C_{20}H_{20}^{2+}$).
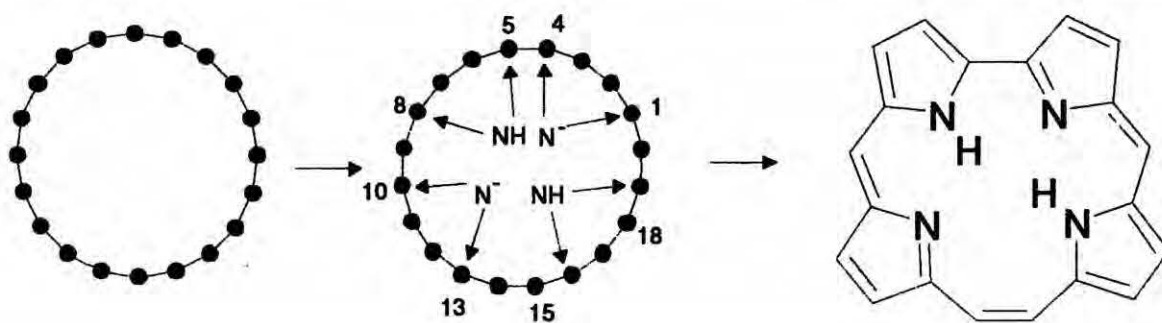
Figure 4.8. Formal derivation of corrphycene from an 18 π electron perimeter, the [20]annulene dication.

The electronic states considered are those derived from four singly excited configurations corresponding to excitations from the two highest occupied (HOMO) π-orbitals into two lowest unoccupied (LUMO) π-orbitals. Configuration interaction produces four states, labeled L_1, L_2, B_1 and B_2 in the order of increasing energy. In porphyrin and its derivatives the lower two transitions are usually referred to as Q, while the two higher ones are known as the Soret bands. The degree of mixing of the L states with the B states can be expressed by the values of the parameters α and β, which, in turn, are simple functions of the splittings of the initially degenerate HOMO and LUMO pairs, Eqs. 1.18-1.21. The corresponding values of the B terms are described by Eqs. 1.28-1.29.

The origins for the soft character of the corrphycene chromophores or the hard character of the hemiporphycene are easy to understand by inspecting the shape of the molecular orbitals of the parent perimeter. This allows to predict the response of each orbital to structural perturbations that lead to **1** or **2**. These responses are shown in Figure 4.9 or 4.10, for hemiporphycene and corrphycene, respectively.
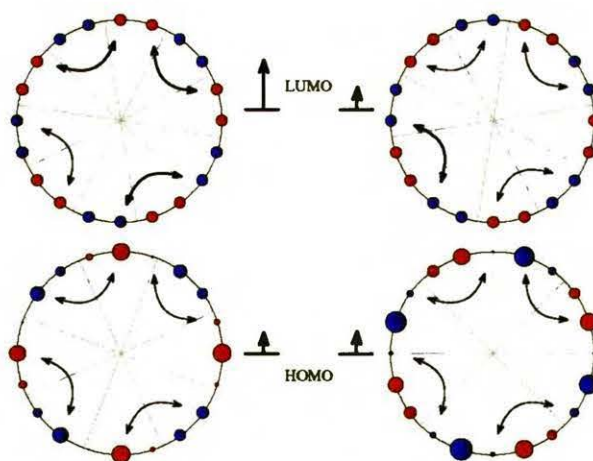
Figure 4.9. The shapes of the HOMO and LUMO orbitals of the parent $C_{20}H_{20}^{2+}$ perimeter and the expected energy shifts caused by the perturbations corresponding to the formation of hemiporphycene.
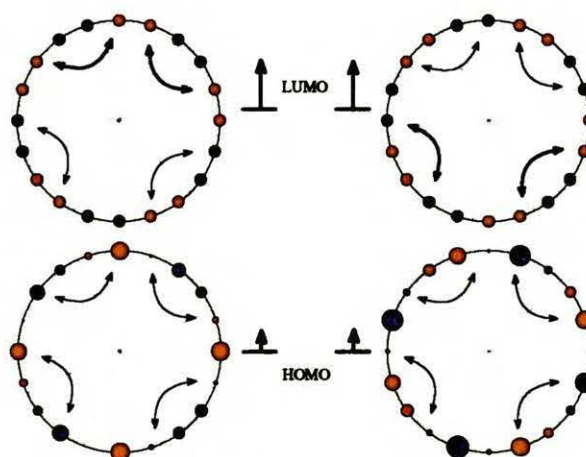
Figure 4.10. The shapes and nodal planes of the HOMO and LUMO orbitals of the parent $C_{20}H_{20}^{2+}$ perimeter, and the predicted response to the perturbation corresponding to the formation of corrphycene.

The bridging will have a significant effect on the energy of a molecular orbital if (i) the LCAO coefficients at the positions of bridging are large, and (ii) the bridging group does not lie in the nodal plane. Therefore, in the case of corrphycene, none of the HOMO orbitals should undergo a significant shift upon bridging, and thus no significant splitting is expected. The two LUMO orbitals are pushed to higher energies: each, however, by the same amount. Again, no splitting is expected. The same situation is encountered for porphyrin. On the other hand, the topology of porphycene dictates a completely different behavior: four bridges raise the energy of one of the LUMO orbitals, leaving the other orbital unaffected.[42] In hemiporphycene, three bridges affect the energy of one component of the LUMO pair, whereas only one bridge raises the energy of the other component.[42] These simple considerations explain why porphyrin and corrphycene are soft chromophores, whereas porphycene and hemiporphycene reveal negative-hard character, stronger in the former.

Since the –N⁻ group is a stronger perturber than –NH, the LUMO splitting should be the largest in the dianion, and the smallest in the doubly protonated chromophores. And for

corrphycene additional effect is also observed due to the nonplanarity (see below), whereas for hemiporphycene this effect is not important.

It has been established that the neutral form of hemiporphycene consists of two *trans* tautomers (**1a** and **1b** in Chart 4.3), of which the former is more stable by about 1 kcal/mol.[46-47]
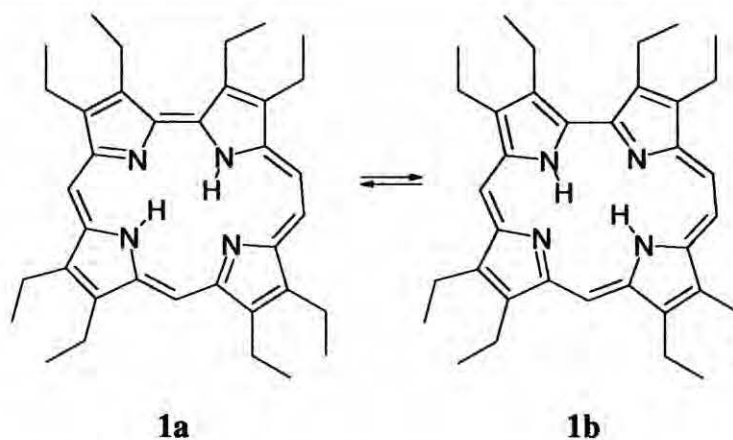
Chart 4.3. Two different trans tautomers of hemiporphycene.

The electronic spectra of the two tautomers are very similar: in a polar solvent, the spectra overlap to such a degree that it is not possible to distinguish features due to a particular form. The same is true for MCD spectra, which confirms that the orbital splitting pattern should be qualitatively the same for both forms, with only minor differences in the orbital splitting values. Actually, for a case of tautomeric equilibrium occurring in a soft chromophore, the situation would have been much different: different signs of ΔHOMO - ΔLUMO and thus, different MCD signs could be expected for different tautomers, as has been discussed for porphyrin and its derivatives.[48]

The orbital splittings have been calculated previously using the PPP method.[42] The present results are qualitatively the same and quantitatively not much different. The values of ΔHOMO computed using B3LYP/6-31G** for the hemiporphycene are 0.08, 0.04, 0.11, and 0.32 eV for the dication, tautomer **1a**, tautomer **1b**, and the dianion, respectively. The

corresponding ΔLUMO values are 0.39, 0.57, 0.57, and 0.66 eV. The inequality ΔHOMO < ΔLUMO is obtained no matter which theoretical method is used. This implicates that even a simple theoretical analysis may be safe and fruitful in predicting the "hard" character of a chromophore.

Naturally, for "soft" or nearly "soft" chromophores, the situation is more complicated, and the exact determination of the sign of ΔHOMO < ΔLUMO may require more sophisticated approaches. Using B3LYP/6-31G** calculations for the non-alkylated species, we obtained 0.03 and 0.07 eV for the values of ΔHOMO and ΔLUMO, respectively, in the neutral form of corrphycene. The corresponding values for the dianion are 0.07 and 0.05 eV. For the dication, two different ground state structures, with energies separated by 3.99 kcal/mol, were obtained (see Figure 4.11).

a   b

Figure 4.11. The structures of two doubly protonated forms of corrphycene, calculated by B3LYP/6-31**. The lower energy was obtained for the form (a).

Both forms are not flat, and differ by the amount of nonplanarity and by the manner the inner protons are tilted out of the molecular plane. The calculations gave 0.06 and 0.07 eV for the HOMO and LUMO splittings in the lower energy form (a), and 0.01 and 0.04 eV for the splittings in the other structure (b).

The above orbital splitting values were obtained for parent, unsubstituted molecules. As can be concluded from the inspection of the shape of molecular orbitals of the parent perimeter (Figures 4.9-4.10), substitution by eight alkyl groups should not have much influence on the splitting pattern. We checked this prediction by comparing the results of AM1 and PM3 calculations performed for both the unsubstituted and octamethyl-substituted species. Qualitatively similar results were obtained in both cases.

Having established the negative-hard character of the hemiporphycene chromophore ($\beta < 0$), we now can make predictions regarding signs and intensities in absorption and MCD spectra. For the Q-bands region, this is easy. The expected -, + sequence of the signs of B terms for the L_1 and L_2 transitions is beyond any doubt, since the μ^+ contributions dominate (cf. Eq. 1.59). The theory predicts that MCD intensities should be strongest for the dianionic forms, which correspond to the largest perturbation of the parent perimeter. Moreover, due to the nature of L-B magnetic mixing, the absolute values of $B(L_2)$ should be larger than those of $B(L_1)$. All these predictions are confirmed experimentally (Figures 4.1-4.3).

In the region of the Soret bands (B states), the analysis is more challenging. Now, the μ^+ contributions will be dominant only for sufficiently strong perturbation (Eq. 1.60). We already noted that the borderline was observed in porphycene and that the inequality ΔHOMO $< \Delta$LUMO is much stronger for the latter than for hemiporphycene. We may thus expect that the perturbation of the perimeter occurring upon formation of hemiporphycene is not strong enough to make the μ^+ term dominant in the formulas for $B(B)$. Therefore, a +, - sequence is predicted for $B(B_1)$ and $B(B_2)$. Figures 4.1-4.3 show that such behavior is indeed observed. The theory also predicts that, as a consequence of L-B magnetic mixing, the magnitude of the B term for B_1 should be smaller than for B_2. This is clearly observed for the dianionic form; in the neutral and protonated species, some cancellation of the MCD intensity in the region of B_2 occurs, due to overlap with another close-lying higher energy transition.

The perimeter model also allows predictions regarding intensities of the individual bands in the absorption spectra. In the case of strongly overlapping L_1-L_2 and B_1-B_2 pairs of transitions, it is difficult to evaluate intensities for individual components. Instead, it is better to use the sums of dipole strengths for L and B bands. The intensity ratio $D(L)/D(B) = [D(L_1)+D(L_2)]/[D(B_1)+D(B_2)]$ should increase with growing strength of the perturbation. Indeed, the experimentally observed ratio is largest for the dianionic form, smaller for the neutral form, and the smallest in the dication (although, due to the presence of an additional band in the Soret region, this trend can only be expressed qualitatively). Equation 1.61[6] relates the intensity ratio to the values of orbital splittings,. Inserting the B3LYP/6-31G** calculated values of orbital splittings into this formula leads to the prediction of the increase of the $D(L)/D(B)$ ratio in the order: dication, neutral forms, dianion, exactly as observed.

For the case of nearly equal ΔHOMO and ΔLUMO values, correct reproduction of the MCD signs is not an easy task, as illustrated in Figures 4.4-4.6, which show the results of INDO/S calculations. For the neutral corrphycene, the results are correct for all four perimeter excited states, and also for an additional nearby higher energy transition. However, the signs are not correctly predicted for the L transitions in the dianion. For the dication, the situation is even worse, which may be due to the presence of two nonplanar structures and possible solute-solvent interactions leading to changes in geometry and location of excited states. Actually, we note that the MCD intensity for the dication is stronger than in the neutral molecule, and similar to that in the anion. This seems a little unexpected, given that the -NH groups are weaker perturbers than the -N⁻ bridges. However, the nonplanarity may enhance the effect of perturbation and make the dication a "harder" chromophore. Actually, the MCD results combined with the ΔHOMO and ΔLUMO values obtained for the two forms of the dication favor the structure (b) of Figure 4.11.

The above results demonstrate the usefulness and reliability of a simple perimeter model when predicting the absorption and MCD spectral patterns. One can expect that the correctness of this approach will depend on how well an excited state can be defined in terms of four configurations only. In particular, the validity of this model could be put in doubt with regard to the Soret transitions, since the experiment shows a presence of at least one nearby electronic state. A good measure of the accuracy of description of a given state by a perimeter model (or, for that matter, by a closely-related four orbital model of Gouterman[49]) is provided by the value of the sum of squares of the four CI coefficients that describe the four configurations of the perimeter model. The recently computed values of this parameter that were performed in series of calculations that used various sizes of CI bases for porphyrin,[50] porphycene,[50] dibenzoporphycene[50] and smaragdyrins (the results presented in part 4.1.2), show that the better the description by the four-orbital model is, the closer the value will approach unity for a given electronic state.

The INDO/S calculated values for two tautomers of **1**, for **2**, and for its charged forms are shown in Tables 4.9-4.10.

Table 4.9. Values of the sums of squares of the four CI coefficients, calculated for two tautomers of hemiporphycene, describing the contributions from single excitations considered in four-orbital model. The INDO/S calculations involved a 14x14 CI basis set.

	1a	1b	Dication	Dianion
L_1	15.4 (0.03)/0.96	13.4 (0.04)/0.95	13.6 (0.06)/0.97	15.2 (0.20)/0.93
L_2	16.3 (0.15)/0.97	16.0 (0.07)/0.98	15.2 (0.00)/0.97	18.6 (0.05)/0.95
B_1	27.9 (1.49)/0.55	26.0 (0.77)/0.38	26.3 (2.35)/0.70	23.6 (1.08)/0.92
B_2	27.8 (1.68)/0.79	26.4 (1.64)/0.73	26.8 (2.21)/0.75	24.6 (0.81)/0.87

Table 4.10. Values of the sums of squares of the four CI coefficients, calculated for corrphycene describing the contributions from single excitations considered in the four-orbital model. The INDO/S calculations involved a 14x14 CI basis set.

	Neutral form	Dication	Dianion
L_1	15.4 (0.005)/0.95	13.9 (0.041)/0.96	15.7 (0.009)/0.97
L_2	16.5 (0.009)/0.98	15.0 (0.001)/0.95	20.9 (0.050)/0.97
B_1	26.2 (1.920)/0.75	26.4 (2.520)/0.92	23.9 (2.130)/0.87
B_2	27.4 (1.450)/0.51	26.7 (2.820)/0.85	24.5 (0.400)/0.83

It can be seen that the L states are always described perfectly in terms of the four orbital model. For the Soret transitions, the model works well for charged species, while in neutral forms one of the states is mixed with other electronic transitions. Similar situation was encountered using the same computational approach for parent porphyrin.[50]

The values of transition energies and oscillator strengths, calculated using TD-DFT for the unsubstituted parent hemiporphycene and corrphycene, are shown in Tables 4.1-4.8 compared with the experimental results obtained for the alkylated molecule. The experimental and calculated values are in quite good agreement. The calculations overestimate the transition energies by 0.1 – 0.4 eV, a result similar to those obtained for free base and metalloporphyrin derivatives using TD-DFT and various *ab initio* schemes.[51] In fact, the agreement would have been much better if the alkyl substituents were included in the calculations. For magnesium porphyrin, it has been reported that the TD-DFT calculated values for tetramethyl-tetraethyl-substituted molecule are lower by 0.2-0.3 eV than the values obtained for the unsubstituted compound.[52] Much better agreement is obtained for the splitting between L and B pairs. Moreover, the calculations correctly predict that for the neutral species of hemiporphycene the lowest excited singlet state of tautomer **1a** lies higher than in form **1b**, and that for the second excited state this ordering is reversed.

4.2. Isomers of smaragdyrin

In this part, the results of spectral, photophysical and theoretical studies are presented for alkyl derivatives of two porphyrinoids, **3** (isosmaragdyrin) and **4** (monooxoisosmaragdyrin), isomers of smaragdyrin (Chart 4.4). Since the neutral forms turned out to be unstable, all of the results refer to singly protonated species.
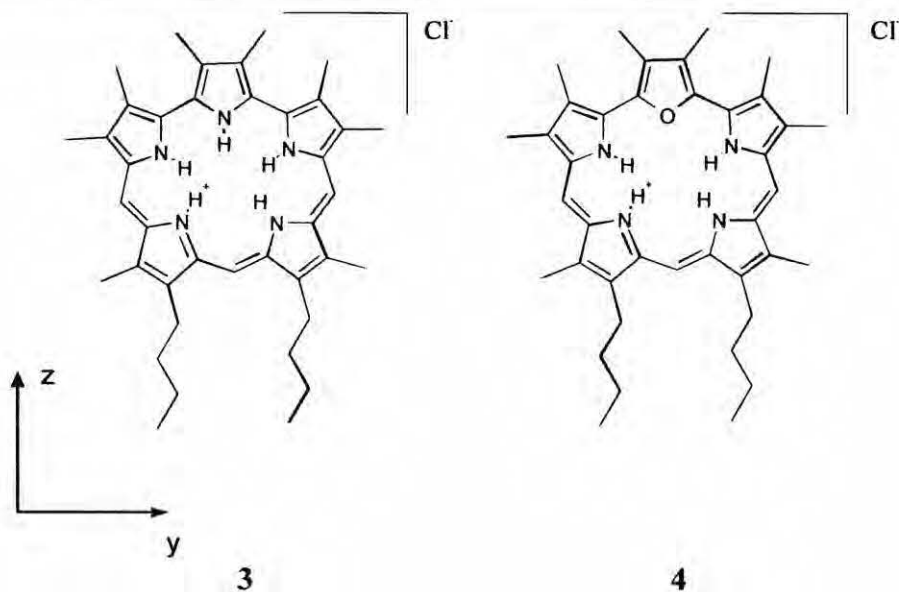
Chart 4.4.   Isosmaragdyrin **3** (left) and monooxoisosmaragdyrin **4**

The aim of the spectral work was to determine the electronic structure of the two compounds, to assign the lowest electronic transitions and to relate them to those of porphyrin on the basis of both experiment and calculations. The photophysical studies were focused on the efficiencies of fluorescence and triplet formation, both parameters being crucial for possible applications in photodynamic therapy. The investigation led to the location and assignment of a large number of electronic transitions. In particular, strong electronic transitions were observed in the vicinity of the Soret bands, their origin being described by orbitals other than the ones used in the Gouterman model.[4, 49] Nevertheless, the four orbital model proved to work extremely well in the description of the four lowest

electronic states.

Absorption spectra of **3** and **4** at 77 K are shown in Figures 4.12 and 4.13, while those taken at room temperature are presented in Figures 4.14 and 4.15.
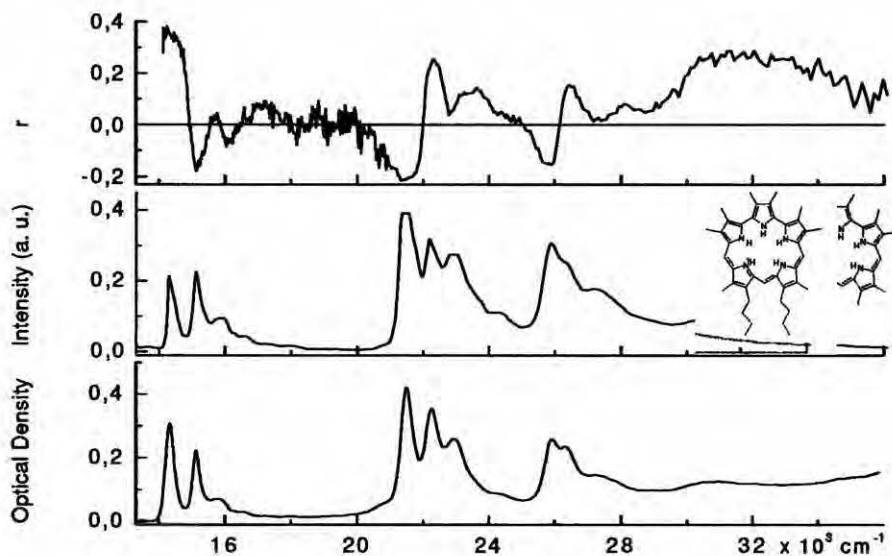
Figure 4.12. Bottom, absorption; middle, fluorescence excitation (monitored at 14 300 cm^{-1}); top, anisotropy of fluorescence excitation of **3**. The spectra were measured at 77 K in EPA glass (ethyl ether: isopentane:ethanol 5:5:2).
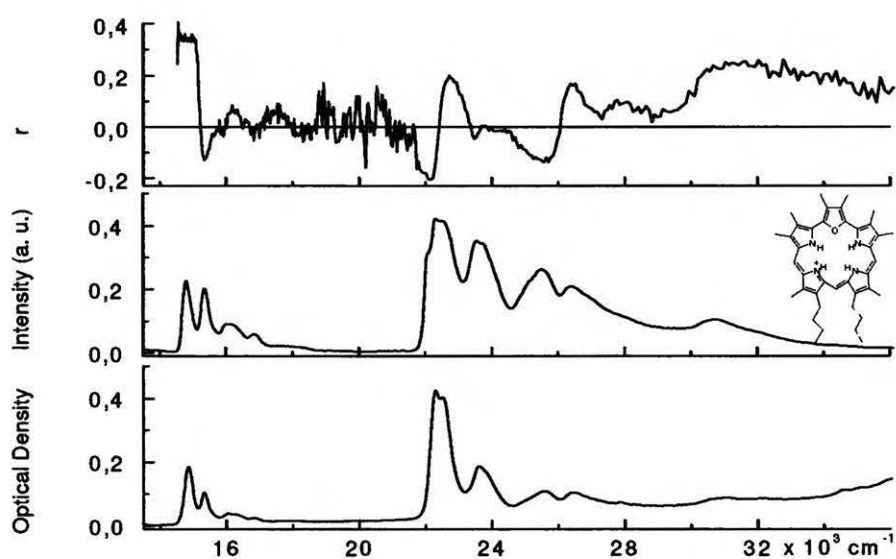
Figure 4.13. Bottom, absorption; middle, fluorescence excitation (monitored at 14 700 cm^{-1}); top, anisotropy of fluorescence excitation of **4** at 77 K in EPA glass.
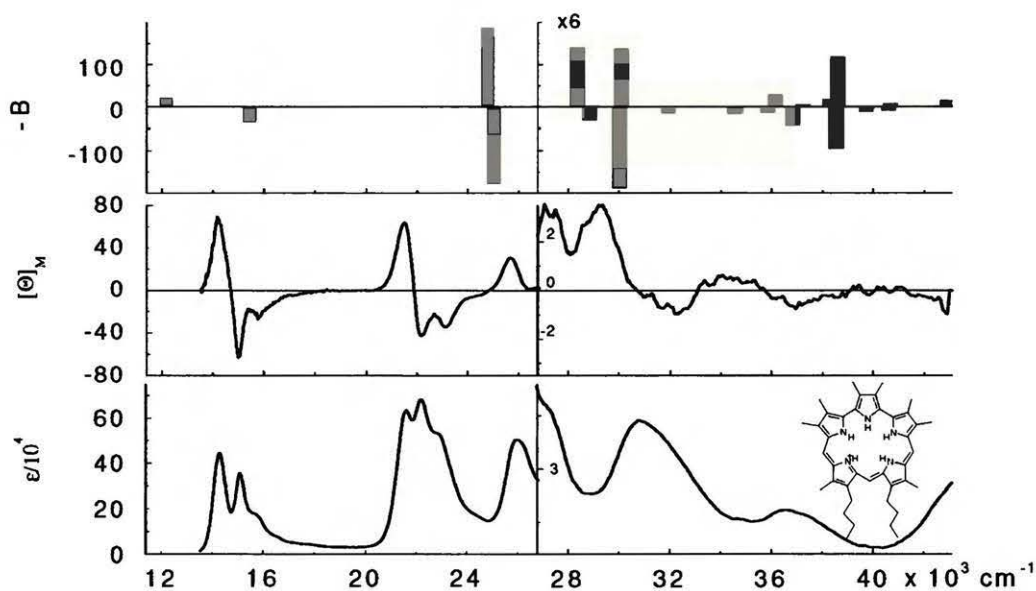
Figure 4.14. Bottom, absorption; middle, MCD spectrum of **3** in acetonitrile at 293 K. Top, INDO/S calculated values of transition energies and B terms (D$^2\mu_B$/cm^{-1}).
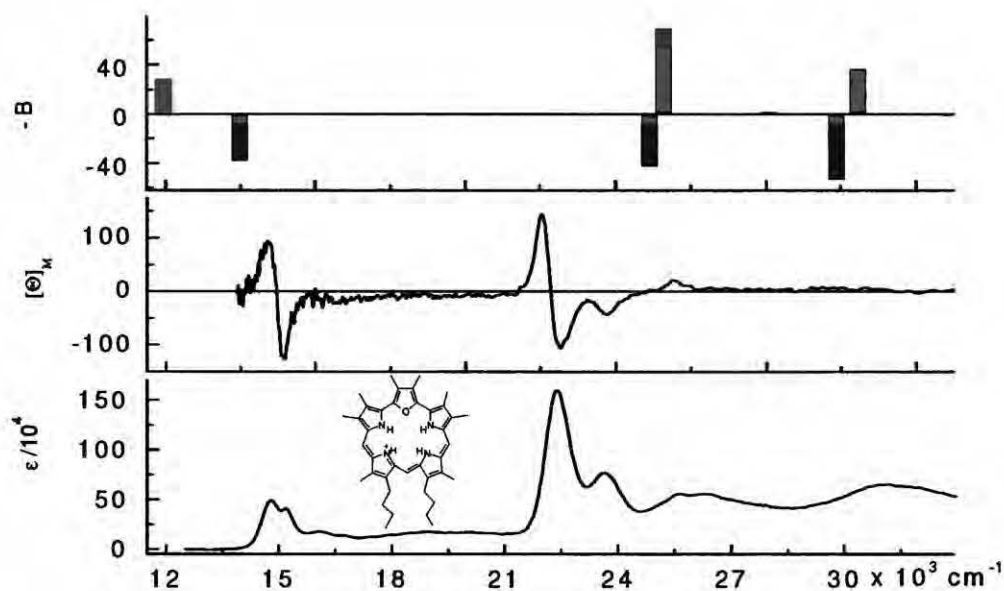
Figure 4.15. Bottom, absorption; middle, MCD spectrum of **4** in acetonitrile at 293 K. Top, INDO/S calculated values of transition energies and B terms $(D^2\mu_B/cm^{-1})$.

The spectral pattern is rich and quite different from that characteristic of porphyrin derivatives. Low-energy bands are located around 14-16 000 cm^{-1}, separated by about 7000 cm^{-1} from the onset of stronger transitions at higher energies. These two band systems may be considered analogs of Q and Soret transitions. However, unlike in porphyrins, the two band systems have comparable intensities, in particular in **3**. Several additional electronic transitions are observed above 26 000 cm^{-1}, again with intensities not much different from those of the strongest band system. This behavior is very different from that of porphyrins[45, 53], in which the Soret bands intensity is much larger than that of all other electronic transitions.

The analysis of the absorption spectra with the help of polarized spectroscopy techniques (emission anisotropy and magnetic circular dichroism) reveals that each of the

lowest three band systems in both compounds is composed of two close-lying electronic transitions, with origins separated by less than 1000 cm^{-1}. The two components of each pair have different polarizations, as evidenced by the shape of the anisotropy of fluorescence excitation curves for both compounds (Figures 4.12 and 4.13). Different polarizations make it possible to separate the vibronic components of each transition. In all the lowest transistions, vibronic activity of a mode having a frequency of 1300-1600 cm^{-1} is observed for both compounds (Table 4.11 and 4.12).

Table 4.11. Electronic transition energies of **3**, along with the corresponding values of fluorescence anisotropy (r), orientation factors (K_i) and Faraday B terms.

	E [10^3 cm^{-1}]	r	K_i [a]	B [b]
1	14.3	0.36	0.44	-82
	15.8			
	17.3			
2	15.1	-0.18	0.35	99
	15.9			
	16.6			
	18.0			
3	21.5	-0.21	0.35	-55
	23.0			
	24.4			
4	22.2	0.25	0.44	74
	23.6			
5	25.9	-0.16	0.35	-26
	27.4			
6	26.5	0.15	0.44	
	28.1			
7	29.3	0.10		
8	30.6	0.25		
9	32.3	0.23		
10	34.1	0.24		
11	36.6	0.07		

[a] accuracy: ±0.05; [b] units of D$^2\mu_B$/cm^{-1}.

Table 4.12. Electronic transition energies of **4**, along with the corresponding values of fluorescence anisotropy (r) and Faraday B terms.

	E $[10^3 \text{ cm}^{-1}]$	r	B^a
1	14.8	0.36	-68
	16.2		
	17.6		
2	15.3	-0.13	73
	16.8		
	18.3		
3	22.1	-0.20	-65
	23.8		
4	22.5	0.20	111
	23.6		
5	25.6	-0.14	-26
	27.3		
6	26.4	0.17	
	27.8		
7	30.7	0.24	

^{a}units of $D^2\mu_B/\text{cm}^{-1}$.

The moments of the second, third and fifth transitions are practically orthogonal to the moment of the S_0-S_1 transition, as evidenced by the fluorescence anisotropy values, close or equal to -0.2. On the contrary, a small value is obtained for the angle between the S_0-S_1 transition moment and the moments of the fourth and the sixth transitions. The observed positive values must be treated as lower limits, due to overlap with differently polarized close-lying transitions. These findings suggest an approximate C_{2v} symmetry of the chromophores. Indeed, the X-ray data of both **3** and **4** show nearly planar structures, with only the middle pyrrole ring of the terpyrrole moiety tilted out of the plane formed by the four other rings by 23.2^0 in **3** and 21.2^0 in **4**.[17]

The locations of electronic transitions were independently confirmed by MCD experiments (Figures 4.14 and 4.15). The maxima and minima on the fluorescence excitation

anisotropy curves coincide with the minima and maxima in the MCD spectra. The -, +, -, +, - sequence of the signs of the Faraday B terms is obtained for the lowest four transitions in both compounds. Overall, the combination of MCD and fluorescence anisotropy makes it possible to identify eleven electronic transitions for **3** and seven for **4** (the lower number in the case of **4** is due to a weaker MCD signal in the region above 28 000 cm^{-1}, most probably caused by the overlap of positive and negative bands belonging to different electronic states). The transition energies, B terms, and the values of fluorescence anisotropies are given in Tables 4.11 and 4.12. For **3**, these Table 4.11 also contains the values of orientation factors, K_i, obtained from the LD spectra.

The K values were extracted from the LD spectra using the TEM procedure.[1] The LD spectra and the application of the TEM procedure are shown in Figures 4.16 and 4.17.
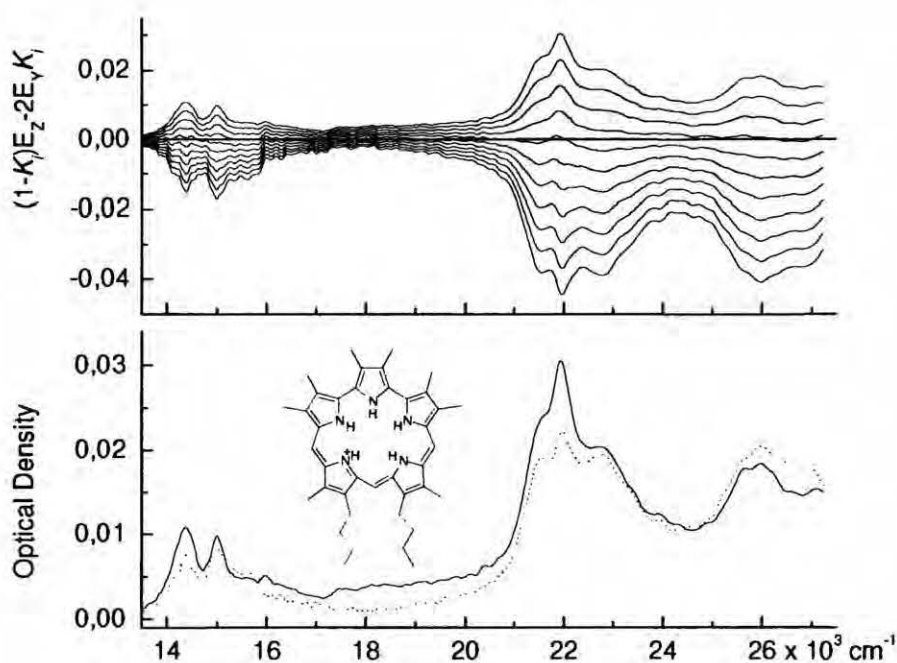
Figure 4.16. LD spectra of **3** (bottom) measured in a stretched polyethylene sheet at room temperature and the stepwise reduction procedure (top).
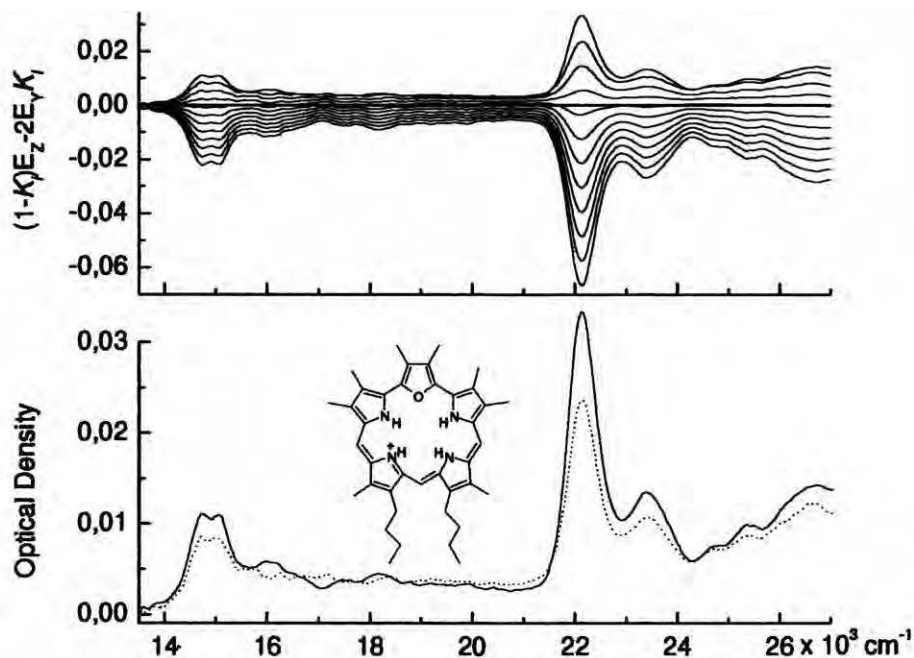
Figure 4.17. LD spectra of **4** (bottom) measured in a stretched polyethylene sheet at room temperature and the stepwise reduction procedure (top).

The spectra are quite noisy, due to very low solubility of both compounds in PE. The K values change in a rather narrow range. However, joint analysis of the LD and anisotropy measurements can be quite instructive. The first, fourth and sixth electronic transitions in **3**, have $K_i = 0.44$, while for the other three (second, third and fifth transitions) $K_i = 0.35$. This result is in perfect agreement with the fluorescence anisotropy data that show different polarizations in the two groups. Thus, the transitions with a larger K_i value are better aligned with the "effective orientation axis" - a direction which, on the average, aligns the best. It is natural to identify the effective orientation axis with the long molecular direction z (vertical direction in the Chart 4.4). This implies, given an approximate C_{2v} symmetry of the chromophore, that the first, fourth and sixth electronic transitions in **3** are polarized along the z axis, while the moments of the second, third and fifth transitions coincide with the in-plane y axis, perpendicular to z.

For **4**, the reliable separation of the orientation factors of the components of each pair was not possible, due to the combination of low solubility in PE and the fact that the pairs of transitions 1-2, 3-4 and 5-6 lie even closer to each other than in **3**. Interestingly, however, qualitative use of the reduction procedure for **4** yields an important result: for the two components of the Soret region the ordering of polarizations is opposite than in **3** (the first peak at 22 500 cm^{-1} has a larger K_i value than the peaks corresponding to the higher-lying component of the pair). Thus, the ordering of the two Soret transitions is reversed in **4** with respect to **3**. This is consistent with the shapes of the absorption spectra in this region. The transition with larger oscillator strength corresponds to the higher-energy state in **3**, and to the lower-energy state in **4**. In the latter molecule, since the two transitions are nearly degenerate, their overlap produces only one broad absorption band at room temperature; the two components become distinguishable only at lower temperatures (*cf.* Figures 4.13 and 4.15). This finding also explains why the extinction coefficient of the strongest absorption band is much larger in **4** than in **3**: in the former, it corresponds to a sum of two transitions. In addition, the oscillator strength of the strongest transition in **4** may be larger than in **3**, as predicted by calculations (Tables 4.13 and 4.14).

Table 4.13. Transition energies, oscillator strengths (f), polarizations, and Faraday *B* terms for the excited singlet states of **3**. Dominant configurations are shown using the convention of numbering the occupied orbitals as 1, 2... downwards from the HOMO, and the unoccupied ones as -1,-2... upwards from the LUMO. α_{zy} and α_{zx} are the angles between the transition moment and the *z* axis in the *zy* and *zx* planes, respectively (see Chart 4.4).

state	E $[10^3\,cm^{-1}]$	f	zy [deg]	zx [deg]	B	Main CI contribution
1	12.2	0.166	89	-2	-20.40	0.80 (1 -1), 0.56 (2 -2)
2	15.4	0.145	-2	-4	35.14	0.81 (2 -1), 0.50 (1 -2)
3	24.8	2.827	1.7	5	-183.41	0.84 (1 -2), 0.48 (2 -1)
4	25.0	2.737	-88	1	172.58	0.80 (2 -2), 0.56 (1 -1)
5	28.4	0.028	88	-1	-23.95	0.69 (1 -4), 0.66 (2 -3)
6	28.8	0.037	-3	8	5.36	0.61 (1 -3), 0.54 (2 -4)
7	30.0	0.178	89	0	30.78	0.77 (4 -1), 0.45 (3 -2)
8	30.1	0.003	48	-40	-22.19	0.77 (3 -1)
9	31.9	0.053	-4	-14	2.42	0.85 (6 -1)
10	32.2	0.001	-28	12	0.17	0.47 (7 -1), 0.42 (5 -1)
12	32.8	0.020	-89	2	-0.07	0.47 (2 -3), 0.44 (5 -1)
13	33.7	0.080	90	-8	1.94	0.69 (7 -1), 0.35 (2 -3)
17	36.8	0.059	88	6	7.61	0.58 (3 -2), 0.46 (4 -1)
18	37.2	0.091	-1	-20	-1.26	0.65 (1 -6), 0.36 (5 -2)
22	39.7	0.120	-39	24	1.17	0.42 (4 -2), 0.35 (8 -2)
23	39.7	0.093	27	24	1.24	0.48 (4 -2), 0.38 (2 -5)
24	40.6	0.037	-1	32	1.40	0.45 (1 -1), 0.38 (5 -2)
26	41.6	0.093	1	16	0.01	0.57 (9 -2), 0.30 (1 -6)
27	42.9	0.073	-89	-3	-2.62	0.54 (2 -8), 0.33 (6 -2)
28	43.4	0.019	-89	2	5.90	0.70 (1 -6), 0.35 (2 -6)
29	43.6	0.035	0	22	0.62	0.55 (1 -10), 0.40 (2 -7)
30	43.9	0.066	0	-14	-4.19	0.55 (2 -7), 0.46 (1 -8)

Table 4.14. Transition energies, oscillator strengths (f), polarizations, and Faraday B terms for the excited singlet states of **4**. See caption to Table 4.13 for details.

state	E $[10^3 \text{ cm}^{-1}]$	f	zy [deg]	zx [deg]	B	Main CI contribution
1	11.9	0.102	83	0	-28.19	0.75 (1 -1), 0.58 (2 -2)
2	14.0	0.086	-3	-4	37.80	0.77 (2 -1), 0.55 (1 -2)
3	24.9	2.960	-83	2	45.23	0.69 (2 -2), 0.54 (1 -1)
4	25.3	3.487	7	5	-72.55	0.71 (1 -2), 0.48 (2 -1)
5	27.7	0.000	56	-8	0.54	0.65 (2 -3), 0.57 (1 -4)
6	28.1	0.003	60	0	-1.30	0.60 (1 -3), 0.54 (2 -4)
7	29.9	0.264	-88	0	53.26	0.75 (4 -1), 0.46 (3 -2)
8	30.5	0.057	-1	-1	37.06	0.77 (3 -1)
9	31.9	0.007	10	-19	0.26	0.72 (5 -1)
10	32.6	0.011	15	-9	0.35	0.75 (6 -1)
11	32.9	0.015	2	10	0.89	0.40 (2 -4), 0.38 (7 -1)
12	33.7	0.018	-73	-3	0.24	0.44 (5 -1), 0.43 (2 -4)
13	34.1	0.018	-49	47	0.85	0.52 (7 -1), 0.36 (2 -3)
16	36.8	0.025	-69	-12	3.37	0.44 (4 -1), 0.40 (3 -2)
19	38.4	0.063	-85	-2	-3.43	0.63 (1 -5), 0.43 (6 -2)
20	38.6	0.054	82	7	-3.01	0.58 (7 -2), 0.39 (2 -6)
21	39.0	0.129	-3	-27	10.39	0.60 (4 -2), 0.47 (2 -5)
22	39.5	0.058	-3	16	-2.99	0.43 (8 -2), 0.39 (1 -6)
27	42.7	0.045	-72	2	4.10	0.77 (1 -7)
28	43.0	0.055	-68	5	-7.58	0.65 (2 -8)
29	43.7	0.088	52	3	3.35	0.68 (2 -7)

The results of calculations of transition energies, oscillator strengths, polarizations and Faraday B terms are presented in Tables 4.13 and 4.14. The assignment of the experimentally observed transitions to the calculated ones is obvious for the lowest two pairs, 1-2 and 3-4, although the energy ordering in the pairs is not always correct. This is not surprising, since the experimentally observed spacings between S_1-S_2 and S_3-S_4 transitions are less than 1000 cm^{-1}, while the accuracy of the INDO/S method is about 2000-3000 cm^{-1}. The leading configurations correspond to those predicted by the Gouterman's four-orbital model. A quantitative measure of how well a given state is described by this model is given by the sum of four CI coefficients corresponding to the electronic excitations from the two highest occupied molecular π orbitals to the two lowest unoccupied ones:

$$r = \sum_{ij=1,2} C_{ij}^2 \tag{4.1}$$

Values of r close to one indicate a validity of the approach based on a simple 2x2 MO basis. The calculated values of r for **3** and **4** are given in Table 4.15.

Table 4.15. The calculated values of the coefficient r for the lowest excited states of **3** and **4** (see text for details). For comparison, data obtained for the *trans* and *cis* tautomeric forms of parent porphyrin[50] are also shown.

	porphyrin		3	4
	trans	*cis*		
1	0.96	0.96	0.96	0.96
2	0.98	0.97	0.95	0.95
3	0.71	0.57	0.93	0.96
4	0.94	0.61	0.96	0.93
5			0.02	0.05
6			0.03	0.02

It is seen that the four orbital model works exceptionally well for both Q and Soret transitions in the two compounds. The r values are about the same as in parent porphyrin,[50] or even higher in the case of one of the Soret transitions. Thus, for the S_1-S_4 states the four

configurations of the Gouterman model mix very little with other ones. This is clearly seen in Figures 4.18-4.19 and Tables 4.16-4.17, in which we compare transition energies and oscillator strengths calculated using various CI bases.
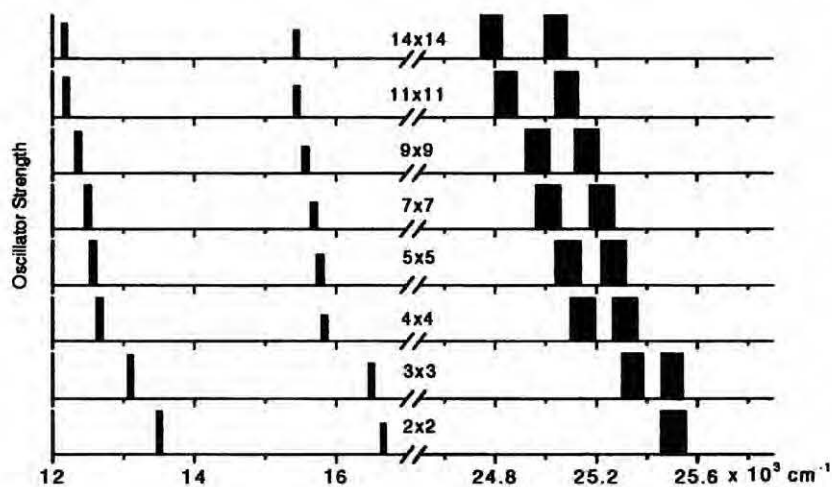
Figure 4.18. Calculated energies and intensities of the four lowest excited singlet states of 3 as a function of the of the CI basis size. See also Table 4.16.
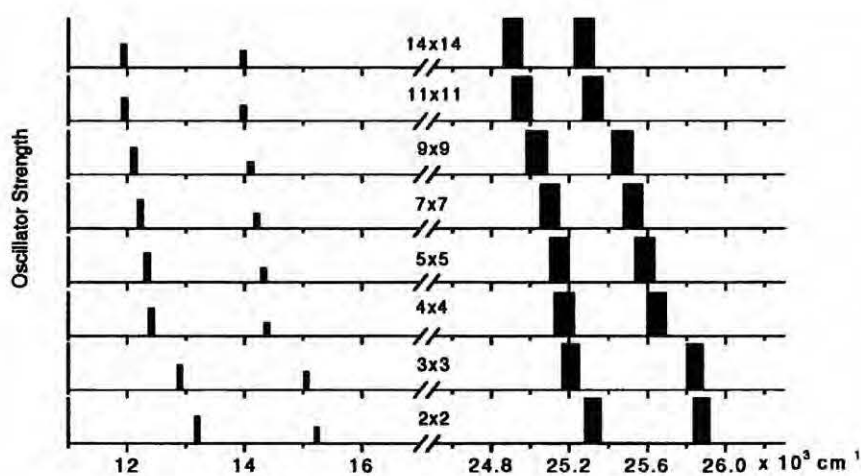
Figure 4.19. Calculated energies and intensities of the four lowest excited singlet states of 4 as a function of the of the CI basis size. See also Table 4.17.

Table 4.16. Transition energies, oscillator strengths, and MCD B terms calculated for 3 using various sizes of the CI basis set.

Basis	E [10^3 cm^{-1}]	F	B
2x2	13.5	0.219	-22.9
	16.7	0.156	39.3
	25.5	2.811	-[a]
	25.5	2.837	2560.2
3x3	13.1	0.186	-21.6
	16.5	0.162	36.4
	25.3	2.825	-341.2
	25.5	2.989	329.11
4x4	12.7	0.182	-21.3
	15.8	0.135	35.8
	25.1	3.068	-299.2
	25.3	2.883	292.4
5x5	12.6	0.187	-22.3
	15.8	0.144	37.2
	25.1	3.051	-287.1
	25.3	2.869	281.2
7x7	12.5	0.178	-21.2
	15.7	0.139	35.8
	25.0	2.934	-231.2
	25.2	2.841	222.0
9x9	12.4	0.171	-20.8
	15.6	0.138	35.2
	25.0	2.904	-260.9
	25.2	2.797	253.0
11x11	12.2	0.167	-20.7
	15.5	0.145	35.5
	24.8	2.851	-203.1
	25.1	2.765	192.1
14x14	12.2	0.166	-20.4
	15.4	0.145	35.0
	24.8	2.827	-186.4
	25.0	2.736	175.3

[a] unrealistically large value calculated due to accidental degeneracy

Table 4.17. Transition energies, oscillator strengths, and MCD B terms calculated for **4** using various sizes of the CI basis set.

Basis	$E\ [10^3\ cm^{-1}]$	f	B
2x2	13.2	0.122	-29.3
	15.2	0.093	39.0
	25.3	3.063	-61.9
	25.9	3.691	52.0
3x3	12.9	0.110	-27.7
	15.1	0.096	36.9
	25.2	3.141	-31.3
	25.8	3.705	21.4
4x4	12.4	0.112	-29.5
	14.4	0.082	38.6
	25.2	3.097	6.3
	25.6	3.748	-21.2
5x5	12.3	0.112	-29.8
	14.3	0.084	39.2
	25.2	3.111	12.4
	25.6	3.710	-29.0
7x7	12.3	0.111	-29.8
	14.3	0.085	39.3
	25.1	3.063	20.0
	25.6	3.641	-40.1
9x9	12.1	0.108	-29.0
	14.1	0.082	38.3
	25.0	3.039	22.4
	25.5	3.583	-45.4
11x11	12.0	0.103	-28.6
	14.0	0.086	38.2
	25.0	2.987	46.1
	25.3	3.505	-74.0
14x14	11.9	0.102	-28.2
	14.0	0.086	37.8
	24.9	2.960	41.7
	25.3	3.487	-69.1

The energy and intensity changes between a minimum 2x2 model and the calculation involving 196 (14x14) singly excited configurations are indeed very small. The reason why the lowest four electronic states are so well described even by a 2x2 basis is due to the pattern of MO energies. Two highest occupied orbitals are well-separated in energy, by about 2 eV, from the third and lower ones. The energy splitting between the second and third unoccupied orbital is also quite high, about 1.5 eV. This situation is analogous to that found for porphyrin and porphycene, but very different from the orbital energy pattern in another extended porphyrin, rosarin,[54] where the second and third highest occupied orbitals, as well as the second and third lowest unoccupied ones were found to lie close in energy (for a high-symmetry parent rosarin chromophore they are exactly degenerate).

An important quantity resulting from calculations is the value of the energy splitting between the two highest occupied π orbitals (ΔHOMO) and the splitting between the two lowest occupied π orbitals (ΔLUMO). The difference ΔHOMO - ΔLUMO is crucial for the sign of the MCD in the region of the lowest four electronic transitions that can be described by the perimeter model. The calculations predict that ΔHOMO $\ll$ ΔLUMO, which corresponds to a negative-hard chromophore. For such a case, and for large values of D(L)/D(B), the ratio of dipole strengths of Q and Soret transitions, a +, -, +, - sequence of B terms is expected, exactly as observed. The origins for the hard character of the **3** and **4** chromophores are easy to understand by inspecting the shape of the molecular orbitals of the parent perimeter. Isosmaragdyrin as well as monooxoisosmaragdyrin can formally be derived from a [23]annulene cation, $C_{23}H_{23}^+$ perimeter containing 4N+2=22 π-electrons. These structures are obtained from an unperturbed perimeter by bridging with five -NH- groups or with four -NH- groups and one -O$^-$ group for **3** and **4**, respectively (Figure 4.20).
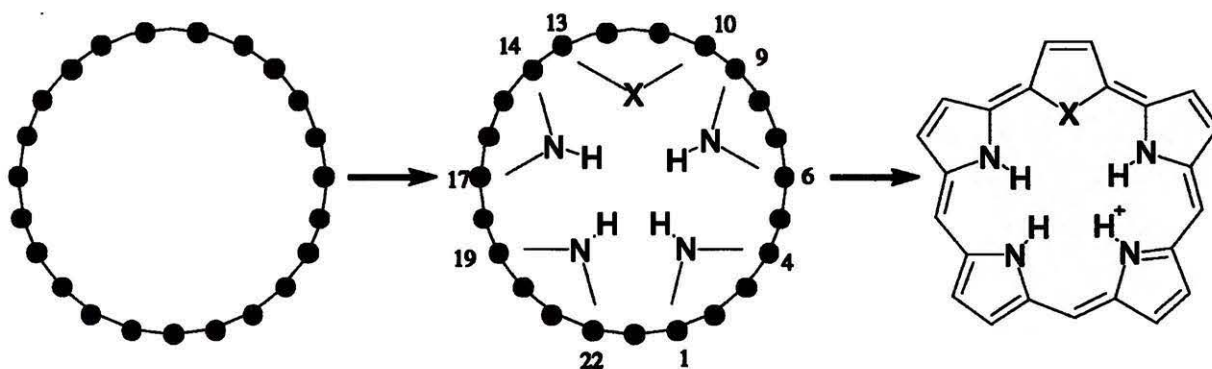
Figure 4.20. Formal derivation of isosmaragdyrin X=-NH- or monooxoisosmaragdyrin X=-O⁻, from an 22 π electron perimeter, the [23]annulene cation.

The response of each orbital to structural perturbations that lead to **3** or **4** can be readily predicted. These responses are shown in Figure 4.21.
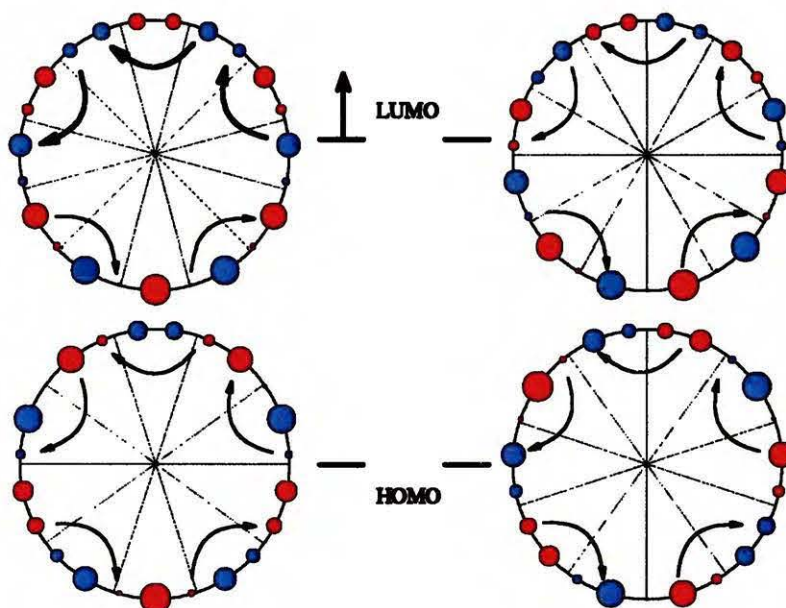
Figure 4.21. The shapes of the HOMO and LUMO orbitals of the parent $C_{23}H_{23}^{+}$ perimeter and the expected energy shifts caused by the perturbations corresponding to the formation of **3** or **4**.

The values of ΔHOMO and ΔLUMO can also be used for estimation of the relative intensities of the Q and Soret transitions. According to the perimeter model, the intensity ratio can be calculated[6] as in Eq. 1.61. For **3**, the calculations yield very small values of ΔHOMO, while ΔLUMO is about 1 eV. We thus obtain D(L)/D(B) $\approx$ 0.19, in a very reasonable agreement with experiment. An important possibility is to compare the experimental D(L)/D(B) intensity ratios in **3** and **4** with those predicted on the basis of orbital energy differences. In **4**, ΔLUMO is calculated to be smaller than in **3**. As a consequence, **4** should reveal a smaller D(L)/D(B) ratio: this is indeed observed (*cf.* Figures 4.14 and 4.15).

Inspection of Tables 4.13 and 4.14 shows that the transition moment directions follow quite well the approximate C_{2v} symmetry of the chromophore. This is in agreement with the results obtained from anisotropy measurements.

All the calculations presented above were performed for a singly-charged chromophore, without taking into account the role of the chloride counterion. In order to investigate the possible influence of the chloride anion on the structure and spectral properties of **3** and **4**, we have made quantum chemical calculations of transition energies, intensities and *B* terms for neutral structures, with the chloride anion located above the center of the molecular plane of the positively charged chromophore. This geometry, optimized by the AM1 method, is in general agreement with the X-ray data.[17] The INDO/S calculations revealed that the introduction of the chloride anion does not have much influence on the calculated spectral pattern.

Photophysics of **3** *and* **4**

Fluorescence spectra of **3** and **4** in a nonpolar, polar aprotic and a protic solvent are shown in Figure 4.22.
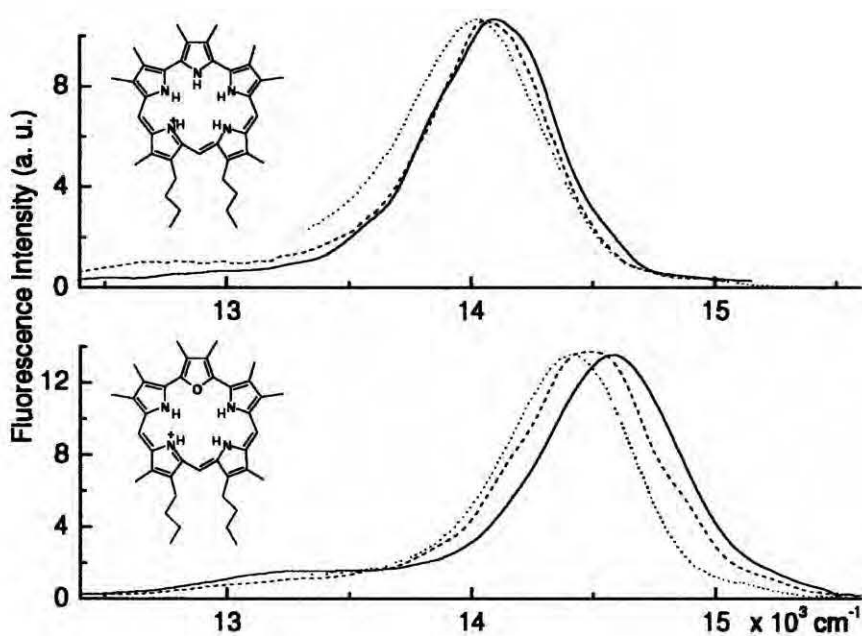
Figure 4.22. Room temperature fluorescence spectra of **3** (top) and **4** (bottom) in different solvents: acetonitrile (solid line), methanol (dashed line) and cyclohexane (dotted line).

The photophysical parameters of **3** and **4** are presented in Table 4.18. These data are for the protonated structures. We have also attempted to characterize neutral forms of **3** and **4**. For this purpose, NaOH or NH_3 were added to solutions of the studied compounds in various solvents. This resulted in a blue shift of fluorescence by 8-10 nm. No appreciable change in intensity could be observed. More comprehensive and precise investigations of the neutral forms turned out to be impossible because these forms are unstable when exposed to light and decay within hours.

Table 4.18. Photophysical parameters of **3** and **4**.

	Solvent	ϕ_f [a]	ϕ_T [b]	τ_f, [c] [ns]	k_r [d] $[10^7 s^{-1}]$	k_{ISC} [e] $[10^8 s^{-1}]$	k_{IC} [f] $[10^8 s^{-1}]$
1	Methanol	0.042	0.40	2.2±0.2	1.9	1.8	2.5
	Acetonitrile			2.5±0.3			
	Cyclohexane			2.8±0.3			
2	Methanol	0.046	0.47	1.4±0.2	3.3	3.4	3.7
	Acetonitrile			2.3±0.2			
	Cyclohexane			3.0±0.2			

[a] fluorescence quantum yield, accuracy: ±20%; [b] triplet formation efficiency, estimated accuracy: ±30%; [c] non-deaerated solutions; after deoxygenation, these values increase by about 10%; [d] the radiative constant of S_1 depopulation; [e] the rate constant of $S_1 \rightarrow T_1$ intersystem crossing; [f] the rate constant of $S_1 \rightarrow S_0$ internal conversion.

Quantum yields of the formation of triplet states (φ_T) for **3** and **4** have been calculated on the basis of transient absorption and bleaching measurements on the nanosecond timescale (Figures 4.23-4.24). Briefly, the value of φ_T is estimated from the ratio of the amplitudes of the slow and fast kinetic signals describing the recovery of the ground state population.[55] The former describes the $T_1 \rightarrow S_0$ intersystem crossing, while the latter, $S_1 \rightarrow S_0$ internal conversion. The measurement is performed at wavelengths where the contribution of transient absorption is negligible. Alternatively, the $S_1 \rightarrow S_n$ and/or $T_1 \rightarrow T_n$ contributions can be substracted from the transient signal. Bottom parts of Figures 4.23 and 4.24 show the kinetic curves of the ground state repopulation, from which the quantum yield of triplet formation could be determined.
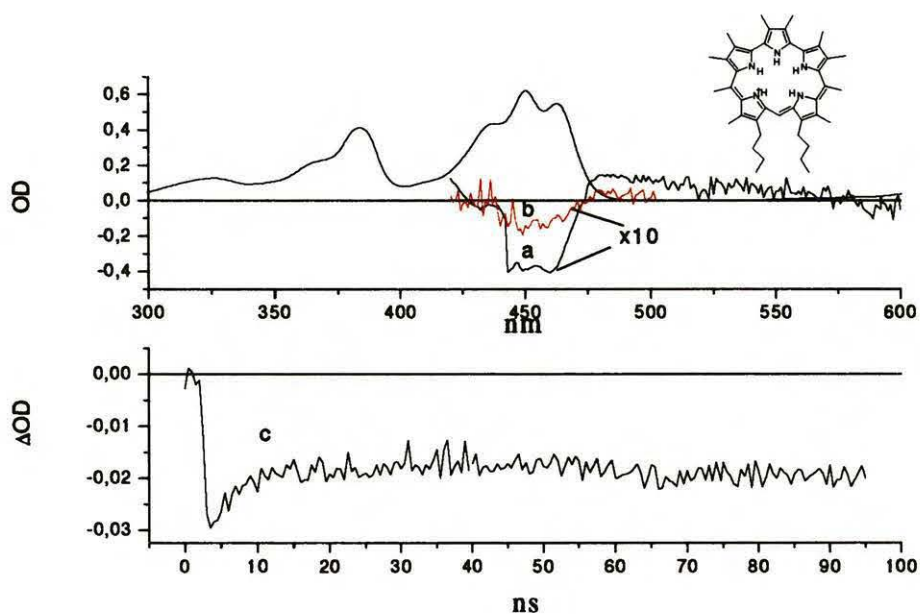
Figure 4.23. Top, stationary absorption and transient curves measured at the moment of excitation (a) and 50 ns after excitation (b). Bottom, kinetic curve of the ground state repopulation of **3**, monitored at 450 nm (c).
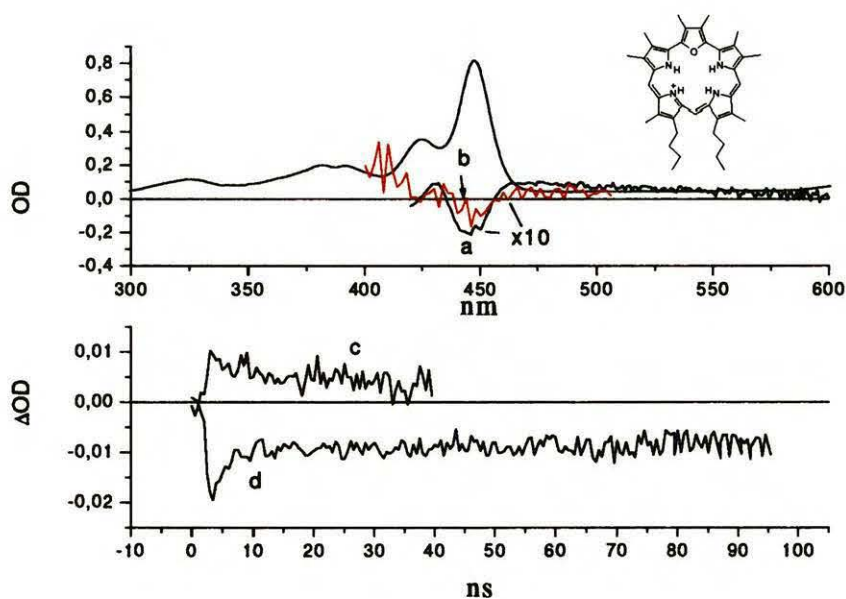
Figure 4.24. Top, stationary absorption and transient curves of **4** measured at the moment of excitation (a) and 40 ns after excitation (b). Bottom, transient signals, monitored at 470 nm (c) and at 440 nm (d).

The photophysical data shown in Table 4.18 indicate a "normal" character of the chromophores. The values of the rate constants for the nonradiative depopulation are typical of aromatic compounds and do not point to considerable structural changes upon excitation. This is in contrast to some other extended porphyrins, such as rosarin, whose nonplanarity and conformational flexibility leads to very efficient $S_1 \rightarrow S_0$ internal conversion process.[54] **3** and **4**, on the other hand, seem to preserve the planarity and rigidity in the lowest excited singlet state.

The high values of φ_T for **3** and **4**, combined with strong absorption in the red region of the visible range could make these molecules promising candidates for photodynamic therapy. Unfortunately, low stability of the neutral forms provides a strong argument against such application.

4.3. Cyclo[n]pyrroles

This part of the work is the last one from a series which was dedicated to the investigation of electronic properties of isomers and expanded porphyrins by MCD experiments, quantum chemical calculations, and theoretical predictions based on the perimeter model. Three cyclo[n]pyrrole compounds have been studied, where n is the number of the pyrrole rings in the macrocycle and changes from 6 to 8. The alkylated derivatives of these molecules, named in the order of increasing the size of the macrocycles, **5**, **6** and **7**, were used in their doubly protonated forms (Chart 4.5).
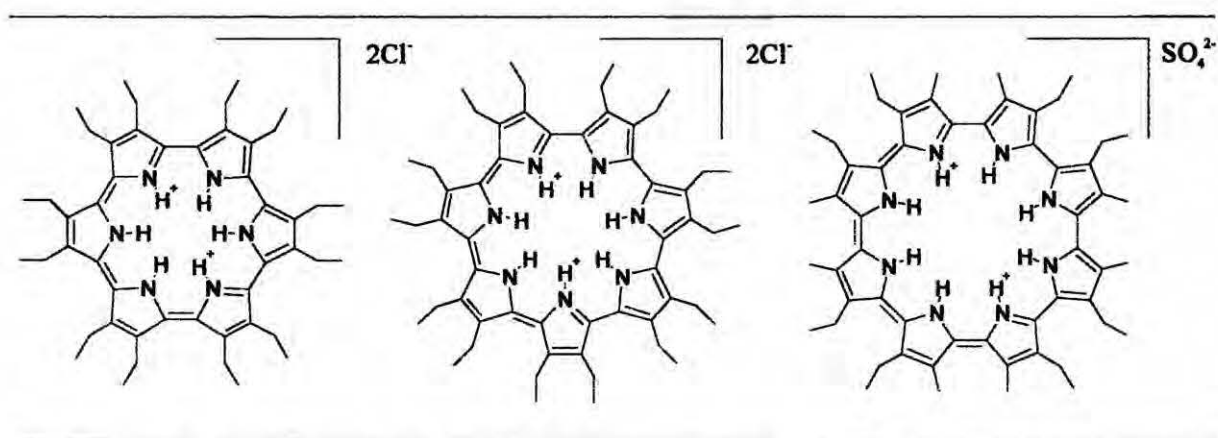
Chart. 4.5.   Left to right: cyclo[6]pyrrole, cyclo[7]pyrrole and cyclo[8]pyrrole.

A wonderful property of these compounds is a high symmetry of the chromophores, which provides perfect examples of molecules whose electronic properties such as absorption intensities and MCD parameters, A and B terms, are easy to predict based on the perimeter model only. These predictions remain in a good agreement with the experiments, as well as DFT and INDO/S calculations. The diprotonated systems **5-7** can formally be derived from [n]annulene dications, $C_nH_n^{2+}$ perimeters containing $4N+2$ π-electrons Thus, **5** is obtained from $C_{24}H_{24}^{2+}$ ($N=5$) by a suitable distortion of the perimeter and introducing six -NH- – bridges, as shown in Figure 4.25. For **6** and **7**, the precursors are $C_{28}H_{28}^{2+}$ ($N=6$) and $C_{32}H_{32}^{2+}$ ($N=7$), bridged by seven and eight -NH- – groups, respectively. These perturbations lower the

symmetry of **5-7** from that possessing the 24-, 28- and 32-fold rotation axis to that of 6-, 7- and 8-fold rotation axis, respectively, as long as the chromophore remains planar (or all pyrrole units are tilted by the same value in the same direction). In this case, the orbital splittings and, as follow, the MCD parameters, are dictated by the molecular symmetry and may be predicted without any calculations whatsoever.
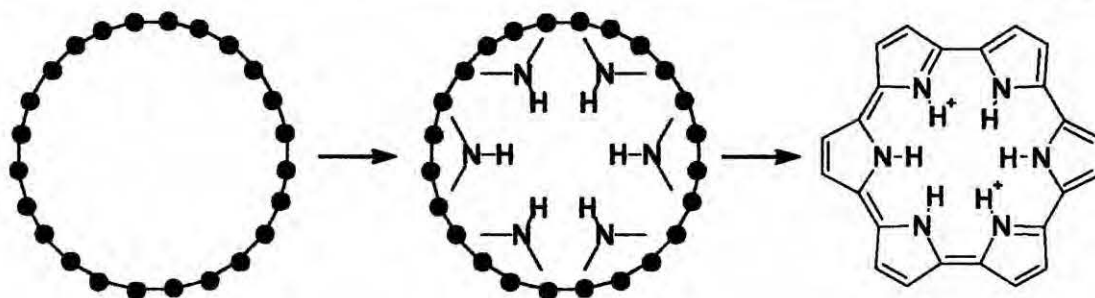
Figure 4.25. Formal derivation of **5** from an 18 π electron perimeter, the [24]annulene dication ($C_{24}H_{24}^{2+}$).

In each of the three molecules under consideration in this study, the parent perimeter n-fold axis is converted into the corresponding (n/m)-fold axis, with m=4. Theoretical analysis for such a case,[5] in which N+1 is an integer multiple of n/2m, shows that, on the basis of symmetry alone, the pair of HOMO orbitals should remain degenerate. On the other hand, the two LUMOs should split. The origin of LUMO splitting is easy to visualize upon inspection of the shape of molecular orbitals of the parent perimeter. This is illustrated for **5** in Figure 4.26, where the real form of the frontier orbitals is used. Bridging should have no effect for one orbital of the LUMO pair, since the NH groups are located on nodes. On the contrary, the other orbital should be strongly destabilized, since contributions from each NH bridge add up. The energies of both HOMO orbitals should be shifted by the same amount.
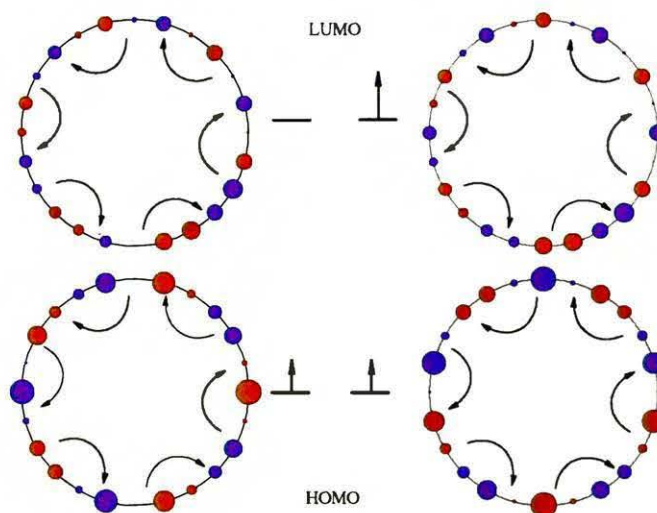
Figure 4.26. The shapes of the HOMO and LUMO orbitals of the parent $C_{24}H_{24}^{2+}$ perimeter, and the predicted response to the perturbation corresponding to the formation of cyclo[6]pyrrole.

The same pattern, ΔHOMO = 0 and ΔLUMO $\neq$ 0, is expected for **5-7**, corresponding to a negative-hard chromophore. Therefore, all three molecules should reveal very similar absorption and MCD patterns. The predictions can be summarized as follows:

1. two degenerate $\pi\pi^*$ electronic transitions (L and B, in the order of increasing energy) should be observed in the low energy region of the electronic absorption

2. because of disparity between ΔHOMO and ΔLUMO, the L/B intensity ratio is expected to be quite high

3. since the HOMO-LUMO separation should decrease from **5** to **7**, the location of L and B transitions should be shifted to the red as the size of the macrocycle increases

4. due to the degeneracy of both the L and B states, both A and B terms should be revealed in the MCD spectra

5. the A terms should be negative for both L and B transitions, with the former being of larger magnitude

6. the B terms should be positive for the L states and negative for the B states.

Figures 4.27-4.29 show the absorption and MCD spectra for **5-7**. The location of the absorption maxima and the values of the Faraday parameters are given in Table 4.19. As expected, the three molecules indeed show very similar spectral features. A low-lying transition is observed in the near-IR region, followed by another one, of comparable absorption intensity, in the visible range. These transitions are located at highest energies in **5** and at lowest in **7**. The A terms are negative for both L and B transitions, with their absolute values being about 3-5 times larger for the former. The B terms are positive for the L transitions and negative for the B states, exactly as predicted.
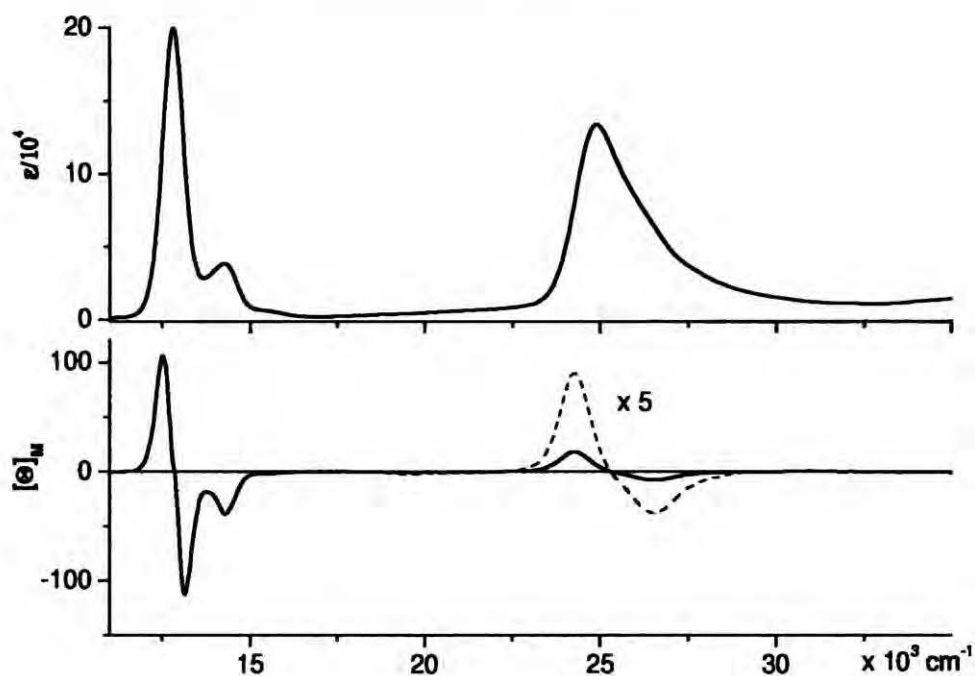
Figure 4.27. Electronic absorption (top) and MCD (bottom) spectra of **5** in DMSO acidified with perchloric acid.
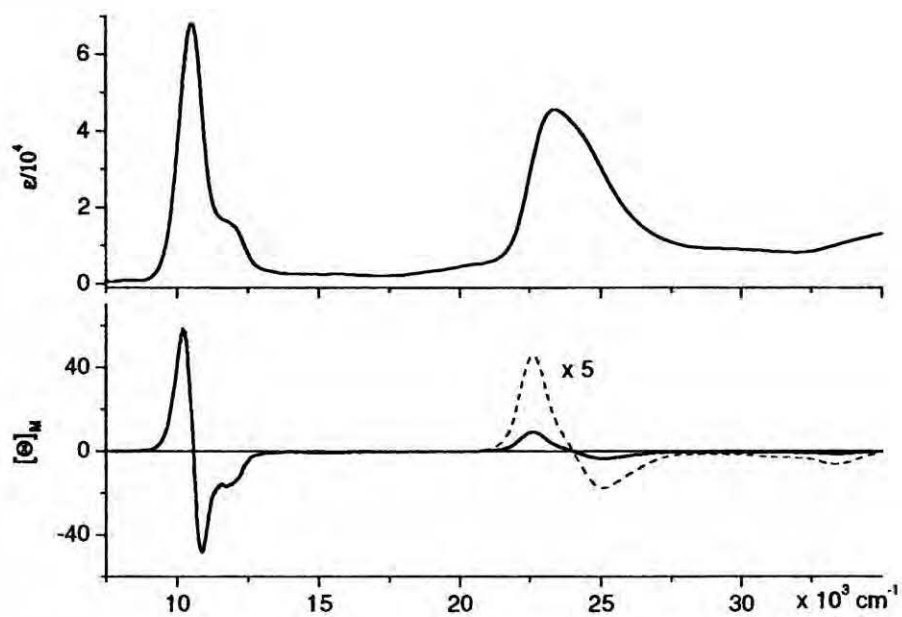
Figure 4.28. Electronic absorption (top) and MCD (bottom) spectra of **6** in DMSO acidified with perchloric acid.
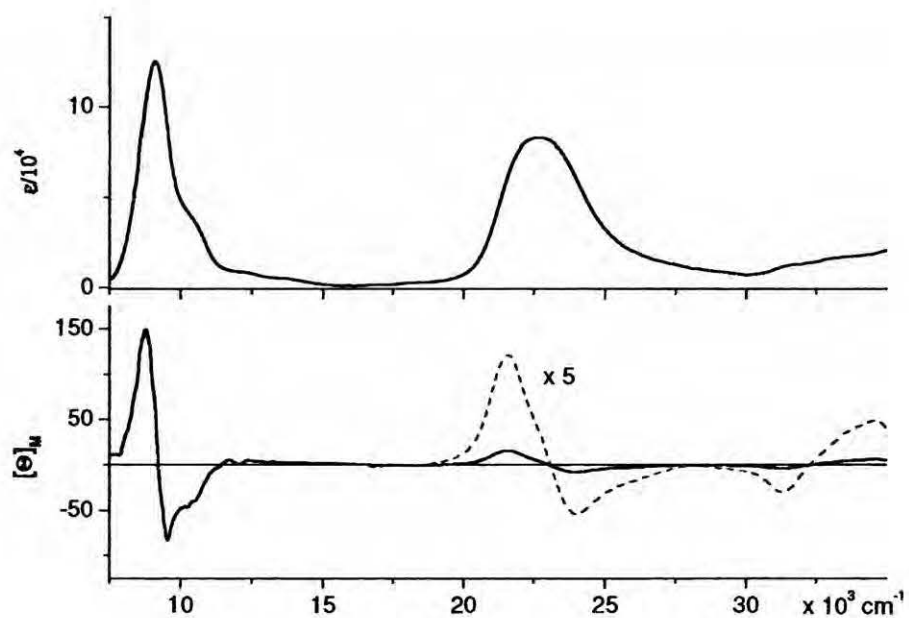
Figure 4.29. Electronic absorption (top) and MCD (bottom) spectra of **7** in DMSO acidified with perchloric acid.

Table 4.19. Absorption and MCD characteristics of **5-6**.

	L transition				B transition			
	$\tilde{\nu}_0$ [a]	f [b]	A [c]	B [d]	$\tilde{\nu}_0$ [a]	f [b]	A [b]	B [c]
1	12.8	0.88	-192	67	24.9	1.38	-40	-8.2
2	10.5	0.42	-145	7.2	23.4	0.62	-29	-6.6
3	9.1	1.03	-354	20	22.6	1.43	-122	-28

[a] 10^3 cm^{-1}; [b] oscillator strength; [c] D^2/μ_B; [d] $10^{-3}D^2/\mu_B$ /cm^{-1}, μ_B is the Bohr magneton.

These results can be analyzed in a more quantitative fashion, using the formulas obtained previously.[5] The ratio of the dipole strengths, $D(L)/D(B)$ should vary as $\tan^2\beta$, where β, in the case of negative hard chromophore, where ΔHOMO=0, is a measure of LUMO splitting only. Therefore, following Eqs. (1.49), (1.50) and (1.52), the expression for β can be written as:

$$\tan(2\beta) = \Delta LUMO/[E(B) - E(L)] \tag{4.2}$$

Using the ratio of experimentally obtained dipole strengths (Table 4.19), β values of 48^0, 51^0, and 53^0 are obtained for **5**, **6** and **7**, respectively. These values are very large, which is as expected, given the finding that the dipole strengths are larger for the L transitions. However, such values of β, should lead, according to eqs. (1.26)-(1.27) to similar values for the A terms in L and B states, whereas the experiments shows that these values are in fact larger for the L bands. Actually, the extreme value of β predicted by the perimeter model is 45^0: it corresponds to the same intensities of L and B transitions, identical A terms and the same absolute values of B terms. We, therefore, used another approach to estimate the values of β. It is based on the experimental values of A and D combined with appropriate values of $\not{y}^-(n,N)$ and $\not{y}^+(n,N)$. The latter have been computed and tabulated for different values of n and N, and for various charges present on the perimeter.[5] Applying formulas (1.26) and (1.27) we obtain 29^0, 30^0, and 38^0 for the β values in **5**, **6**, and **7**, respectively. These values are close to those estimated previously for magnesium 5,10,15,20-tetraazaporphyrin (38^0), zinc

tetrabenzoporphyrin (28^0), and zinc phthalocyanine (38^0).[56] Also the values of the excited state magnetic moments in the L state (Eq. 1.36): 2.7, 3.5, and $3.1 \mu_B$ for **5, 6,** and **7**, respectively, are quite similar to those reported previously for porphyrins and phthalocyanines. For instance, values of $-3.1 \mu_B$ and $-2.3^{57} \mu_B$ have been estimated for octaethylporphyrin cation and anion, respectively. In metalloporphyrins, the reported values are in the range -5.4 to $-7.0 \mu_B$.[56] One should note that the A signs in this case are opposite to those found in **5-7**, since the symmetry properties of porphyrins and phthalocyanines lead to the degenerate LUMO and nondegenerate HOMO pairs. In cyclo[n]pyrroles, on the contrary, the HOMO orbitals remain degenerate, while the LUMOs split.

Simple considerations based on the molecular size could lead to the expectation that the excited state magnetic moments should be larger in **5-7** than in porphyrins and phthalocyanines, since the area encircled by the π perimeter is larger for the former. However, this is counterbalanced by the fact that in the present case of $0 = \Delta\text{HOMO} < \Delta\text{LUMO}$ the $\mu^-(n, N)$ and $\mu^+(n, N)$ contributions add up destructively (Eqs. 1.57 and 1.58). On the contrary, for porphyrins and phthalocyanines (positive-hard chromophores) $\Delta\text{HOMO} > \Delta\text{LUMO} = 0$. For such a case, the two contributions to the excited state magnetic moment add up constructively.[5]

The values of the $-2A/D$ ratio for B transitions in **5-7** are lower than those for L transition, which results in smaller values of the corresponding magnetic moments: 0.68 1.04, and $1.82 \mu_B$ for **5, 6,** and **7**, respectively.

All these theoretical predictions have been based on the assumption of regular and high symmetries, and thus either a planar geometry was assumed, or a structure in which each pyrrole unit is equally tilted out of the molecular plane in the same direction. The X-ray data show that, in the crystal, the molecules are not planar.[58, 59] In **5** and **7**, each pyrrole unit is tilted out of plane in a fashion opposite to that of its two neighbors, to give a kind of up-

down-up ruffling. While the symmetry is lower in this arrangement, it still remains high, with a C_3 symmetry axis being present in **5** and a C_4 symmetry axis being present in **7**. For **6**, a pure up-down-up alternation is not possible. Indeed, the X-ray structure reveals that two adjacent pyrrole rings are tilted in the same direction.[59] As a consequence, no high-order symmetry axis is present. The lower symmetry may be the cause of the lower values of absorption and MCD intensity values seen in **6** as compared to **5** and **7** (*cf.* Table 4.19).

The B3LYP/6-31G(d,p) geometry optimizations performed for nonalkylated analogs of **5-7** confirm the nonplanarity, although the calculated out-of-plane deviations are smaller than those obtained from crystal structure analysis, about 6^0 as compared with 10^0 for **5** and **7** and 15^0 for **6**. It may be that the larger distortions seen in the crystal structure reflect hydrogen bonding interactions involving the counterions bound on either side of the molecular plane (either two chlorine atoms or two oxygen atoms from a sulfate group). The increased distortion seen in the case of **5-7** could also reflect the effect of steric repulsion involving the alkyl groups. In order to estimate the role of these effects, calculations were performed for additional geometries of the three chromophores. First, an "ideal", high-symmetry planar structure was considered with C_6, C_7 and C_8 symmetry axis present for **5-7**, respectively. For the other extreme, a strongly perturbed nonplanar structure, the X-ray geometries were used that included all the alkyl substituents. The results are compared in Table 4.20.

Table 4.20. Calculated orbital splittings and electronic transition energies.

Method	ΔHOMO[a]	ΔLUMO[a]	L transition[b]	A term[c]	B term[d]	B transition[b]	A term[c]	B term[d]
5								
B3LYP/	0.00	1.30	15.7 (0.43)	-	-	26.4 (1.74)	-	-
6-31G(d,p)[e]	0.00	1.44	12.2 (0.09)	-246	12	27.1 (2.80)	-18	-26
INDO/S[f]	0.00	2.24	13.5 (0.26)	-475	22	30.5 (2.94)	-104	-26
INDO/S[g]	0.09	1.66	11.9 (0.09)[i]	-	-1642	26.9 (1.05)[i]	-	-142
INDO/S[h]			12.0 (0.07)[i]	-	1656	27.2 (1.39)[i]	-	172
6								
B3LYP/6-	0.02	1.32	13.9 (0.53)	-	-	24.9 (2.76)	-	-
31G(d,p)[e]	0.03	1.51	10.3 (0.10)	-	19	25.6 (5.57)	-	-7676
INDO/S[f]	0.01	1.15	10.3 (0.01)	-270	11	25.0 (3.90)	-35	-17
INDO/S[g]	0.18	2.06	10.1 (0.08)[i]	-	-1731	25.5 (1.08)[i]	-	-36
INDO/S[j]			10.4 (0.09)[i]	-	1758	26.1 (1.06)[i]	-	119
7								
B3LYP/6-	0.00	1.34	12.4 (0.66)	-	-	23.3 (3.40)	-	-
31G(d,p)[e]	0.00	1.66	9.0 (0.06)	-727	30	24.2 (4.05)	-91	-64
INDO/S[f]	0.00	0.57	8.3 (0.01)	-85	5	22.9 (4.30)	-45	-11
INDO/S[g]	0.21	2.39	9.0 (0.08)[i]	-	-1602	23.7 (1.32)[i]	-	-28
INDO/S[k]			9.6 (0.13)[i]	-	1646	25.8 (1.07)[i]	-	-102

[a] eV; [b] 10^3 cm^{-1}, oscillator strength in parentheses; [c] D^2_{AB}; [d] $10^{-3} D^2_{AB}$ /cm^{-1}; [e] transition energies calculated using TD-DFT; [f] optimized B3LYP/6-31G(d,p) geometry; [g] "ideal", high-symmetry planar geometry; [h] X-ray geometry of 2,3,6,7,10,11,14,15,18,19,22,23-dodecaethyl-cyclo[6]pyrrole; [i] energy splitting due to loss of symmetry; [j] X-ray geometry of 2,3,6,7,10,11,14,15,18,19,22,23,26,27-tetradecaethyl-cyclo[7]pyrrole; [k] X-ray geometry of 2,7,10,15,18,23,26,31-octamethyl-3,6,11,14,19,22,27,30-octaethyl-cyclo[8]pyrrole.

The calculations reveal that the out-of-plane deviations do not change the orbital splitting patterns predicted for high-symmetry chromophores. The calculated values of ΔHOMO and ΔLUMO show that the former are practically degenerate, whereas the latter are separated by large values. Somewhat surprisingly, quasi-degenerate HOMO orbitals are obtained even for **6**, the chromophore of lowest symmetry. Thus, while the nonplanar geometry may influence the absolute values of Faraday terms and the ability of absorption for **5-7**, the generalized predictions from the perimeter model remain still good.

Table 4.20 also presents the energies and oscillator strengths calculated for the four transitions which are described by the perimeter model. Both L and B states are computed as quasi-degenerate. No other electronic states are predicted near L, but several transitions, usually of low intensity, are computed in the vicinity of B. With the increased nonplanarity, more and more allowed transitions are computed close to the B states. This may accidentally result in unrealistically high values of the Faraday parameters, such as, for instance, those calculated in the B region for the DFT-optimized structure of **6**. Naturally, the X-ray geometries do not lead to *A* terms, but the calculated pseudo-*A*-term patterns nicely agree with the predictions obtained for higher symmetry.

The INDO/S method yields the L transition energies closer to the experimental ones, whereas the B states are somewhat better reproduced by TD-DFT. The sums of squares of the four CI coefficients describing the excitation within four frontier orbitals are usually close to 1, indicating that the perimeter model description is a good one and that the use of this model for systems such as **5-7** is both useful and appropriate.

4.4. Conclusions

Our work indicates that MCD experiment, combined with theoretical predictions, based on a simple perimeter model analysis, offers an excellent method of investigation of the electronic structure of aromatic molecules. This method allows us both to describe the electronic properties of molecules and to predict changes of these properties upon chemical or photophysical influences. In addition, basing on the perimeter model, it is possible to produce different derivatives and isomers of the investigated molecules with well-defined properties obtained by appropriate changes in substitution.

Seven compounds, differing in a π-system size and symmetry, were carefully investigated using the methods described above. All compounds were found to exhibit a "model-like" behavior of a system conforming to a four orbital model developed to interpret the spectral behavior of porphyrinoids. This behavior allowed us to use the predictions based on a perimeter model to understand the MCD patterns and describe the electronic properties.

Both experiment and theory demonstrate a soft character of the corrphycene chromophore and its spectral consequences, which place this molecule very close to porphyrin, and far from the negative-hard chromophores porphycene or hemiporphycene.

The approximate equality of orbital splittings in corrphycene can be easily destroyed by structural perturbations, such as, e.g., substitution. The sign of the resulting ΔHOMO - ΔLUMO difference, should be strongly position-dependent. That could make MCD spectroscopy an attractive tool for further studies of corrphycene derivatives.

The negative-hard character of the hemiporphycene, **IS** and **MOIS** chromophores implies a relatively strong absorption in the visible region and thus predict possible applications of these particular systems as a sensitizers, e.g. in photodynamic therapy. On the other hand, some other conditions are required for a successful use in this particular application area, namely high yield of triplet state and singlet oxygen formation efficiencies,

and photochemical stability. Unfortunately, a low stability of the neutral forms of **IS** and **MOIS** precludes using these compounds in such an exciting particular area as photodynamic therapy. Nevertheless, the species that were investigated here by simple theoretical analyses could be a starting point for the design of new substances with expected spectral and photochemical properties. In particular, strong negative-hard character, and, in consequence, intense absorption bands in the visible region, should be expected for porphyrin-(2.2.0.0) and porphyrin-(4.0.0.0), as well as for the pentapyrrolic system, pentaphyrin-(0.0.0.0.0). These molecules remain yet to be synthesized.

The last investigated compounds are three doubly protonated cyclo[n]pyrroles that exhibit the perfect example of high-symmetry chromophores and allow, once again, to confirm the power of the perimeter model. The application of this model leads to the prediction of two degenerate electronic transitions of comparable intensity for these species. Both transitions should exhibit a negative A terms, whereas the B terms should be positive for the L transition, and negative for the B transition. All these predictions are perfectly confirmed by experiment. The patterns expected for a planar chromophore are not changed even when the deviations from planarity are considered.

Chapter 5. Photochromism of β-thioxoketones

5.1. Introduction

This part of the current work is dedicated to the investigation of four compounds, named β-thioxoketones. These species have been known for their chelating properties[60-61] and as models for tautomeric and conformational equilibria.[62-73] More recently, one of the simplest β-thioxoketones, thioacetylacetone, has been proposed as a convenient model for the study of laser-induced reversible phototransformation.[74-75] However, the structures of the initial form and of the photoproduct, and the mechanism of photoreaction have remained an object of debate.[76] In addition, no quantitative measurements of the photoreaction parameters have been performed before: the previous papers reporting on photochromism of β-thioxoketones were only of qualitative nature.

All four investigated compounds undergo a phototransformation upon UV/VIS light irradiation, as illustrated for **9** in Figure 5.1.
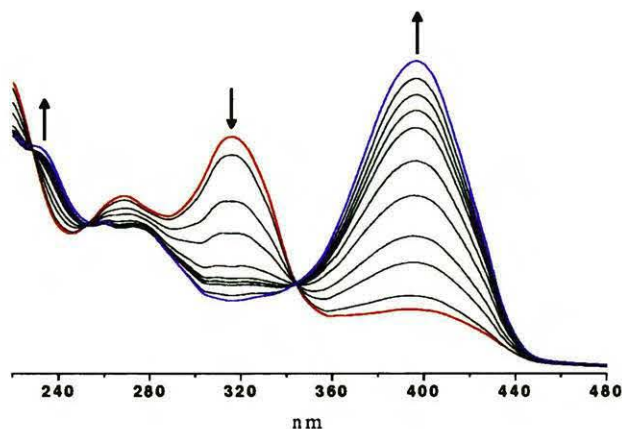
Figure 5.1. Phototransformation in p-methylbenzoylthioacetone: changes in the electronic spectrum observed upon irradiating the solution in 3-methylpentane at 110 K with 410 nm light.

The present work is devoted to the determination of the photoreaction parameters (kinetics and quantum yields), structural and vibrational assignment of the initial and the final (photoproduct) forms, and elucidation of the mechanism of phototransformation in four β-thioxoketones: thioacetylacetone (**8**), *p*-methylbenzoylthioacetone (**9**), thio(p-methylbenzoyl)acetone (**10**) and monothiodibenzoylmethane (**11**), Chart 5.1.
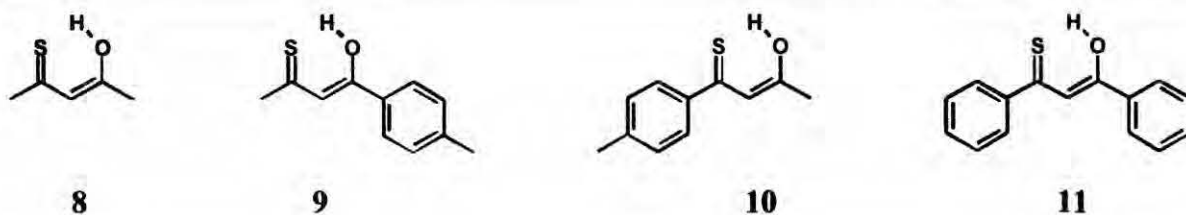
Chart 5.1. Left to right: thioacetylacetone (**8**), thio(*p*-methylbenzoyl)acetone (**9**), *p*-methylbenzoylthioacetone (**10**) and monothiodibenzoylmethane (**11**).

In the first reported investigation[64] of β-thioxoketone photoreactivity at low temperature, the authors concluded that the observed photoprocess was best interpreted as a transformation of an initial (Z)-enol tautomeric form exhibiting a strong intramolecular hydrogen bond (the only observable species at 95 K) into a (Z)-enethiolic counterpart, see Chart 5.2, forms (a) and (b), respectively.
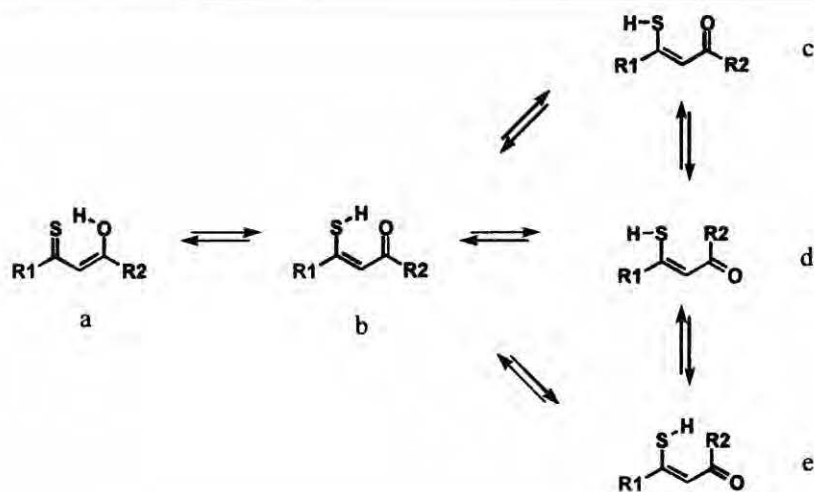
Chart 5.2. Several possible tautomeric and rotameric forms of β-thioxoketones.

However, rotameric substructures of the latter (e.g. (c) and (d)) were not considered at the time. A subsequent study by G bicki and Krantz[76-77] of the phototransformation of thioacetylacetone isolated in an argon matrix led these authors to propose that the photoproduct corresponds to a tautomeric non-chelated (Z)-enethiol form (an analogue of (d) of Chart 5.2) obtained during irradiation of the initial chelated (Z)-enethiol form (an analogue of (b) of Chart 5.2) through rotation around the central single C-C bond of the latter. These authors denied the existence of the (Z)-enol tautomeric form as well as the possibility of a phototransformation through rotation of the thiol SH group. Recently, NMR investigations of 11[65] pointed to the ground state equilibrium between (a) and (b), with a very low interconversion barrier. On the other hand, X-ray and neutron diffraction studies demonstrated that monothiodibenzoylmethane exists in the crystalline state solely in the hydrogen-chelating enolic form (a).[78] This finding questions the suggested C-C bond rotation mechanism, because the latter assumes the predominance of the enethiol form. In view of the controversy surrounding the structure of the photoproduct in β-thioxoketones, we decided to reinvestigate the mechanisms of phototransformation. We have monitored the evolution of electronic and infrared (IR) spectra upon UV/VIS irradiation of 8-11 in various media (solutions, glasses, rare gas cryogenic matrices, KBr tablets and polymer films) and at different temperatures. Decisive structural assignment of the phototransformation product was obtained by FTIR matrix isolation studies of the vibrational spectra of investigated species before and after irradiation, combined with B3LYP/cc-pVDZ quantum chemical calculations of the vibrational spectra for various possible forms. The results strongly suggest that the photoproduct corresponds to a rotameric (Z)-enethiol form, (c). This implies a two-step mechanism for the photoprocess, since the most stable ground-state form corresponds to the (Z)-enol tautomeric form (a).

5.2. Photophysics and structural assignment

The electronic spectra of all β-thioxoketones exhibit a four bands structure (λ_1-λ_4, see Table 5.1) in the visible and UV regions.

Table 5.1. Spectral properties of the studied β-thioxoketones.[a]

Compounds	8	9	10	11	Transition type
λ_1, nm	237	235	239	265	$\pi\pi^*$
λ_2, nm	296	259, 275	330	325	$\pi\pi^*$
λ_3, nm	356	396	375	410	$\pi\pi^*$
λ_4, nm	455	470	528	520	$n\pi^*$

[a]measured in 3-methylpentane

The first three bands (λ_1-λ_3) are of high intensity, corresponding to $\pi\pi^*$ transitions, while the last, lowest energy one (λ_4) shows low intensity and corresponds to an $n\pi^*$ transition. The photoconversion upon light irradiation into λ_3 transitions for all compounds is manifested by the decrease in the intensity of some bands in the visible and near UV regions and the appearance of new bands, shifted to the blue (Figures 5.2-5.5).
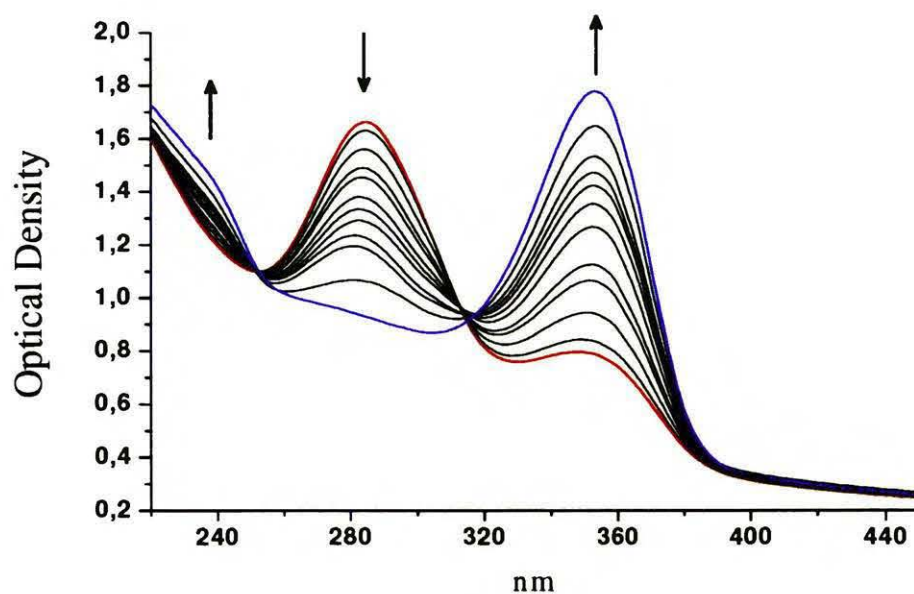
Figure 5.2. Electronic absorption spectra of **8** after irradiation (disappearance of the photoproduct and reappearance of the substrate) observed upon irradiating the solution in 3-methylpentane at 110 K with 360 nm light.
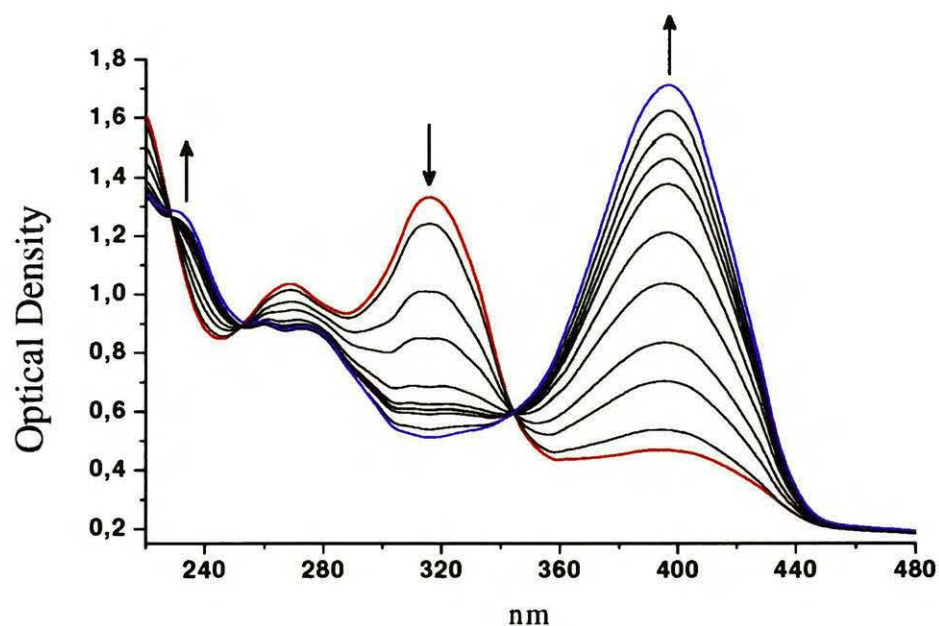
Figure 5.3. Electronic absorption spectra of **9** after irradiation (disappearance of the photoproduct and reappearance of the substrate) observed upon irradiating the solution in 3-methylpentane at 110 K with 400 nm light.
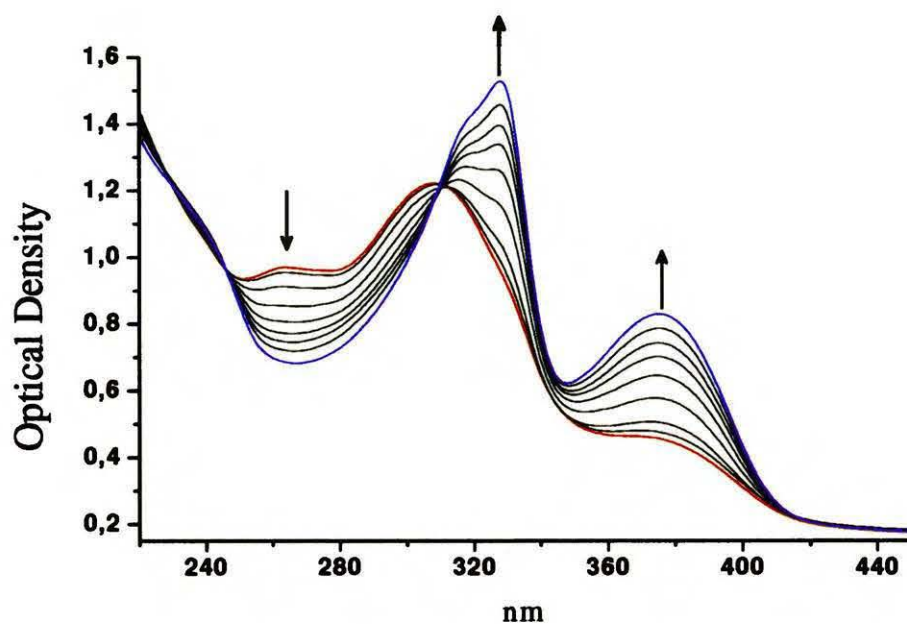
Figure 5.4. Electronic absorption spectra of **10** after irradiation (disappearance of the photoproduct and reappearance of the substrate) observed upon irradiating the solution in 3-methylpentane at 115 K with 380 nm light.
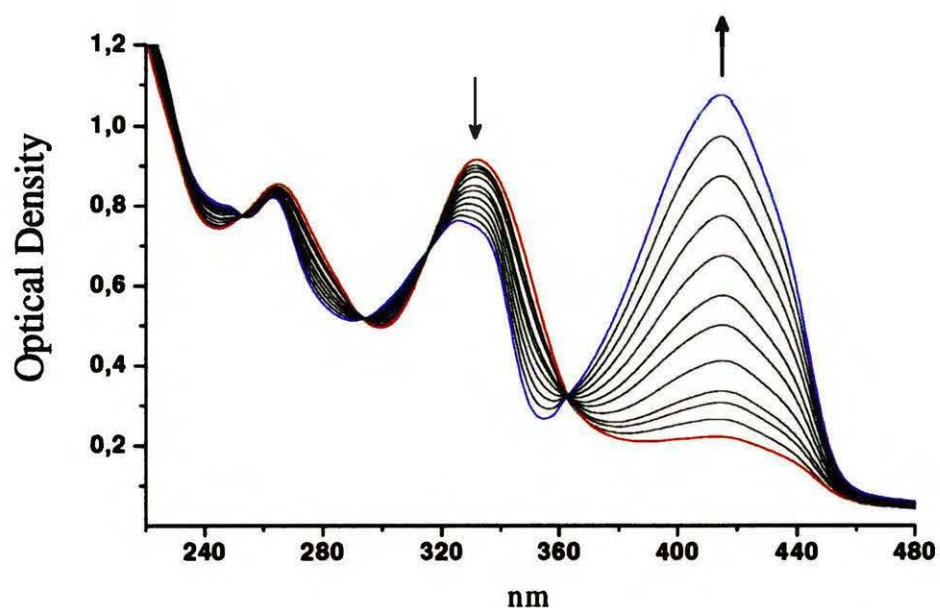
Figure 5.5. Electronic absorption spectra of **10** after irradiation (disappearance of the photoproduct and reappearance of the substrate). observed upon irradiating the solution in 3-methylpentane at 100 K with 410 nm light.

The photoprocess occurs even at liquid helium temperatures, while the back reaction is strongly temperature-dependent and leads to complete recovering of the initial spectrum of enol (see Figures 5.6-5.8).
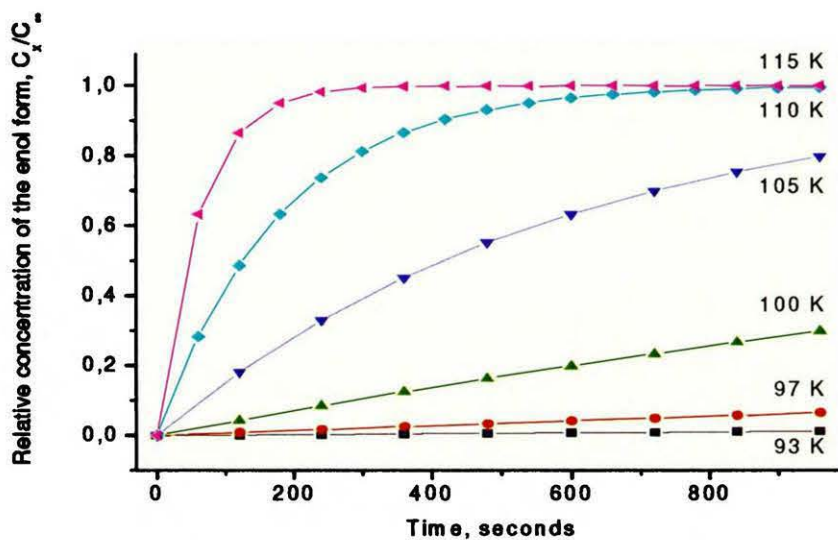
Figure 5.6.   Kinetics of the back reaction (enol formation) from the photoproduct in **11** at various temperatures.
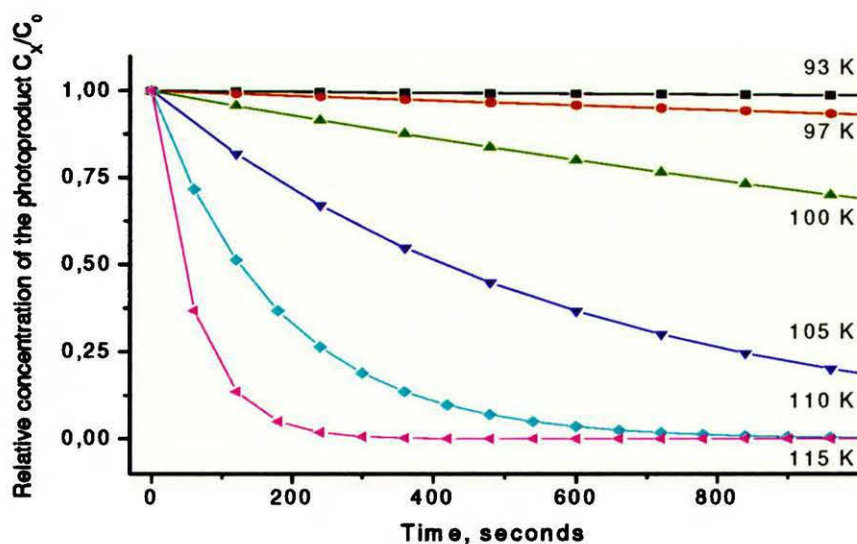
Figure 5.7.   Kinetic curves of the photoproduct disappearance measured for **11** at various temperatures.
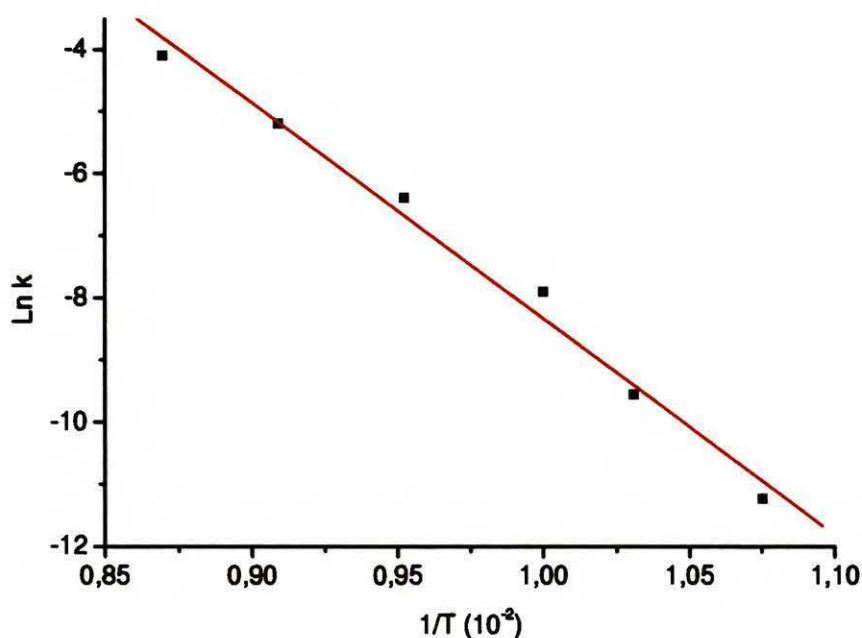
Figure 5.8.   Arrhenius plot for the ground state back reaction in **11** leading from the photoproduct to the initial form.

The photoproduct lifetime stays infinitely large at temperatures below 90 K, which enables detailed spectroscopic characterization of the final form appearing after the phototransformation. Moreover, the reirradiation into long-wavelength absorption bands (λ_1^{ph} = 290, 310, 315, 326 nm for compounds **8-11**, respectively) of the photoproduct, kept at low temperatures, allows to recover the original spectrum of the substrate. The quantum yields of the photoreaction are presented in Table 5.2. Similar results were obtained for different media, such as rare gas matrices at low temperature or polymeric films.

Table 5.2. Quantum yields of the photoreaction[a] and kinetic characteristics of the reverse process (photoproduct → enol) for the studied β-thioxoketones (8-11).

	Quantum yield of photoreaction, Φ, %		Rate constant of the reverse process, K, s^{-1}	Activation barrier for the reverse process, E_{act}, kcal/mol
	Enol→Photoproduct	*Photoproduct→Enol*		
8	4.8	8.2	$3.6 \cdot 10^{-7}$	7.7 ± 0.4
9	1.3	4.7	$3.7 \cdot 10^{-6}$	7.2 ± 0.4
10	4.4	9.5	$5.9 \cdot 10^{-6}$	6.8 ± 0.4
11	1.3	3.4	$5.1 \cdot 10^{-6}$	6.9 ± 0.4

[a]in 3-methylpentane at 90 K.

The quantum yield of the photoreaction was determined by ferrooxalate actinometry.[79] Irradiations were carried out in regular 10-mm square cell. The representative light flux values were 5.4×10^{-7} einstein/min at 300 nm and 7.9×10^{-7} einstein/min at 400 nm.

The quantum yields of phototransformation are rather low, see Table 5.2, probably, because of existence of other efficient competitive processes: internal conversion and/or intersystem crossing. The involvement of the latter process is not clearly confirmed by transient ns-absorption experiment that was done for monothiodibenzoylmethane: the excitation at 337 nm (with a nitrogen laser) gives only one transient species with a lifetime of 4 ns. The mechanism of energy dissipation and the nature of transient species remain unclear and require further investigations.

The temperature-dependence studies of the back reaction exhibits approximately the same values of the activation barrier: 7.7, 7.2, 6.8, and 6.9 kcal/mol for **8-11**, respectively.

The activation barrier values found for the reverse process (photoproduct→enol) compounds **8-11** are in good accordance with the activation barrier value for thioacetic acid C-S rotation (~7.0 kcal/mol) obtained on the basis of NMR measurement.[80]

The fact that the values found for activation barriers of the reverse process have the same values, 7.3 ± 0.4 kcal/mol for all studied β-thioxoketones enables us to propose that phototransformation process for all β-thioxoketones is linked with S-H rotation.

The IR spectra of the most stable form of **8-11**, recorded in Ar matrix at 20 K, are presented on top of Figures 5.9-5.12. These spectra show good agreement with the IR spectra of enol forms, obtained by theoretical calculations (B3LYP/cc-pVDZ, B3LYP/cc-pVTZ). The phototransformation of the enol form of **8-11** leads to significant changes in the IR spectrum. The most characteristic change is the appearance (bottom of Figures 5.9-5.12) of new bands in a region of a conjugated carbonyl group 1650-1700 cm^{-1} and in the region of 2550 cm^{-1} (the region of a non-chelated SH stretch). In addition, the C=C stretching band shifted in the region of low energy and the C-O stretching band, located, depending on the species, in the region from 1450 to 1500 cm^{-1}, disappear. The changes in the IR spectra upon light irradiation are exhibited at the bottom of Figures 5.9-5.12. The IR spectra of the photoproducts are compared with the quantum chemical predictions of the vibrational structure of enethiolic forms.
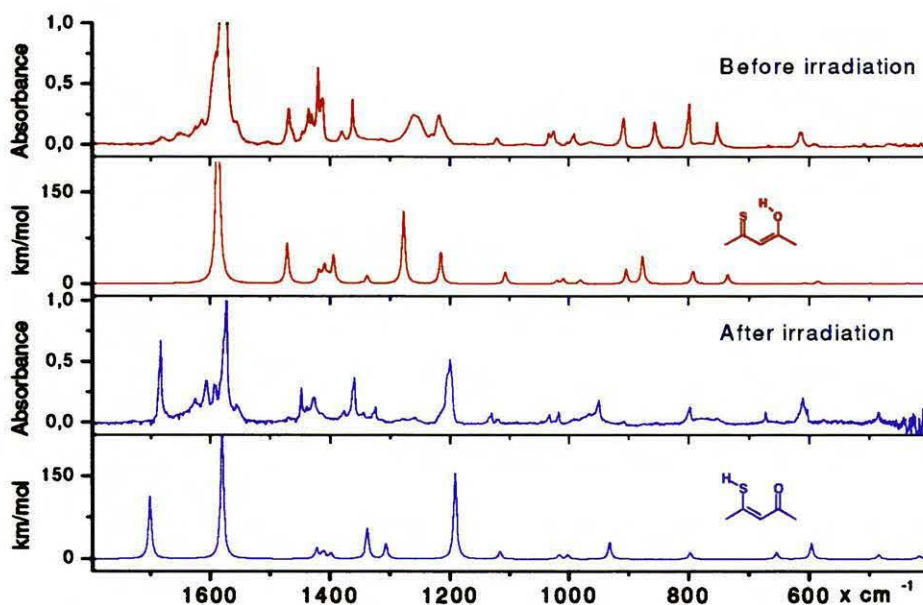
Figure 5.9.   Top - IR spectra of **8** (Ar matrix, 20 K) measured before and after irradiation. Bottom - theoretical calculations of vibrational transitions for the (Z)-enol (chelated form) and the (Z)-enethiol (non-chelated form).
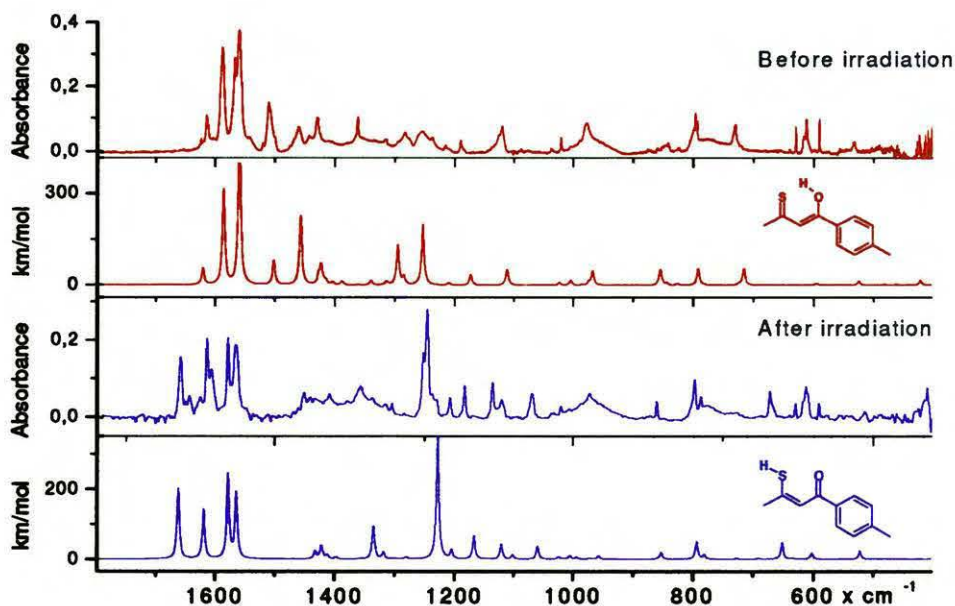
Figure 5.10.   Top - IR spectra of **9** (Ar matrix, 20 K) measured before and after irradiation. Bottom - theoretical calculations of vibrational transitions for the (Z)-enol (chelated form) and the (Z)-enethiol (non-chelated form).
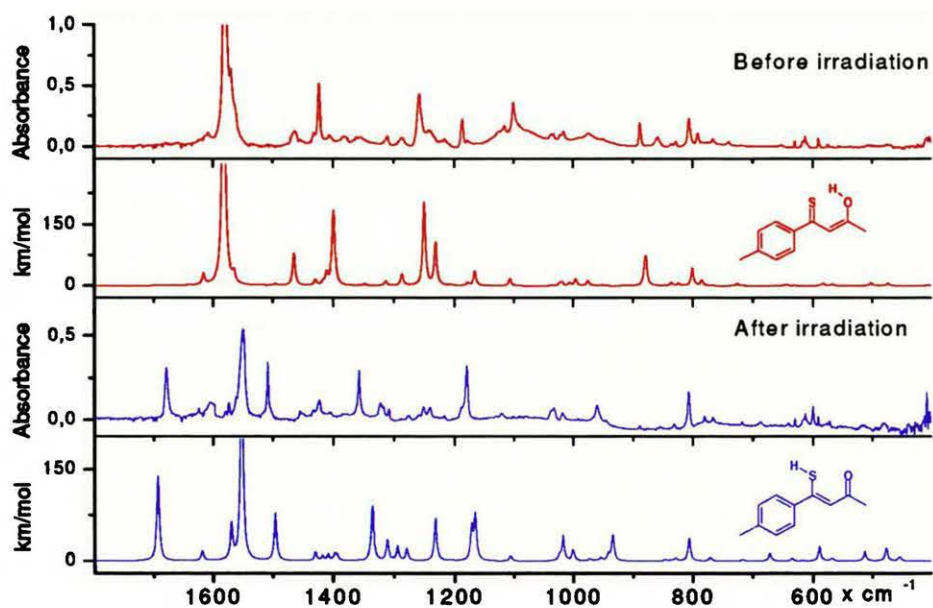
Figure 5.11.   Top - IR spectra of **10** (Ar matrix, 20 K) measured before and after irradiation. Bottom - theoretical calculations of vibrational transitions for the (Z)-enol (chelated form) and the (Z)-enethiol (non-chelated form).
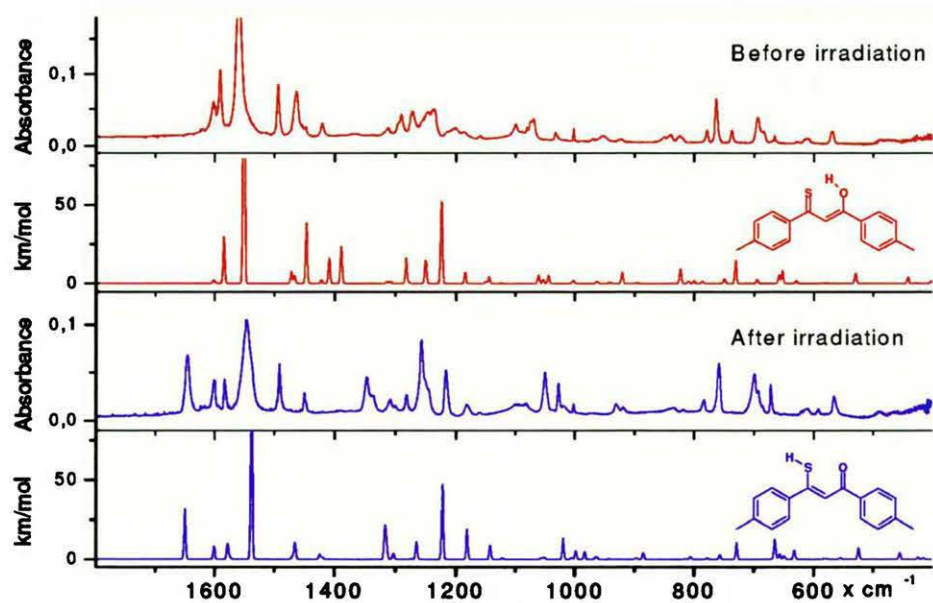
Figure 5.12.   Top - IR spectra of **11** (Ar matrix, 20 K) measured before and after irradiation. Bottom - theoretical calculations of vibrational transitions for the (Z)-enol (chelated form) and the (Z)-enethiol (non-chelated form).

As was described above, the comparison of the experimental spectra, measured before and after irradiation, with the theoretically predicted ones can be helpful in a structural assignment. The calculations were performed for different structures, corresponding to several lowest-energy rotameric and tautomeric forms of **8-11**. Figure 5.13, for example, presents the experimental IR spectrum of the substrate, the enol form of **10**, measured in Ar matrix at 20 K, in comparison with the theoretically predicted vibrational spectra of five different rotameric and tautomeric structures. As shown, the best agreement between experiment and theory is obtained for structure (a), Chart 5.2, corresponding to the (Z)-enol form. Figure 5.14 represents the same sequence of the theoretically predicted spectra, as mentioned above, in comparison with the experimental spectra of the photoproduct. An even better agreement is observed between the theoretical spectra, corresponding to the -SH exo-rotamer of the (Z)-enethiol form of **10** and the experimental data for the final form. This result implies that the mechanism of monothiodibenzoylmethane phototransformation is linked with the SH-group rotation about the C-S bond, most probably according to the sequence: chelated enol (a)→ chelated enethiol (b)→ non-chelated enethiol (c) (see Chart 5.2). Similar results were obtained for other β-thioxoketones.[81-83]
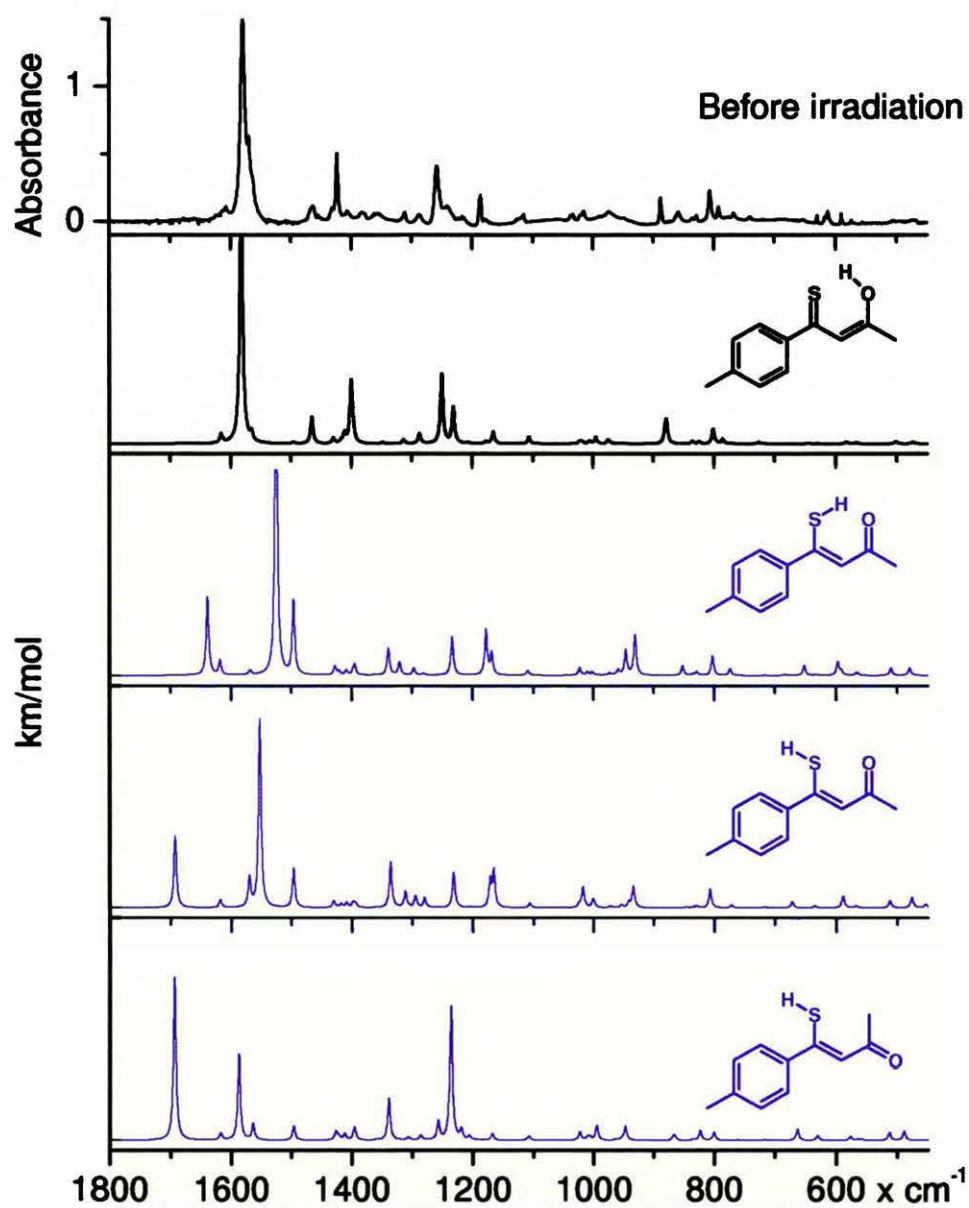
Figure 5.13. Comparison of the experimental IR spectra of thio(*p*-methylbenzoyl)acetone (**10**) before irradiation in an argon matrix at 20 K (top), with the IR spectra predicted for various forms of **10** by B3LYP/cc-pVDZ calculations. The theoretical wavenumbers were scaled by a factor of 0.975; lorentzian line-shape with HWHM 3 cm⁻¹ was used.
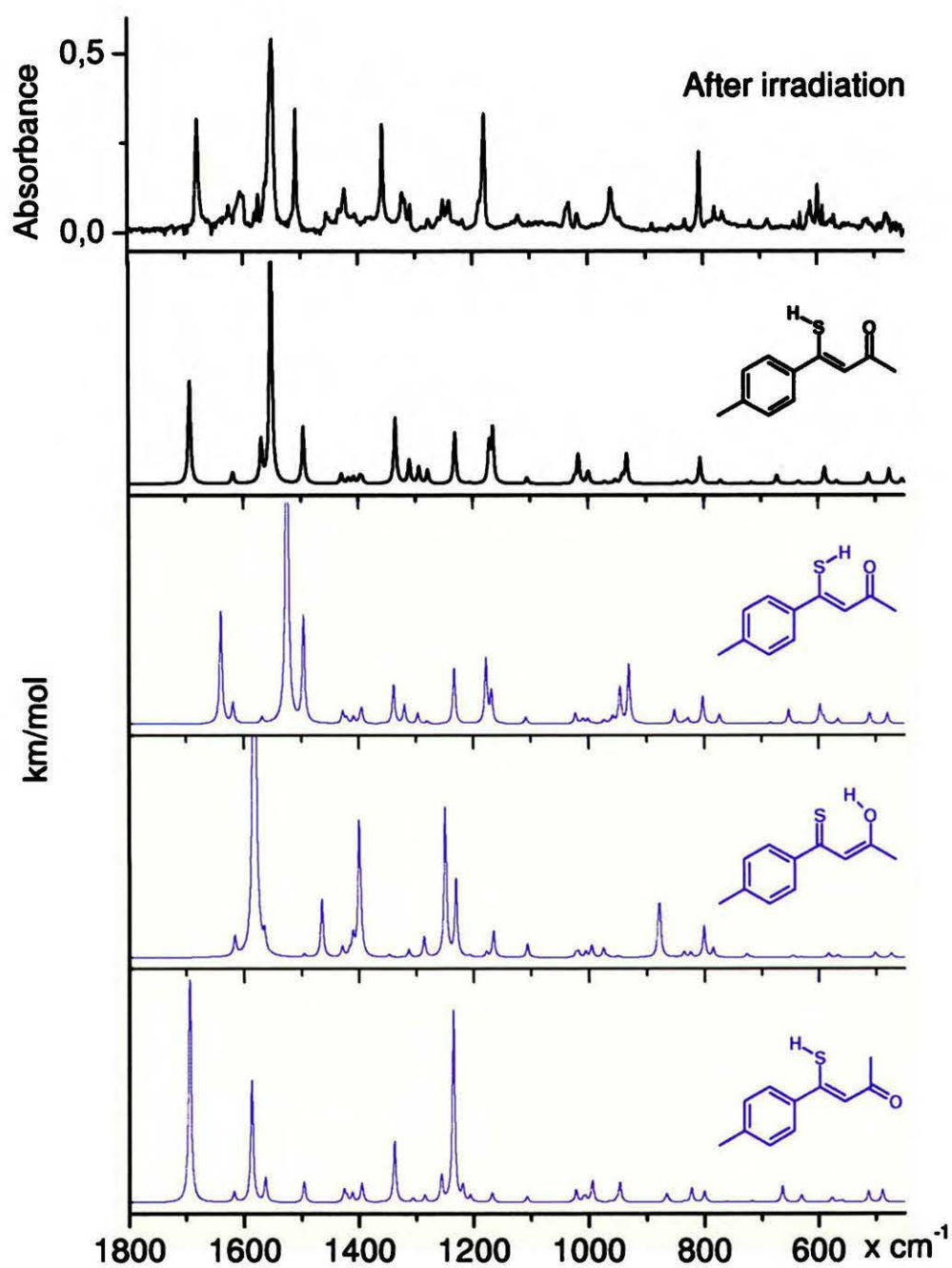
Figure 5.14. Comparison of the experimental IR spectra of thio(*p*-methylbenzoyl)acetone (**10**) after irradiation in an argon matrix at 20 K (top), with the IR spectra predicted for various forms of **10** by B3LYP/cc-pVDZ calculations. The theoretical wavenumbers were scaled by a factor of 0.975; lorentzian line-shape with HWHM 3 cm⁻¹ was used.

Returning to the comparison of the IR spectrum predicted by B3LYP/cc-pVDZ for (a) and (c) within the harmonic approximation with the experimental (Ar matrix, 20 K) IR spectra of the initial structure and the photoproduct (see Figures 5.9-5.12 for details), it is clear to see, that the spectrum predicted for enol (a) is actually in less striking agreement with that observed for the initial form. This can probably be explained by the impact of anharmonic effects associated with the chelated intramolecular hydrogen bonding in (a). These effects are absent in the case of (c). For example, a number of vibrational modes of (a) in the 1400-1600 cm^{-1} region are predicted to involve -OH bending motions and might be influenced by these effects. The calculations performed for malonaldehyde[84] some time ago demonstrate that the anharmonic contributions can reduce the predicted wavenumber of the OH-stretching mode by more than 500 cm^{-1}. The present second-order perturbation analysis of the enol form of **8** predicts an anharmonic shift of more than 600 cm^{-1} for the OH-stretching mode.[82] In reality, the anharmonic calculations predicted a wavenumber close to 2200 cm^{-1} for this mode, which is actually 200-300 cm^{-1} lower than the experimentally measured value. In the case of other vibrational modes, the inclusion of anharmonic effects leads to excellent overall agreement with the experimental wavenumbers (Figure 5.15).
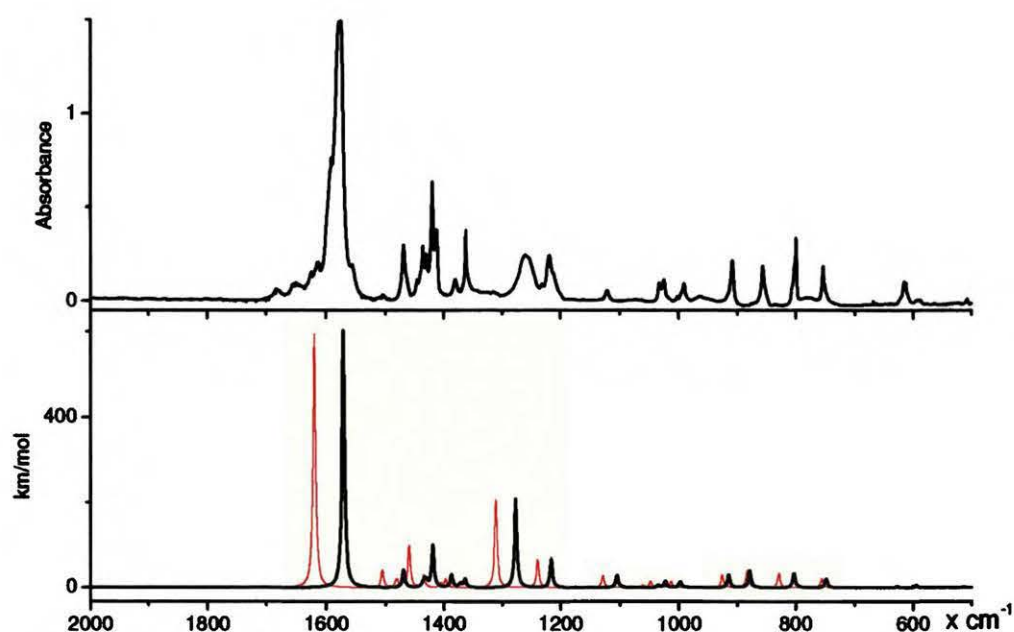
Figure 5.15.   Top: IR spectrum of the initial form (argon matrix, 20 K) of **8**. Bottom: red - vibrational pattern calculated for the enol form of **8** in a harmonic approximation and black – after applying a correction for anharmonicity.

Discarding the disagreement of the OH-stretching mode frequency, a least-squares scaling regression analysis led to a scaling factor $\alpha=1.0028$ and a standard deviation SD=12.4 cm^{-1} (the corresponding data for the harmonic wavenumbers are $\alpha=0.9663$ and SD= 14.7 cm^{-1}). The corresponding experimental data in comparison with the theoretical calculations are presented in Table 5.8, where the vibrational frequencies obtained in harmonic field approximation are given in parentheses.

The comparison of isotopomers of 8

The arguments for structural assignments that were mentioned above are not the only ones. LD measurements and the analysis of IR spectra obtained in carbon tetrachloride at 293 K for four different isotopomers of **8** present independent confirmations. The plots of observed vs. calculated frequencies of **8** and different isotopomers: undeuterated molecule of

8; singly deuterated, **8**-d_1; containing only one light hydrogen isotope, **8**-d_7; fully deuterated, **8**-d_8, are presented in Figures 5.18-5.21. Similar plots obtained for the initial and the final form of **8** recorded in Ar matrix at low temperatures before and after phototransformation are presented in Figures 5.16-5.17.
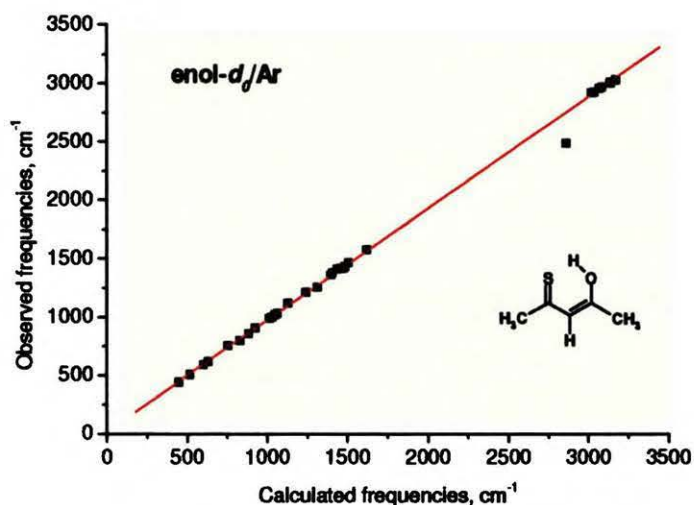
Figure 5.16   Correlation between the experimentally observed vibrations (argon matrix, 20 K) and the frequencies calculated for the enol form of **8**.
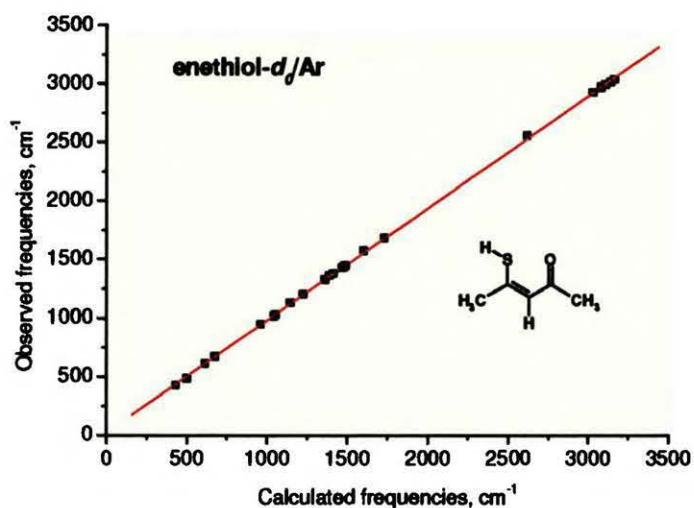
Figure 5.17   Correlation between the experimentally observed vibrations (argon matrix, 20 K) and the frequencies calculated for the enethiol form of **8**.
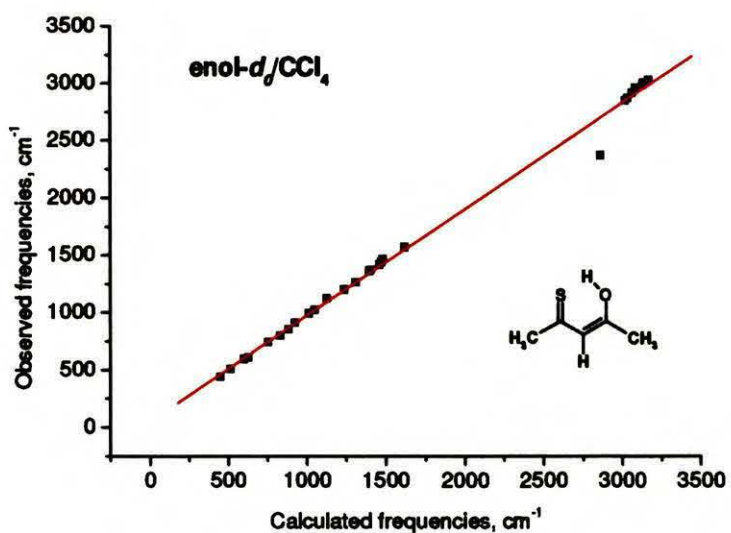
Figure 5.18   Correlation between the experimentally observed vibrations (CCl₄ solution) and the frequencies calculated for the undeuterated enol form of **8**.
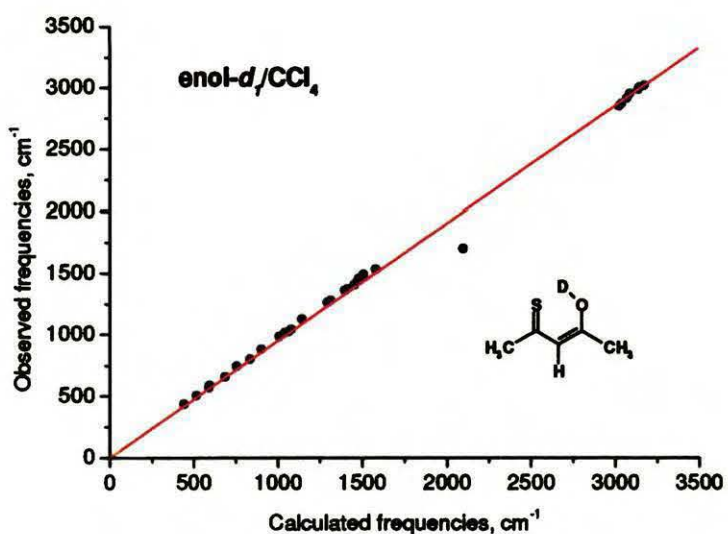
Figure 5.19   Correlation between the experimentally observed vibrations (CCl₄ solution) and the frequencies calculated for the singly deuterated (*d₁*) enol form of **8**.
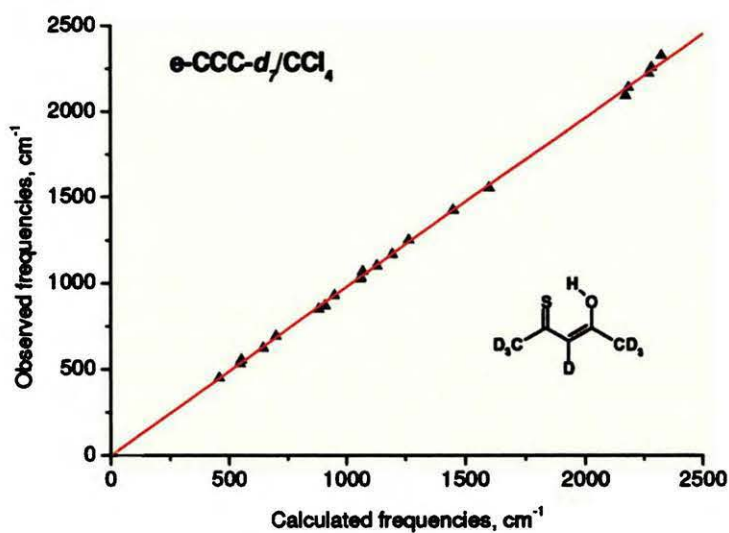
Figure 5.20   Correlation between the experimentally observed vibrations (CCl₄ solution) and the frequencies calculated for the deuterated enol form of **8** (*d₇*), containing only one light hydrogen isotope.
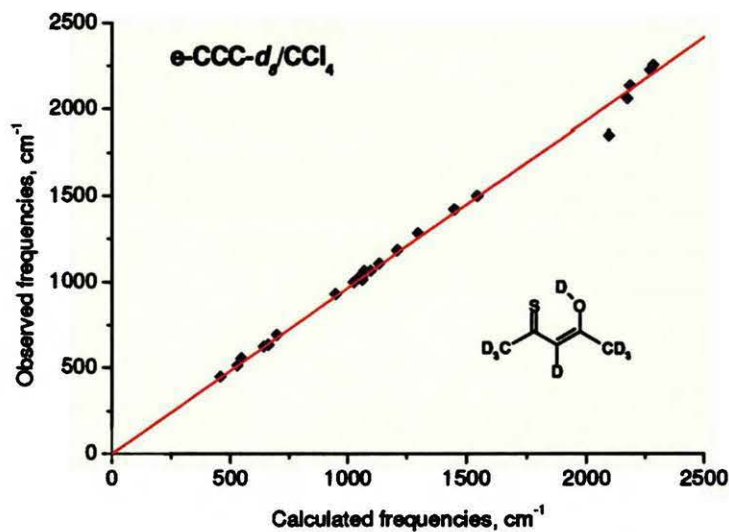
Figure 5.21   Correlation between the experimentally observed vibrations (CCl₄ solution) and the frequencies calculated for the fully deuterated enol form of **8** (*d₈*).

As is clearly shown, all experimental vibrational frequencies are in good agreement with experiment, except for the OH stretching frequency, which is computed too high by about 500 cm^{-1} (see Table 5.8).

Table 5.3. Experimental (CCl$_4$ solution at 293 K) and calculated values of the vibrational transitions of various isotopomers of the enol form of **8**.

	d_0 (exp.)	d_0 (theor.)[a]	d_1 (exp.)	d_1 (theor.)	d_7 (exp.)[b]	d_7 (theor.)	d_8 (exp.)	d_8 (theor.)
v_1	3025 sh	3170 (9.80)	3020 sh	3170 (9.65)		2339 (3.79)		2339 (4.76)
v_2	3002	3140 (8.28)	3004	3140 (6.49)		2325 (2.46)		2325 (3.63)
v_3	2992	3135 (8.67)	2990	3135 (2.48)	2325	2323 (3.97)		2323 (4.00)
v_4	2959	3085 (5.32)	2956	3085 (5.33)	2255	2282 (2.58)	2255	2282 (2.57)
v_5	2918	3067 (8.90)	2917	3067 (8.91)	2220	2269 (4.93)	2225	2269 (4.92)
v_6	2870 sh	3036 (10.2)	2870 sh	3036 (8.23)	2138	2183 (1.65)	2135	2183 (3.76)
v_7	2850	3020 (8.53)	2850	3020 (8.50)	2091	2172 (2.63)	~2060	2172 (2.64)
v_8	2370	2862 (422.8)	~1700	2094 (302.6)	-	2862 (429.0)	~1850	2094 (300.4)
v_9	1570 (vs)	1620 (474.0)	1532 (vs)	1579 (381.6)	1553 (vs)	1600 (514.0)	1499 (vs)	1545 (473.3)
v_{10}		1505 (32.7)	~1490	1505 (39.9)	1025 sh	1058 (15.8)	1028	1058 (10.5)
v_{11}		1483 (6.15)		1483 (6.2)	1070	1069 (3.0)	1065	1069 (3.33)
v_{12}	1466	1481 (11.3)	1461	1480 (10.7)	1034	1060 (12.9)	1035	1053 (12.6)
v_{13}	~1440	1472 (8.68)	1442	1472 (8.3)		1060 (4.12)	1015	1060 (3.77)
v_{14}	1417	1460 (77.6)	1408	1452 (98.6)	1422	1451 (92.0)	1420	1449 (115.3)
v_{15}		1435 (23.7)	1044?	1077 (35.7)		1415 (88.3)	1065	1096 (18.0)
v_{16}	~1370	1405 (7.69)	1373	1411 (4.7)	1103	1129 (15.9)	1108	1132 (22.6)
v_{17}	1361	1397 (16.2)	1360	1397 (16.7)		1049 (0.01)	999	1026 (28.5)
v_{18}	1262	1311 (164.2)	1278	1313 (154.3)	1168	1195 (75.4)	1183	1209 (75.4)
v_{19}	1200	1240 (52.6)	1263?	1293 (22.9)	1249	1264 (84.1)	1282	1297 (52.8)
v_{20}	1125	1129 (22.9)	1127	1141 (5.4)	930	949 (0.8)	929	948 (2.2)
v_{21}		1062 (4.5)	~1025?	1062 (5.3)	871	908 (8.2)	871	908 (4.8)
v_{22}	1026	1049 (12.3)	1015	1037 (38.5)		832 (6.0)		832 (6.8)
v_{23}		1027 (0.61)		1027 (1.1)		862 (0.9)		863 (0.1)
v_{24}	993	1014 (11.0)	988	1006 (19.0)		795 (5.9)		791 (5.1)
v_{25}	912	926 (24.0)	882	899 (10.2)	-	889 (4.8)	-	864 (0.4)
v_{26}	857	884 (32.3)	660	685 (12.0)	850	881 (37.1)	635	660 (22.8)
v_{27}	800	829 (27.1)	802?	831 (14.5)	624	644 (6.4)	624	641 (1.07)
v_{28}	746	755 (16.8)	745?	753 (17.1)	693	698 (17.8)	694	697 (18.2)
v_{29}	611	630 (2.43)	568	587 (15.7)	533	545 (3.4)	514	528 (8.4)
v_{30}	595	600 (4.49)	587	592 (4.4)	556	551 (3.4)	556	545 (3.2)
v_{31}	507	516 (1.33)	507	515 (0.7)	450	456 (1.5)	450	456 (1.3)
v_{32}	440	447 (1.06)	435	440 (0.92)		412 (1.8)		403 (1.7)
v_{33}		363 (2.78)	479?	358 (3.09)		336 (1.42)		333 (1.71)
v_{34}		334 (5.59)		333 (3.53)		313 (3.89)		311 (3.81)
v_{35}		231 (1.71)		228 (1.70)		211 (1.1)		210 (1.1)
v_{36}		174 (0.03)		174 (0.02)		150 (0.07)		150 (0.06)
v_{37}		129 (0.55)		128 (0.56)		120 (0.05)		119 (0.04)
v_{38}		124 (0.37)		124 (0.33)		93 (0.51)		93 (0.51)
v_{39}		66 (0.33)		66 (0.34)		48 (0.08)		48 (0.09)

[a] intensities (km/mol) in parentheses; [b] OH stretching vibration could not be observed for d_7 isotopomer.

The explanation of the behavior observed for the OH stretching vibration, as was mentioned above, is related to the anharmonicity of this vibration in the chelated form.

Vibrational assignments

All four compounds were measured in two kinds of rare gas matrices (Ar, Xe) before and after irradiation. The compounds were irradiated into a corresponding $\pi\pi^*$ state of **8-11**, at 360, 400, 380 and 410 nm, respectively. The IR spectra obtained for the initial forms (before irradiation) and for the final forms (after irradiation) were carefully compared with theoretical predictions of vibrational structures for several low-energy isomers and rotamers of **8-11**. The best agreements were obtained for the enethiol and the enol forms corresponding to the photoproduct and the substrate, respectively. Under this assumption, more than half of all vibrations were characterized for both forms of all compounds (Tables 5.8-5.15). In the cases of **10** and **11** no any other forms were detected. The situation differs a little for compounds **8** and **9**, where the chelated enol is the dominant form before irradiation, but some weaker bands reported in Figures 5.9-5.10 and in Tables 5.8 and 5.10 do not disappear upon irradiation and, therefore, have to be assigned to another isomer than the enol. An obvious candidate is the chelated enethiol form, whose calculated energy is only slightly higher than that of the enol form. The calculations predict that the three strongest IR bands of the chelated enethiol form of **8** should lie at 1695, 1582, and 1224 cm^{-1}, in nice agreement, also with regard to relative intensities, with the observed transitions at 1654, 1553, and 1212 cm^{-1}. Similar situation occurs for compound **9**, whose three bands observed at 1624, 1543 and 1235 cm^{-1} correspond to those predicted by theory at 1655, 1576 and 1267 cm^{-1}. These bands are therefore assigned to the chelated (Z)-enethiol form, in agreement with the results of NMR studies, where, in addition to the dominant enol form, presence of small amount of the (Z)-enethiol form (~ 5 %) for **8** and **9** was also postulated.[62, 65]

Polarization measurements.

Additional help in the vibrational assignments was provided by polarized spectroscopy experiments. The photochromic transformation induced by linearly polarized light results in initiating the photochemical reaction preferentially in those molecules whose corresponding transitions dipole moment are collinear with the direction of light polarization. This produces anisotropic samples with the oriented photoproduct and the partially aligned substrate. LD measurements on such photooriented samples yield information about the directions of vibrational transition moments with respect to the direction of the moment of the electronic transition that was excited during irradiation.[85]

It can also be mentioned that the dichroic effect (see Eq. 1.23) should be strongest for the product at the initial stages of irradiation, when only a small fraction of the photochromic form has been obtained. The opposite should be true for the initial form. In this case, the effect should be most pronounced when the remaining population consists of a small number of those molecules that cannot practically absorb z-polarized light, since they have their transition moments perpendicular to z. These predictions have been confirmed experimentally. The Tables 5.4-5.7 represent the orientation factors K_i (Eq. 1.20) which were determined from LD measurements (Eq. 1.23) of **10** for both, the product and the substrate upon irradiation at 514 nm ($n\pi*$ state) and 410 nm ($\pi\pi*$ state). The values of K_i, $K_i^{'}$ and $K_i^{''}$ exhibit the changes in LD at different stages of irradiation and, as was explained above, indicate that the molecules of the photoproduct lose the anisotropy at the final stage of the irradiation (the orientation factors approach the value of 0.33), in contrast to the substrate, of which the orientation at times close to the end of the irradiation is improved.

It needs to be said that better LD signals were observed for compounds **9** and **10**, species with a single p-methylphenyl substituent at the carbon atoms adjacent to either oxygen or sulfur. This may have two origins: 1) the assumption of pure out-of-plane or in-plane polarization at the wavelength of irradiating light may not be strictly valid, as the $\pi\pi*$

band can overlap with an nπ* transition; 2) the molecules may not be rigidly held in the matrix, but may change their positions somewhat during the phototransformation process. The latter is more probable in the case of small molecule of **8**.

The LD signals observed for the initial forms exhibit higher dichroic ratios than those of the photoproduct (Tables 5.4-5.7). As it was previously mentioned, the quantum yield of the photoreaction is rather low (Table 5.2). The other ways of energy dissipation are still not clear, but no luminescence was detected. This allows us to propose that large part of the energy of higher excited states is used for heating the neighboring rare gas environment of the molecules due to radiationless transitions and vibrational relaxation. Therefore, these molecules which are finally converted into the photoproduct have some more degrees of freedom to rotate and change their position upon excitation with polarized light, whereas for the molecules of the initial form which are not excited, the position remains unchanged.

The most accurate LD measurements were done for compound **10**. The interpretation of the LD results is presented below. Under assumption that the z axis in the laboratory system of coordinates corresponds to the direction of light polarization and, as follows, to the orientation of molecules induced by photoselection process, the relation between the orientation factors K_i and the value of the angle α_i, which the direction of the i-th transition moment forms with the z axis can be written as:[86]

$$\tan^2 \alpha_i = \frac{K_z - K_i}{K_i - K_x} \tag{5.1}$$

The LD of the out-of-plane (the molecular plane is defined as a plane which consists of oxygen, sulfur, and the carbon atoms in-between) polarized transition of the substrate observed at 888.6 cm^{-1} (out-of-plane bending of the O-H group) is positively polarized in the case of irradiation into the ππ* state (410 nm), for which the electronic transition is in-plane polarized. For this situation, the in-plane polarization direction defines the molecular z axis,

while the x and y axes, equivalent with regard to orientation, correspond to the out-of-plane direction, and to the in-plane direction perpendicular to z, respectively. If the error in the estimation of the dichroic ratio for the 888.6 cm^{-1} vibration is small, we can use the following limiting assumptions. We have $K_x = K_y = 0.39$ (Table 5.7), therefore $K_z = 0.22$ (Eq. 1.21) and the absolute value of the angle α_i can be written as:[86]

$$\alpha_i = \arctan\left(\frac{K_i - 0.22}{0.39 - K_i}\right)^{\frac{1}{2}}$$

The results for six different transitions are presented in Table 5.7. The vibration at 1423.2 cm^{-1} corresponds to another out-of-plane vibration, that of the CH$_3$ group (calculated at 1454 cm^{-1}). It should, therefore, exhibit the same orientation factor and the same value of α_i, 90^0, as the 888.6 cm^{-1} vibration; this is indeed observed. The vibration at 1464.4 cm^{-1} is assigned, based on the DFT calculations, to the clear in-plane stretching vibration of the C-O group and allows us to estimate the value of the in-plane angle which the direction of the first $\pi\pi^*$ transition forms with the C-O group. This angle, with the experimentally determined value of 25^0, gives information about the orientation of the $\pi\pi^*$ transition into the molecular framework (the calculated value is 31^0). The sign of LD should be changed upon irradiation into the $n\pi^*$ state (a pure $n\pi^*$ state is perpendicular to $\pi\pi^*$ state). In fact, as is shown in Table 5.5, the dichroism of two out-of-plane vibrations (at 1423.2 and 888.6 cm^{-1}) changes to negative (the orientation factors are smaller than 0.33). On the contrary, the dichroism of the in-plane vibration of the C-O group becomes positive (the orientation factor is larger than 0.33).

The values of the orientation factors in the case of the irradiation into the $n\pi^*$ state are close to each other in all but one case (the in-plane vibration of the C-O group). This could suggest similar transition moment directions. However, this is not consistent with the results

obtained upon irradiation into the $\pi\pi^*$ state. The explanation of such behavior may be that the direction of the transition dipole moment of the $n\pi^*$ state is not exactly perpendicular to the molecular plane but forms an angle that lower than 90^0. The calculations yield the angle of ~10^0 with the molecular plane. An additional argument is that for an electronic transition polarized exactly perpendicular to the molecular plane, the expected value of K_z should be $1 - 2\times0.44 = 0.12$ for out-of-plane polarized vibrational transitions. The experimentally obtained values are definitively higher. Moreover, they are not strictly equal for the 1423.2 and 888.6 cm^{-1} vibrations, which shows that the assumed parallelity of their transition moments is only approximate.

Table 5.4.   Linear dichroism of the photoproduct, the exo-thiol form of **10** measured in Ar matrix at 20 K upon 514 nm (nπ* state) light irradiation. The LD spectra were obtained at three different stages of irradiation.

IR band, cm^{-1}	Sign of LD	Tendency of K	K_i	$K_i^{'}$	K_i^{*}
1678.8[a]	+	↓ [b]	**0.35**	**0.34**	**0.34**
1549.4	+		0.35		
1508.6	+	↓	**0.37**	**0.36**	**0.36**
1356.7			**0.33**	**0.33**	**0.33**
1322.5	+	↓	**0.39**	**0.39**	**0.35**
1179.6	+	↓	0.36	0.35	0.35

[a]bold – pure, non-overlapping bands; [b]↓ decrease and ↑ increase of LD signals at different stages of irradiation, respectively

Table 5.5.   Linear dichroism of the substrate, the chelated enol form of **10** measured in Ar matrix at 20 K upon 514 nm (nπ* state) light irradiation. The LD spectra were obtained at two different stages of irradiation. See caption to Table 5.4 for details.

IR band, cm^{-1}	Sign of LD	Tendency of K	K_i	$K_i^{'}$
1579.7	-		-	0.26
1464,4	+	↑	**0.43**	**0.44**
1423.2	-		**0.27**	**0.26**
1258.4	-	↓	0.28	0.26
1186.6	-		0.3	-
888.6	-	↓	**0.24**	**0.20**

Table 5.6. Linear dichroism of the photoproduct, the exo-thiol form of **10** measured in Ar matrix at 20 K upon 410 nm ($\pi\pi*$ state) light irradiation. See caption to Table 5.4 for details.

IR band, cm^{-1}	Sign of LD	Tendency of K	K_i	K_i'	K_i''
1678.8	-	↑	**0.30**	**0.31**	**0.33**
1549.4	+	↓	0.38	0.38	0.34
1508.6	+	↓	**0.35**	**0.36**	**0.34**
1356.7	+	↓	**0.4**	**0.40**	**0.36**
1322.5	-	↑	**0.29**	**0.29**	**0.30**
1179	+	↓	0.36	0.36	0.34

Table 5.7. Linear dichroism of the substrate, the chelated enol form of **10** measured in Ar matrix at 20 K upon 410 nm ($\pi\pi*$ state) light irradiation. See caption to Table 5.4 for details.

IR band, cm^{-1}	Sign of LD	Tendency of K	K_i	K_i'	K_i''	α_i^{exp} [a], deg	α_i^{thr} [b], deg
1579.7	-		-	0.31	0.30	43	46
1464,4	-	↓	**0.3**	**0.27**	**0.25**	**25**	**31**
1423.2	+	↑	**0.35**	**0.37**	**0.39**	**90**	**57**
1258.4	+		0.33	0.33	0.33	54	60
1186.4	+		0.33	0.33	0.33	54	28
888.6		↑	**0.33**	**0.36**	**0.39**	**90**	**87**

[a]The calculated (α_i^{thr}) and [b]experimentally obtained (α_i^{exp}) angles between the direction of the transition dipole moment ($\pi\pi*$ state) and the directions of vibrational transition dipole moments

Table 5.8.   Vibrational assignments for the enol form of 8[a].

		Exp.				Calc.		
		$\tilde{\nu}$ (cm^{-1})				$\tilde{\nu}$ (cm^{-1})[b]	I (km/mol)	Approximate mode description
	Ar	CCl$_4$	Vapour					
ν_1	3035 sh	3025 sh		a'		3171 (3049)	9.80	C3-H s
ν_2	3014 w	3002 w	3013			3141 (2994)	8.28	CH$_3$ s
ν_3	3004 w	2992 w				3136 (3002)	7.67	CH$_3$ s
ν_4	2931 w	2918 w	2930			3037 (2929)	10.20	CH$_3$ s
ν_5	2922 w					3021 (2915)	8.53	CH$_3$ s
ν_6	2490 w	2370 w	2500			2862 (2188)	422.8	OH s (ν_{OH})
ν_7	1578 vs	1570 vs	1580			1620 (1571)	474.4	OH b, C=C s
ν_8	1468 m	1466 w	1465			1506 (1469)	32.7	C-O s, C-C s
ν_9	1430 w	~1440 w	1430			1481 (1433)	11.26	CH$_3$ b
ν_{10}	1419 s	1417 m				1460 (1419)	77.60	OH b, C-O s, C-C s
ν_{11}	1412 m					1435 (1387)	23.66	OH b, C=C s
ν_{12}	1380 w	1376 w				1405 (1372)	7.69	CH$_3$ b, OH b, C=C s
ν_{13}	1362 m	1361 m	1365			1397 (1364)	16.21	CH$_3$ b
ν_{14}	1260 m	1262 m	1258			1312 (1277)	164.2	C-C s, C=C s, C-O s
ν_{15}	1218 m	1218 w	1220 sh			1240 (1216)	52.6	C-CH$_3$ s, skel def
ν_{16}	1121 m	1125 m	1121			1130 (1105)	22.96	C-CH$_3$ s, skel def
ν_{17}	1025 w	1026 m	1020			1049 (1023)	12.28	CH$_3$ b, skel def
ν_{18}	991 w	993 w	985			1014 (988)	10.97	CH$_3$ b, C=S s
ν_{19}	909 m	912 m	911			927 (915)	24.03	CH$_3$ b, C-O s, skel def
ν_{20}	753 m	746 m	755			756 (748)	16.80	C=S s, skel def ($\nu_{C=S}$)
ν_{21}	591 vw					600 (595)	4.49	skel def
ν_{22}	440 vw	440				447 (446)	1.06	skel def
ν_{23}						363 (372)	2.78	skel def
ν_{24}						334 (334)	3.58	skel def, C=S b
ν_{25}						230 (240)	1.71	skel def
ν_{26}	2975 vw		2975	a		3087 (2942)	5.32	CH$_3$ s
ν_{27}	2964 w	2959 w	2963	,,		3069 (2927)	8.90	CH$_3$ s
ν_{28}	1436 w					1482 (1436)	6.15	CH$_3$ b
ν_{29}	~1420 m?					1472 (1430)	8.68	CH$_3$ b
ν_{30}	1034 w					1062 (1035)	4.51	CH$_3$ b
ν_{31}	1002 vw					1027 (998)	0.61	skel oop def, CH$_3$ b
ν_{32}	857 m	857 m	857			884 (879)	32.3	OH oop b (γ_{OH})
ν_{33}	799 s	800 m	798			828 (803)	27.14	C3-H oop b (γ_{CH})
ν_{34}	615 w	611 m	610			629 (627)	2.43	skel oop def
ν_{35}	508 vw	507 w	505			516 (514)	1.33	skel oop def
ν_{36}						172 (164)	0.03	skel oop def, CH$_3$ tor
ν_{37}						128 (124)	0.55	C-O oop b, C=S oop b
ν_{38}						120 (109)	0.37	CH$_3$ tor, skel oop def
ν_{39}						56 (-39)	0.33	CH$_3$ tor

[a]sh=shoulder; vs, s, m, w, vw = very strong, strong, medium, weak, very weak, respectively;
skel=Skel et al; def=deformation; oop=out of plane; tor=torsion; [b]Results of anharmonic analysis
given in parentheses, see text.

Table 5.9. Vibrational assignments for the enethiol form of 8.

	Exp.			Calc.		
	$\widetilde{\nu}$ (cm^{-1})			$\widetilde{\nu}$ (cm^{-1})	I (km/mol)	Approximate mode description
	Ar	Xe				
ν_1	3038 vw		a'	3164	8.31	C3-H s
ν_2	3014 w	3009 w		3139	10.21	CH$_3$ s
ν_3	2992 w			3109	15.26	CH$_3$ s
ν_4	2927 w			3027	14.73	CH$_3$ s
ν_5	2927 w			3027	3.68	CH$_3$ s
ν_6	2555 w			2615	29.87	SH s (ν_{SH})
ν_7	1683 s	1682 s		1729	119.0	C=O s, C=C s ($\nu_{C=O}$)
ν_8	1572 vs	1575 vs		1601	252.3	C=C s, C=O s
ν_9	1448 m	1443 m		1489	23.01	CH$_3$ b
ν_{10}	1426 m	1421 m		1467	13.74	CH$_3$ b
ν_{11}	1376 w	1373 w		1412	3.10	CH$_3$ b, C–CH$_3$ s
ν_{12}	1359 m	1359 m		1387	87.58	CH$_3$ b, C–CH$_3$ s
ν_{13}	1324 m	1325 w		1360	26.09	C3–H b, skel def
ν_{14}	1200 s	1202 s		1225	172.2	skel def, C3–H b
ν_{15}	1130 m	1131 m		1146	19.03	C–CH$_3$ s, skel def
ν_{16}	1032 w	1032 w		1053	11.81	Skel def, SH b
ν_{17}				990	0.09	SH b (δ_{SH})
ν_{18}	949 m	951 m		959	32.6	skel def, CH$_3$ b
ν_{19}				926	1.01	skel def
ν_{20}	672 w			672	11.91	C–S s, skel def ($\sim\nu_{C-S}$)
ν_{21}	610 m	612 m		611	28.60	C=O b, C–S s
ν_{22}	427 w			428	4.67	skel def
ν_{23}				357	5.69	skel def
ν_{24}				306	0.65	skel def
ν_{25}				160	6.26	O····S s
ν_{26}	2972 w	2972 w	a''	3080	11.55	CH$_3$ s
ν_{27}	2965 w	2963 w		3079	6.63	CH$_3$ s
ν_{28}	1439			1481	8.07	CH$_3$ b
ν_{29}	1435			1477	9.37	CH$_3$ b
ν_{30}				1062	0.59	skel oop def, CH$_3$ b
ν_{31}	1017 w	1016 w		1042	5.79	skel oop def, CH$_3$ b
ν_{32}	797 m	803 m		829	16.00	C3–H oop b (γ_{CH})
ν_{33}				628	0.48	skel oop def
ν_{34}	483 w			500	8.38	skel oop def
ν_{35}				420	3.03	SH oop b (γ_{SH})
ν_{36}				204	0.00	skel oop def
ν_{37}				154	0.20	skel oop def, CH$_3$ tor
ν_{38}				103	0.50	CH$_3$ tor
ν_{39}				79	4.26	skel oop def, CH$_3$ tor

Table 5.10. Vibrational assignments for the enol form of 9.

	Exp. $\widetilde{\nu}$ (cm^{-1})		Calc. $\widetilde{\nu}$ (cm^{-1})	I (km/mol)	Approximate mode description
	Ar	Xe			
ν_1			3145,4	0,24	CH s
ν_2			3130,5	1,49	CH s
ν_3			3117,1	0,41	CH s
ν_4			3096,5	3,67	CH s
ν_5			3091,5	2,86	CH s
ν_6			3074,3	1,59	CH s
ν_7			3043,1	2,51	CH s
ν_8			3010,1	2,48	CH s
ν_9			3005,8	1,86	CH s
ν_{10}			2952,8	5,49	CH s
ν_{11}			2947,6	1,62	CH s
ν_{12}			2610,7	100,00	OH s (ν_{OH})
ν_{13}	1614 m	1613 m	1620,8	7,85	C=C s (B)[b]
ν_{14}	1588 s	1585 s	1586,1	46,30	O-H b, C3-H b, skel def (B)
ν_{15}	1559 vs, 1567 s	1558 vs	1559,6	79,51	O-H b, C3-H b, skel def (B)
ν_{16}	1510 m	1508 m	1502,1	11,80	skel def, C-H b
ν_{17}	1460 w	1458 w	1457,2	33,78	C-O s, C3-H b
ν_{18}			1427,1	4,13	CH$_3$ b, O-H b
ν_{19}	1429 w	1427 w	1423,0	9,12	CH$_3$ b, O-H b
ν_{20}			1418,8	1,23	CH$_3$ b
ν_{21}			1414,5	1,85	CH$_3$ b
ν_{22}			1403,6	1,34	CH$_3$ b, O-H b, C3-H b, C-H b
ν_{23}			1387,7	1,81	C-H b, skel def, CH$_3$ b
ν_{24}	1361 m	1358 m	1360,8	0,30	CH$_3$ b
ν_{25}			1339,4	2,17	CH$_3$ b
ν_{26}			1314,1	1,72	skel def (B)
ν_{27}			1295,5	19,09	C-H b (B), C3-H, C-C s
ν_{28}	1283 w	1282 w	1285,4	3,70	C-C s, C-H b
ν_{29}	1256 w	1254 w	1253,7	29,69	O-H b, C3-H b, skel def (B)
ν_{30}	1216 vw	1216 vw	1210,3	1,07	C-C s, C-H b (B)
ν_{31}	1190 w	1188 w	1173,4	4,96	C-H b (B)
ν_{32}	1121 w	1120 w	1114,6	1,14	C-H b (B)
ν_{33}			1111,6	7,08	C-H b, C3-H, C-CH$_3$
ν_{34}			1083,0	0,15	C3-H b
ν_{35}			1023,6	1,31	CH$_3$ tor
ν_{36}			1004,7	2,21	skel def (B)
ν_{37}			984,8	0,25	CH$_3$ tor
ν_{38}			974,5	0,14	C-H oop b (B)
ν_{39}	979 m	978 m	974,1	1,28	CH$_3$ b
ν_{40}			967,9	6,73	CH$_3$ b
ν_{41}			954,8	0,17	C-H oop b (B)
ν_{42}			855,3	7,21	O-H oop b (γ_{CH})
ν_{43}			852,5	0,71	O-H oop b (γ_{CH}), skel def
ν_{44}	843 w	845 w	844,7	0,84	C-H oop b (B), C3-H oop b
ν_{45}	824 vw	823 vw	826,5	0,83	C-H oop b (B)
ν_{46}	796.8 m	799 m	792,2	7,96	C3-H oop b
ν_{47}	794 w	796 m	782,7	0,35	C3-H oop b, skel def
ν_{48}	730 m	729 m	724,4	0,76	C-H oop b, C3-H oop b, skel def
ν_{49}			715,8	8,03	skel def
ν_{50}			678,0	0,16	skel oop def
ν_{51}			634,0	0,23	skel def (B)

ν_{52}			595,4	0,97	skel def (B)
ν_{53}	532 w	530 w	524,6	1,93	skel oop def
ν_{54}			480,0	0,43	skel def, skel oop def
ν_{55}			460,9	0,44	skel def, skel oop def
ν_{56}			420,4	2,31	skel def
ν_{57}			402,2	0,01	skel oop def (B)
ν_{58}			381,4	0,32	skel def
ν_{59}			343,8	0,33	skel def
ν_{60}			290,2	0,15	skel oop def
ν_{61}			265,2	0,02	skel def
ν_{62}			232,8	0,32	skel def
ν_{63}			149,5	0,05	skel oop def
ν_{64}			132,4	0,05	skel def
ν_{65}			109,5	0,16	skel def
ν_{66}			57,0	0,01	skel oop def
ν_{67}			40,4	0,10	CH_3 tor
ν_{68}			30,6	0,03	CH_3 tor
ν_{69}			23,2	0,20	skel def tor

[a]B – corresponding to the benzoyl ring.

Table 5.11. Vibrational assignments for the enethiol form of 9.

	Exp. $\widetilde{\nu}$ (cm^{-1})		Calc. $\widetilde{\nu}$ (cm^{-1})	I (km/mol)	Approximate mode description
	Ar	Xe			
ν_1			3133,2	0,95	CH s
ν_2			3130,9	7,91	CH s
ν_3			3114,4	0,84	CH s
ν_4			3091,7	10,32	CH s
ν_5			3087,8	9,47	CH s
ν_6			3044,6	7,33	CH s
ν_7			3040,4	7,44	CH s
ν_8			3015,0	4,47	CH s
ν_9			3008,9	7,00	CH s
ν_{10}			2952,8	7,26	CH s
ν_{11}			2952,3	19,63	CH s
ν_{12}			2528,2	33,47	SH s (ν_{SH})
ν_{13}	1658 s 1644 m ?	1656 s 1642 m ?	1661,7	83,79	C=C s, C=O s, (ν_{CO})
ν_{14}	1624 m ? 1614 s	1612 s	1618,8	58,89	Skel def (B)[a]
ν_{15}	1578 s	1577 s	1577,8	100,00	Skel def (B)
ν_{16}	1565 s 1562 m ?	1561 s	1564,0	77,67	skel def, C3-H b, C=C
ν_{17}			1499,9	0,00	C-C s, C-H b (B)
ν_{18}	1451 w	1450 w	1432,1	9,40	CH$_3$ b
ν_{19}			1421,9	14,79	CH$_3$ b
ν_{20}			1419,2	2,92	CH$_3$ b
ν_{21}	1409 w	1408 w	1411,6	4,59	CH$_3$ b
ν_{22}			1397,1	2,52	Skel def (B), CH$_3$ b
ν_{23}	1356 w	1355 w	1360,8	0,11	CH$_3$ b, C-CH$_3$ s
ν_{24}			1355,2	0,63	CH$_3$ b, C-CH$_3$ s
ν_{25}	1338 vw	1337 w	1334,5	39,33	C3-H b, skel def (B)
ν_{26}	1305 vw	1305 vw	1318,1	7,98	C3-H b, skel def (B)
ν_{27}	1253 s	1252 s	1280,9	2,73	C3-H b, C-H b, C=C s
ν_{28}	1246 s 1230 vw ?	1245 s 1230 w ?	1228,1	150,64	C3-H b, C-H b, C-C s
ν_{29}	1209 w	1209 w	1204,9	10,07	C-CH$_3$ s, skel def (B)
ν_{30}	1184 m	1183 m	1167,1	27,48	C-H b (B)
ν_{31}	1136 m	1136 m	1120,9	17,67	C-H b, S-H b, C3-H b
ν_{32}			1101,6	5,30	C-H b (B)
ν_{33}	1068 w	1069 w	1059,3	15,29	C3-H b, skel def
ν_{34}			1023,6	2,54	skel oop def, CH$_3$ b
ν_{35}			1017,0	1,04	skel oop def, CH$_3$ b
ν_{36}			1005,0	4,39	Skel def (B), C-H b (B), S-H b (δ_{SH})
ν_{37}			994,0	2,20	S-H b
ν_{38}			990,0	0,22	C-H oop b (B)
ν_{39}	973 vw	973 vw	971,9	1,52	skel def, CH$_3$ b
ν_{40}			957,0	4,09	CH$_3$ b, S-H b
ν_{41}			943,9	0,04	C-H oop b (B)
ν_{42}	860 w	860 w	858,3	0,44	C-H oop b (B)
ν_{43}	847 vw		852,6	8,04	Skel def (B)
ν_{44}			829,0	0,04	C-H oop b (B)
ν_{45}	798 m	798 m	793,4	20,70	C3-H oop b, C-H oop b (B)
ν_{46}	787 w	787 w	780,8	4,88	skel def (B)
ν_{47}	724 vw		726,7	0,97	skel def oop (B)

v_{48}			691,0	0,95	C3-H oop b, C-H oop b (B)
v_{49}	672 w	672 w	651,6	19,47	C3-H b, CH$_3$ b, C-S s
v_{50}			633,4	0,76	Skel def (B)
v_{51}	609 vw	609 vw	602,1	7,07	Skel def (B)
v_{52}	514 w	514 w	521,7	9,48	Skel oop def, S-H oop b
v_{53}			467,7	0,13	Skel oop def
v_{54}			459,0	0,20	Skel def
v_{55}			422,1	0,78	S-H oop b
v_{56}			403,2	0,02	Skel def (B)
v_{57}			395,4	4,25	Skel def, S-H b
v_{58}			358,0	7,54	Skel def
v_{59}			347,9	0,08	Skel def
v_{60}			281,1	1,55	Skel oop def
v_{61}			259,7	0,97	Skel def
v_{62}			200,7	0,26	CH$_3$ tor
v_{63}			188,9	2,16	Skel def
v_{64}			152,6	0,02	CH$_3$ tor
v_{65}			114,5	0,44	Skel oop def
v_{66}			96,5	0,56	Skel def
v_{67}			46,1	0,09	CH$_3$ tor, Skel oop def
v_{68}			38,4	0,96	CH$_3$ tor, Skel oop def
v_{69}			8,4	0,41	Skel oop def

^{a}B – corresponding to the benzoyl ring.

Table 5.12. Vibrational assignments for the enol form of **10**.

	Exp. $\widetilde{\nu}$ (cm^{-1})		Calc. $\widetilde{\nu}$ (cm^{-1})	I (km/mol)	Approximate mode description
	Ar	Xe			
ν_1			3127,4	0,28	CH s
ν_2			3127,1	1,19	CH s
ν_3			3115,7	0,54	CH s
ν_4			3091,2	2,29	CH s
ν_5			3089,6	2,11	CH s
ν_6			3072,6	0,95	CH s
ν_7			3040,6	1,90	CH s
ν_8			3022,7	0,64	CH s
ν_9			3008,9	1,77	CH s
ν_{10}			2963,2	1,67	CH s
ν_{11}			2952,2	3,93	CH s
ν_{12}			2636,9	66,18	OH s (ν_{OH})
ν_{13}	1607,5 w	1605,8 w	1617,4	2,69	C=C s (A)[a]
ν_{14}	1579,7 vs	1576,7 s	1583,5	100,00	O-H b, C3-H b, skel def (A)
ν_{15}	1569,9 m	1567,6 m	1566,6	2,48	O-H b, C3-H b, skel def (A)
ν_{16}	1508,6	1506,7 w	1497,3	0,44	skel def, C-H b
ν_{17}	1464,4 w	1462,5 w	1466,3	8,22	C-O s, C3-H b
ν_{18}	1430,7 w	1425,2 w	1430,7	1,43	CH$_3$ b
ν_{19}	1423,2 m	1419,3 m	1418,0	0,76	CH$_3$ b
ν_{20}			1412,1	2,84	CH$_3$ b, O-H b
ν_{21}	1406,4 w	1404,2 w	1402,8	1,00	CH$_3$ b, O-H b
ν_{22}			1400,8	18,28	CH$_3$ b, O-H b, C3-H b, C-H b
ν_{23}	1382,0 w	1381,0 w	1396,7	1,49	C-H b, skel def, CH$_3$ b
ν_{24}	1361,8 vw	1356,6 w	1360,2	0,04	CH$_3$ b
ν_{25}			1349,3	0,42	CH$_3$ b
ν_{26}	1311,2 w	1311,3 w	1314,7	1,13	skel def (A)
ν_{27}	1286,9 w	1286,9 w	1288,1	2,94	C-H b (A)
ν_{28}	1258,4 m	1251,5 w	1251,1	21,05	C=C s (A)
ν_{29}			1232,4	10,82	O-H b, C3-H b, skel def (A)
ν_{30}	1215.9 m	1215,9 w	1208,3	0,29	C-C s, C-H b
ν_{31}	1186,5 w	1187,3 m	1179,2	0,70	C-H b, C3-Hb, O-H b
ν_{32}	1125,2 w	1123,2 w	1166,7	3,73	C-H b
ν_{33}	1115,5 w	1114,3 w	1107,6	1,91	C-H b (asym)
ν_{34}			1023,2	0,67	CH$_3$ tor
ν_{35}	1020,2 w	1018,5 w	1019,3	0,78	CH$_3$ tor
ν_{36}	1015,0	1013,4 w	1006,8	0,79	skel def (A)
ν_{37}	989,6 w	988,6	996,4	1,74	CH$_3$ b, C3-H b
ν_{38}	973,2	972,7 w	976,1	1,31	CH$_3$ b, C3-H b (asym)
ν_{39}			971,6	1,16	CH$_3$ b
ν_{40}			969,1	0,17	C-H oop b (A)
ν_{41}	949,0 w	948,1 w	951,4	0,20	C-H oop b (A)
ν_{42}	888,6 m	887,5 m	881,1	4,26	O-H oop b (γ_{CH}), skel def
ν_{43}		858,7 w	878,9	4,83	O-H oop b (γ_{CH})
ν_{44}	835,5 w	835,5 w	836,9	0,79	C-H oop b, C3-H oop b
ν_{45}	829,2 w	829,9 w	825,4	0,65	C-H oop b, C3-H oop b
ν_{46}	807,0 m	802,3 w	802,0	4,47	C3-H oop b, C-H oop b
ν_{47}	792,4 w	791,2 w	786,0	1,35	C3-H oop b, skel def
ν_{48}	741,0 w	739,6 w	726,9	0,50	skel def
ν_{49}			719,3	0,08	skel oop def, C3-H
ν_{50}	653,4 w	650,0 w	645,7	0,30	skel oop def, O-H oop b, C3-H oop b

v_{51}			631,2	0,06	skel def
v_{52}	590,6 w	589,7 w	583,3	0,59	skel def
v_{53}	574,0 w	573,4 w	567,5	0,36	skel def, CH_3 b
v_{54}			501,9	0,70	O-H b, skel def
v_{55}			474.0	0,64	O-H b, skel def
v_{56}			405,8	0,14	Skel oop def (A)
v_{57}			394,8	0,79	Skel def
v_{58}			352,0	0,15	CH_3 b, skel def
v_{59}			326,0	0,58	CH_3 b, skel def
v_{60}			279,2	0,10	Skel oop def
v_{61}			262,4	0,01	Skel oop def
v_{62}			241,2	0,11	Skel def
v_{63}			171,6	0,12	Skel oop def, CH_3 tor
v_{64}			136,7	0,01	Skel oop def, CH_3 tor
v_{65}			115,0	0,13	CH_3 tor
v_{66}			91,0	0,04	Skel def
v_{67}			66,1	0,08	Skel def
v_{68}			45,4	0,11	Skel def
v_{69}			31,1	0,06	CH_3 tor

[a]A – corresponding to the thiobenzoyl ring.

Table 5.13. Vibrational assignments for the enethiol form of **10**.

	Exp. $\tilde{\nu}$ (cm^{-1})		Calc. $\tilde{\nu}$ (cm^{-1})	I (km/mol)	Approximate mode description
	Ar	Xe			
ν_1			3117,0	3,97	CH s
ν_2			3114,1	8,38	CH s
ν_3			3101,5	2,70	CH s
ν_4			3091,8	14,83	CH s
ν_5			3088,8	13,86	CH s
ν_6			3075,1	10,95	CH s
ν_7			3040,6	13,63	CH s
ν_8			3017,3	9,59	CH s
ν_9			3010,1	13,91	CH s
ν_{10}			2954,1	3,51	CH s
ν_{11}			2952,5	30,60	CH s
ν_{12}			2553,9	26,20	SH s (ν_{SH})
ν_{13}	1678,8 m	1674,6 s	1694,3	110,73	C=C s, C=O s, (ν_{CO})
ν_{14}	1624,6 w	1618,5 w	1619,6	12,25	Skel def (A)[a]
ν_{15}	1574 w		1570,9	44,63	Skel def (A)
ν_{16}	1549,4 s	1544,1 m	1553,6	291,69	skel def, C3-H b, C=C s
ν_{17}	1508,6 m	1507,5 w	1497,5	61,18	C-C s, C-H b (A)
ν_{18}			1430,8	10,68	CH$_3$ b
ν_{19}			1418,9	6,09	CH$_3$ b
ν_{20}			1409,5	7,69	CH$_3$ b
ν_{21}			1398,6	8,18	CH$_3$ b
ν_{22}			1394,7	6,28	Skel def (A), CH$_3$ b
ν_{23}	1356,7 s	1352,2 w	1361,0	0,23	CH$_3$ b, C-CH$_3$ s
ν_{24}	1322,5 w	1321,5 w	1336,5	71,29	CH$_3$ b, C-CH$_3$ s
ν_{25}	1307,6 w	1307,6 w	1312,1	25,44	C3-H b, skel def (A)
ν_{26}			1295,4	17,96	C3-H b, skel def (A)
ν_{27}	1276,0 w	1276,0 vs	1280,1	14,75	C3-H b, C-H b, C=C s
ν_{28}	1239,0 m	1239,0 m	1232,4	54,93	C3-H b, C-H b, C-C s
ν_{29}			1206,4	1,28	C-CH$_3$ s, skel def (A)
ν_{30}	1179,0 m	1179,9 m	1172,1	41,24	C3-H b, C-H b, skel def
ν_{31}			1166,0	56,67	C-H b (A), skel def
ν_{32}			1106,5	6,82	C-H b (A)
ν_{33}	1033,2 w	1033,2 w	1024,2	5,85	skel oop def, CH$_3$ b
ν_{34}	1017,6 w	1014,5 w	1017,7	31,60	S-H b (δ_{SH}), C-H b (A)
ν_{35}			1001,9	5,11	skel oop def, CH$_3$ b
ν_{36}			1000,3	9,50	Skel def (A), C-H b (A), S-H b
ν_{37}			972,6	2,63	skel def, CH$_3$ b
ν_{38}			963,6	0,48	C-H oop b (asym)
ν_{39}	959,8 m	958,9 m	954,6	4,22	C-H oop b, S-H b
ν_{40}	944,5 w	944,5 w	942,1	8,32	S-H b, skel def
ν_{41}			934,6	32,53	CH$_3$ b, C3-H b
ν_{42}			847,3	1,85	Skel def (A), S-H b
ν_{43}			835,9	1,40	C-H oop b (A)
ν_{44}	832,5 w	832,5 vs	829,8	3,38	C3-H oop b (γ_{CH}), C-H oop b (A)
ν_{45}	807,2 m	805,7 s	807,4	28,79	C3-H oop b (γ_{CH}), C-H oop b (A)
ν_{46}	780,7 w	781,3 w	772,2	4,24	skel def (A)
ν_{47}	718,7 w	717,4 vs	717,8	1,68	skel def oop (A)
ν_{48}	688,2 w	686,8 w	672,6	9,33	skel def

ν_{49}	641,4	641,4	635,4	3,22	skel def (A)
ν_{50}			617,3	0,62	Skel oop def
ν_{51}	599,7 w	599,8 m	589,2	18,30	skel def
ν_{52}	571,2 w	571,0 w	568,4	3,18	skel oop def
ν_{53}	514,0 w		512,9	11,30	skel def
ν_{54}	480,0 w	477,0 w	476,7	16,28	skel def
ν_{55}			454,2	5,34	S-H oop b
ν_{56}			407,1	0,49	Skel oop def (A)
ν_{57}			378,0	6,81	Skel def
ν_{58}			338,5	0,83	CH_3 b, skel def
ν_{59}			313,9	1,38	CH_3 b, skel def
ν_{60}			248,6	0,03	Skel oop def
ν_{61}			239,7	1,67	Skel def
ν_{62}			194,7	2,66	Skel oop def
ν_{63}			157,8	3,84	Skel def
ν_{64}			109,3	0,49	CH_3 tor
ν_{65}			101,5	0,86	Skel def, CH_3 tor
ν_{66}			80,4	3,85	Skel def, CH_3 tor
ν_{67}			63,4	0,39	Skel def
ν_{68}			50,8	0,79	Skel def
ν_{69}			35,8	0,42	CH_3 tor

[a]A – corresponding to the thiobenzoyl ring.

Table 5.14. Vibrational assignments for the enol form of **11**.

	Exp.		Calc.		
	$\tilde{\nu}$ (cm^{-1})		$\tilde{\nu}$ (cm^{-1})	I (km/mol)	Approximate mode description
	Ar	Xe			
ν_1			3151,2	3,79	CH s
ν_2			3147,3	2,39	CH s
ν_3			3129,8	6,16	CH s
ν_4			3128,8	4,99	CH s
ν_5	3110 w		3121,9	14,21	CH s
ν_6	3091 m		3119,0	28,61	CH s
ν_7	3072 m		3114,2	20,41	CH s
ν_8			3108,3	9,26	CH s
ν_9			3103,4	7,46	CH s
ν_{10}			3097,6	0,81	CH s
ν_{11}			3093,7	0,7	CH s
ν_{12}	2600 w		2585,7	530,78	OH s
ν_{13}			1610,7	8,53	skel def (B)
ν_{14}	1605 w	1604 w	1605,8	2,56	skel def (A)
ν_{15}	1593 m	1590 m	1594,1	112,42	C=C s, OH b
ν_{16}			1582,4	0,9	skel def
ν_{17}	1561 vs	1558 s	1561,0	754,47	C=C s, OH b
ν_{18}	1495 m	1492 m	1484,0	29,22	skel def (B)
ν_{19}			1479,1	18,99	skel def (A)
ν_{20}	1465 m	1463 m	1459,6	146,46	C-O s, C-C s
ν_{21}			1435,2	8,86	skel def (A,B)
ν_{22}			1422,5	62,1	OH b, CH b
ν_{23}	1420 w	1420 vw	1403,0	88,93	OH b, C-O s, CC s
ν_{24}			1329,9	5,83	"Kekule" (B)
ν_{25}	1314 w		1325,0	5,01	"Kekule" (A)
ν_{26}	1293 w	1295 w	1299,7	62,2	CH b, skel def
ν_{27}			1294,8	2,91	CH b (B), skel def
ν_{28}	1274 w	1274 w	1267,5	56,34	CC s
ν_{29}	1239 w	1243 w	1242,1	197,2	C-C s, CH b
ν_{30}	1205 w	1202 vw	1204,1	27,25	C-C(A), C-C(B) s
ν_{31}			1092,0	5,83	CH b (B)
ν_{32}	1183 w	1184 vw	1164,1	16,62	CH b (A)
ν_{33}			1144,6	1,28	CH b (B)
ν_{34}			1142,7	0,09	CH b (A)
ν_{35}	1098 w		1083,2	20,8	skel def, C-O s
ν_{36}			1075,4	9,73	skel def
ν_{37}	1087 w		1066,6	20,41	C-O s, skel def
ν_{38}	1030 w		1026,7	3,48	skel def
ν_{39}			1025,7	4,2	skel def
ν_{40}			994,5	0,23	CH oop wag (B)
ν_{41}			988,6	0,5	skel def (A,B)
ν_{42}			987,7	4,11	CC b (B)
ν_{43}			986,7	1,28	CC b (A)
ν_{44}			970,1	0,31	CH oop wag (B)
ν_{45}			966,2	3,83	CH oop wag (A)
ν_{46}	955 w		946,7	25,73	skel def, C=S s
ν_{47}			930,1	0,6	CH oop wag (B)
ν_{48}	926 w		923,3	2,74	CH oop wag (A)
ν_{49}	845 w	840 w	852,1	35,07	OH oop wag (gOH)

v_{50}			839,5	2,45	CH oop wag
v_{51}			838,5	3,24	skel def
v_{52}	823 w	819 w	829,7	6,4	skel def
v_{53}			816,1	5,37	CH oop wag
v_{54}	779 m	779 w	780,0	11,95	CH oop wag (A;B)
v_{55}	763 m	763 m	761,5	55,14	CH oop wag (A)
v_{56}	738 w	738 w	727,4	9,97	skel def, C=S s
v_{57}	694 w	697 w	691,3	19,53	CH oop wag (A)
v_{58}	685 w	681 vw	685,4	31,18	CH oop wag (B)
v_{59}			679,6	0,39	skel def
v_{60}	665 w	666 vw	663,0	6,77	skel def (A,B)
v_{61}	616 w		618,1	1,53	skel def (A)
v_{62}			613,3	1,07	skel def (B)
v_{63}			609,4	0,3	skel def (A)
v_{64}	561 w		565,5	24,5	skel def
v_{65}			479,7	15,3	skel def
v_{66}			466,1	2,39	S..H-O s
v_{67}			441,7	6,27	skel def
v_{68}			404,6	0,99	skel oop def (A)
v_{69}			400,7	0	skel oop def (B)
v_{70}			373,4	3,88	C-O b, C=S s
v_{71}			323,7	0,14	skel def
v_{72}			261,3	2,24	C=S b
v_{73}			241,8	0,29	C=S b
v_{74}			237,9	1,86	skel def
v_{75}			180,4	0,05	C-O, C=S oop wag
v_{76}			155,0	0,28	skel def
v_{77}			86,8	0,46	C-O oop wag
v_{78}			76,0	0,22	C=S, C-O oop wag
v_{79}			64,3	0,32	skel def
v_{80}			37,0	0,29	C-C(A) tor
v_{81}			17,6	0,18	C-C(B) tor

[a]B – corresponding to the benzoyl ring; [b]A – corresponding to the thiobenzoyl ring.

Table 5.15.   Vibrational assignments for the enethiol form of 11.

	Exp.		Calc.		
	$\tilde{\nu}$ (cm^{-1})		$\tilde{\nu}$ (cm^{-1})	I (km/mol)	Approximate mode description
	Ar	Xe			
ν_1			3139,5	6,2	CH s
ν_2			3134,6	8,06	CH s
ν_3			3124,9	9,6	CH s
ν_4			3123,9	6,57	CH s
ν_5	3093 w		3119,0	17,68	CH s
ν_6	3067 m		3115,1	29,21	CH s
ν_7	3041 m		3112,2	11,17	CH s
ν_8	2983 m		3103,4	10,85	CH s
ν_9			3103,4	4,24	CH s
ν_{10}	3093 w		3095,6	0,99	CH s
ν_{11}			3093,7	0,47	CH s
ν_{12}	2550 w		2548,7	33,2	SH s
ν_{13}	1645 vs	1642 vs	1657,5	119,21	C=O s, C=C s
ν_{14}	1602 m	1604 m	1609,7	30,56	CC s (B)^a, CH b (B)
ν_{15}			1607,8	0,52	CC s (A)^b, CH b (A)
ν_{16}	1583 m	1581 w	1587,3	37,59	skel def (CC s)
ν_{17}			1583,4	5,71	skel def (CC s)
ν_{18}	1546 vs	1543 m	1548,3	441,42	C=C s, C-C s, CH b
ν_{19}			1482,0	6,54	skel def, CH b
ν_{20}	1492 m		1477,1	39,99	skel def, CH b
ν_{21}	1452 m	1450 w	1437,1	11,55	skel def
ν_{22}			1432,3	4,74	skel def (A)
ν_{23}	1345 m	1344 w	1332,8	71,8	Kekulé" (B), CH b
ν_{24}	1338 m		1329,9	36,69	CH b, "Kekulé" (B)
ν_{25}	1310 w		1319,2	13,86	"Kekulé" (A), CH b
ν_{26}			1290,9	1,34	CH b (A,B)
ν_{27}	1280 w		1281,1	40,67	CH b (A,B)
ν_{28}	1258 s	1252 w	1239,2	179,61	C-C s, CH b
ν_{29}	1217 m	1214 w	1200,2	71,18	C-C(A) s, C-C(B) s
ν_{30}			1164,1	0,47	CH b (A)
ν_{31}	1183 w	1181 vw	1162,2	33,95	CH b (B)
ν_{32}			1142,7	0,02	CH b (A)
ν_{33}	1160 vw		1141,7	3,1	CH b (B)
ν_{34}	1098 w		1077,4	3,62	CH b (B)
ν_{35}	1073 w		1072,5	5,24	CH b (A)
ν_{36}	1052 m	1048 w	1042,3	51,12	CH b (B), SH b
ν_{37}			1027,6	3,84	CH b (A)
ν_{38}	1027 w		1020,8	20,5	CH b (B)
ν_{39}	1002 w		1007,2	18,4	SH b
ν_{40}			999,4	0,28	CH oop wag (B)
ν_{41}			988,6	4,66	CC b (B)
ν_{42}			987,7	0,13	CH oop wag (A)
ν_{43}			986,7	3,08	CC b (A)
ν_{44}			975,0	0,17	CH oop wag (B)
ν_{45}			966,2	1,24	CH oop wag (A)
ν_{46}			932,1	0,49	CH oop wag (B)
ν_{47}	932 w		923,3	3,15	CH oop wag (A), SH b
ν_{48}	919 w		911,6	15,85	SH b, CH oop wag (A)
ν_{49}			844,4	0,81	CH oop wag (B)
ν_{50}			841,4	1,11	CH oop wag (A)
ν_{51}	839 w	836 vw	834,6	5,91	CH oop wag (B)

ν_{52}	819 w		807,3	3,03	skel def
ν_{53}	785 w		786,8	10,38	CH oop wag (B)
ν_{54}	760 m	759 w	759,5	39,5	CH oop wag (A)
ν_{55}	701 m	697 w	698,1	17,12	CH oop wag (A)
ν_{56}	693 m		697,1	35,84	CH oop wag (B)
ν_{57}			689,3	12,13	CH oop wag (B)
ν_{58}	673 m	668 w	681,5	7,38	skel def
ν_{59}			665,9	20,98	skel def (A,B)
ν_{60}	613 w		616,2	1,55	skel def (A)
ν_{61}			613,3	0,99	skel def (B)
ν_{62}	590 w		589,9	3,9	skel def
ν_{63}	565 w	563 w	559,6	26,82	skel def, SH b
ν_{64}			492,4	15,42	SH oop wag, skel def
ν_{65}			462,1	4,37	SH oop wag, skel def
ν_{66}			452,4	3,54	SH oop wag, skel def
ν_{67}			435,8	2,04	SH oop wag, skel def
ν_{68}			404,6	0,49	skel oop def (A)
ν_{69}			403,6	0,06	skel oop def (B)
ν_{70}			344,2	12,78	skel def, C=O wag
ν_{71}			300,3	5,02	skel def, C=O wag
ν_{72}			249,6	0,13	skel def
ν_{73}			235,0	0,54	skel def
ν_{74}			196,9	3,62	CCS b, skel def
ν_{75}			169,7	0,58	A,B oop def
ν_{76}			143,3	1,12	skel def (A,B rock?)
ν_{77}			94,6	1,09	skel def, C=O oop wag
ν_{78}			69,2	0,72	skel def, SH oop wag
ν_{79}			56,5	0,4	skel def
ν_{80}			33,1	0,79	C-C(A) tor
ν_{81}			18,5	0,01	C-C(B) tor

[a]B – corresponding to the benzoyl ring; [b]A – corresponding to the thiobenzoyl ring.

5.3 Conclusions

The combination of the results of experimental IR and electronic spectral studies, and the theoretically predicted spectra allows us to conclude that the product of photoinduced transformation in all the investigated β-thioxoketones corresponds to the -SH exo-rotameric (Z)-enethiolic tautomer (form (c) in Chart 5.2). These conclusions are in a good agreement with the results of matrix isolation studies of malonaldehyde and acetylacetone,[87] which also suggested the open form as the structure of the photoisomerization product. Excellent agreement was obtained between the calculated vibrational pattern in the harmonic field assumption and the experimental spectra of the photoproduct. The use of anharmonic field assumption allows obtaining a good theoretical prediction of the vibrational pattern even in the more complicated case of the (Z)-enol form, a structure with a strong hydrogen bonding. Thus, the computational chemistry is now able to serve as a valuable tool for the assignment of photoreaction products in relatively large molecules. We are currently testing the applicability of the TD-DFT approach in the investigation of the possible excited-state pathways in photoconversion phenomena in β-thioxoketones.

The polarized spectroscopy studies in cooperation with the vibrational assignments were an independent method which confirmed the previously obtained assignment of structures of the initial and the final form of the photoreaction for all β-thioxoketones. LD measurements allowed us to characterize the directions of the moments of the two lowest singlet transitions for one of the β-thioxoketones within the molecular framework. This allows us to propose that the methodology described above can be successively used as a separate method for the structure elucidation, on one hand, and for spectral assignments, on the other.

Chapter 6. Dynamics of double hydrogen transfer in corrphycene, a porphyrin isomer

6.1. Introduction

Porphyrin and its derivatives are well known due to their importance in biology and medicine, as it was mentioned above, and wide-spread in other various areas of daily life. The results of the investigations of the electronic structure of excited states of corrphycene and hemiporphycene, two constitutional isomers of porphyrin, were presented in the previous part of the current work. This part is dedicated to understanding another exciting property - dynamics of double hydrogen transfer (DHT). Porphyrin and its analogues (see Chart 6.1) are macrocyclic compounds with intra-molecular hydrogen bonds. DHT between inner nitrogen atoms is characteristic for such species. This process occurs both in the ground state (in the dark), and in excited states (upon light irradiation), and differs from a classical reaction in that in porphyrin-like compounds the product and the substrate are chemically identical.
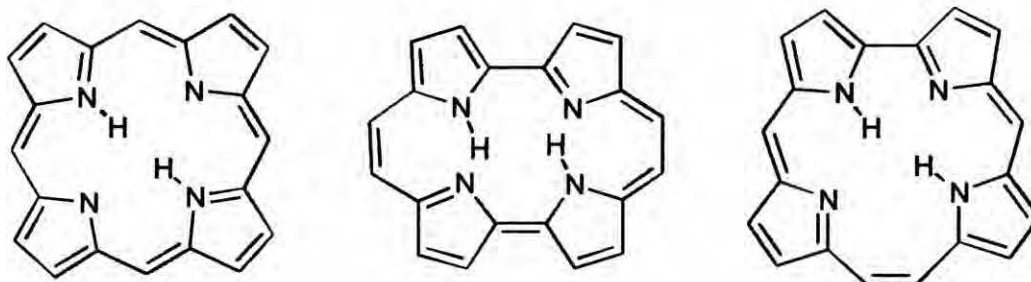
Chart 6.1.   Left to right: porphyrin, porphycene and corrphycene (2).

The rate constant of thermally activated DHT reaction in the ground state of porphyrin is estimated to be higher than 10^4 s^{-1} at room temperature.[88] This dark reaction can be stopped at temperatures below 100 K. On the contrary, the photoinduced reaction in the excited state occurs even at liquid helium temperatures.[89] The former and latter reactions have been investigated for a long time, but some questions are still open:

1. The dominant tautomeric species in porphyrin is a *trans* form, where the inner hydrogens are located at the opposite nitrogen atoms. In such form, phototransformation leads to pseudo-rotation of the molecule (the angle between the dipole moment transitions changes by 90^0). However, the presence of *cis* tautomers (inner hydrogens located at neighboring nitrogen atoms) was also postulated.[90-91]

2. The role of tunneling vs. thermally activated process in the photo-induced reaction remains to be elucidated.

3. The fashion of hydrogen movement during DHT, asynchronous or simultaneous, has long been a subject of discussion. It is now established that in the ground state the hydrogens move in a stepwise manner. The mechanism of the process in the excited singlet and triplet states is still not clear.

The analogues of porphyrin: porphycene[92], corrphycene[93] and hemiporphycene[15-16] were synthesized recently. These molecules differ from each other in the size of the inner nitrogen atoms cavity, have a lower symmetry than porphyrin and may thus be helpful in understanding the mechanism of phototautomerization.

Since, the photoreaction transforms porphyrin-like molecules into themselves, special methods are required for the investigation of this process. The methods of isolating molecules in rigid media at low temperatures are often used for these investigations, combined with the methods of polarized spectroscopy, for instance, anisotropy of fluorescence or LD studies. The main requirement for these methods is the ability to detect the two tautomers after photoreaction. The rare gas[8, 94] or a Shpolskii matrix[95] can break the symmetry of guest molecules depending on the matrix structure and the type of molecular embedding into the host crystal. The tautomers of guest molecules will differ from each other in the orientation, when the photoorientation of the sample is achieved by using polarized light. Such partially aligned samples can be studied by LD measurement.[85] This case is characteristic for a "slow"

DHT, when the dark process in ground state is frozen and stationary experiments are possible. In the case of "fast" DHT, when the dark process occurs rapidly, time-resolved techniques allow to investigate reactions in both the ground and the excited states. If the fluorescence lifetime of tautomers (usually ~10 ns) is shorter or comparable than the time of DHT, the time-resolved emission anisotropy measurement allows obtaining the rate constants of the reaction and characterize the dynamics of the process. The rate k_{PT} can also be determined from stationary anisotropy measurements, using the formula:[96]

$$k_{PT} = \frac{1}{\tau_{fl}}\left(\frac{r_0 - r}{2r - r(2\alpha) - r_0}\right) \qquad (6.1)$$

where r is the measured value of anisotropy, τ_{fl} is a lifetime of the S_1 state obtained at the same temperature as anisotropy r, r_0 is a limiting value of anisotropy (without depolarization due to DHT), 2α is an angle between the transition dipole moments of the lowest singlet electronic states of the two phototautomers (the angle of pseudorotation of the molecule in the process of phototautomerization).

6.2. Tautomerization in corrphycene

The measurement of anisotropy of emission for tetraphenylporphyrin revealed fluorescence that is not depolarized even at 293 K.[97] Therefore, the rate of the process in the S_1 state at room temperature should be slower than 10^7 s^{-1}, which can be estimated based on the S_1 lifetime (~15 ns). On the contrary, fluorescence of the octaethyl derivative of corrphycene under the same conditions is depolarized (Figure 6.1). Therefore, the rate is faster than 10^8 s^{-1}. Since the depolarization is only possible for *trans* tautomers (phototransformation in a *cis* structure would not lead to rotation of the dipole moment transitions) the possibility of the *cis* tautomer being the dominant structure can be rejected.

In addition to estimating the rate of the photoreaction, measurements of emission anisotropy allow to determine the angles between the direction of different transition dipole

moments and, in comparison with the theoretical calculation, can lead to the assignment of the transition dipole moments within the molecular framework. In the simplest case, the anisotropy of emission can be written as:[98]

$$r(\varphi) = [3\cos^2(\varphi) - 1]/5 \qquad\qquad (6.2)$$

where φ is angle between the directions of transition dipole moments in emission and excitation. The anisotropy of fluorescence excitation obtained for **2** at different temperatures in poly (vinyl butyral) (PVB) sheet and EPA (ethyl ether: isopentane: ethanol - 5:5:2) solution is presented in Figure 6.1. As is clearly seen, anisotropy measured at 77 K is still depolarized. On the other hand, the experiment at 60 K reveals an increase in the absolute values of anisotropy. Decreasing the temperature further to 25 K does not lead to any changes. The behavior of anisotropy at low temperatures allows us to propose that the process of phototautomerization in the S_1 state becomes frozen at temperatures in the region 77 - 60 K. The values of the angles between the S_1 transition dipole moment and transition dipole moments of higher excited states were estimated from non-depolarized anisotropy and are presented in Table 6.1 and Figure 6.1. These values reveal good accordance with the theoretical predictions. The values of the angles for two close-lying transitions at higher energy are somewhat lower than predicted by theory, which can be explained by strong overlapping of these transitions. As a result, the apparent anisotropy becomes lower for the state with real higher value. The opposite occurs for the anisotropy for the state with lower values.

Theory   Experiment
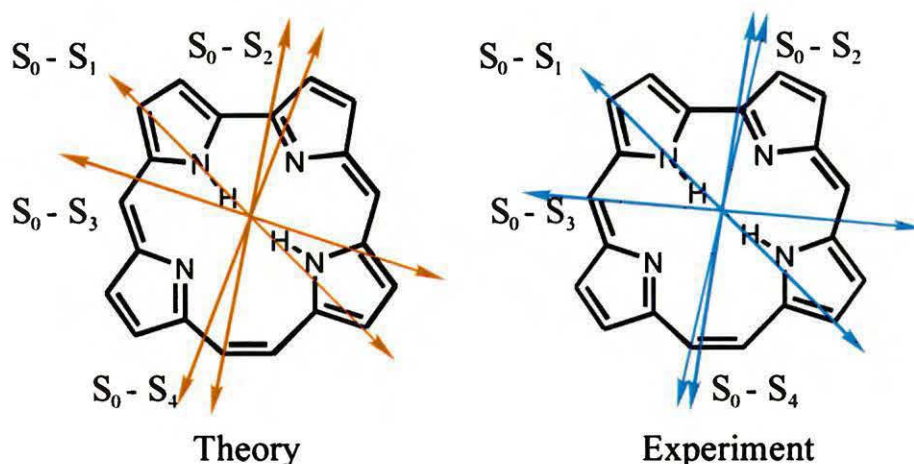
Figure 6.1. The calculated (left) and experimentally obtained (right) angles between the direction of the first transition dipole moment and the directions of transition dipole moments of higher excited states. The experimental dipole moments were drawn under assumption that first dipole moment has the same direction as the calculated one.

Table 6.1. Calculated (TD-B3LYP/6-31G**) electronic states and angles between the direction of the first excited state transition dipole moment and the directions of transition dipole moments of higher excited states of **2** in comparison with the values determined from the anisotropy of emission (**r**) and the transition energies obtained for the octaethyl derivative in poly (vinyl butyral) at 25 K.

	Calc. Energy[a] [10^3 cm^{-1}]	Oscillator strength	α[b] deg	r	β[c] deg	Exp. Energy[d] [10^3 cm^{-1}]
1	18.7	0.001		~0.30		15.8
2	19.7	0.001	57	-0.03	58	17.2
3	26.3	0.293	27	0.00	40	23.3
4	28.1	0.684	66	0.15	54	24.2

[a]calculated for the unsubstituted molecule; [b]theoretically and [c]experimentally obtained angles between the direction of the first transition dipole moment and the directions of transition dipole moments of higher excited states; [d]experimental results for **2** in PVB sheet at 25 K.

The rate of phototransformation can be calculated using the equation 6.1, but the value of anisotropy obtained for the $S_1 \leftarrow S_0$ transition is not precise, see Figure 6.2. As was mentioned above in part 4.1 the electronic structure and the spectral behavior of corrphycene are similar to those of porphyrin and the $S_1 \leftarrow S_0$ transition in **2** is nearly forbidden. This is why a precise measurement of the anisotropy in this region should be done at concentration of molecules higher than used so far. However, for such case, a possible depolarization of anisotropy at high concentrations due to the energy transfer can be a problem. Therefore, additional accurate experiments in the 0-0 region of $S_1 \leftarrow S_0$ transition are required which is considered for future investigations.
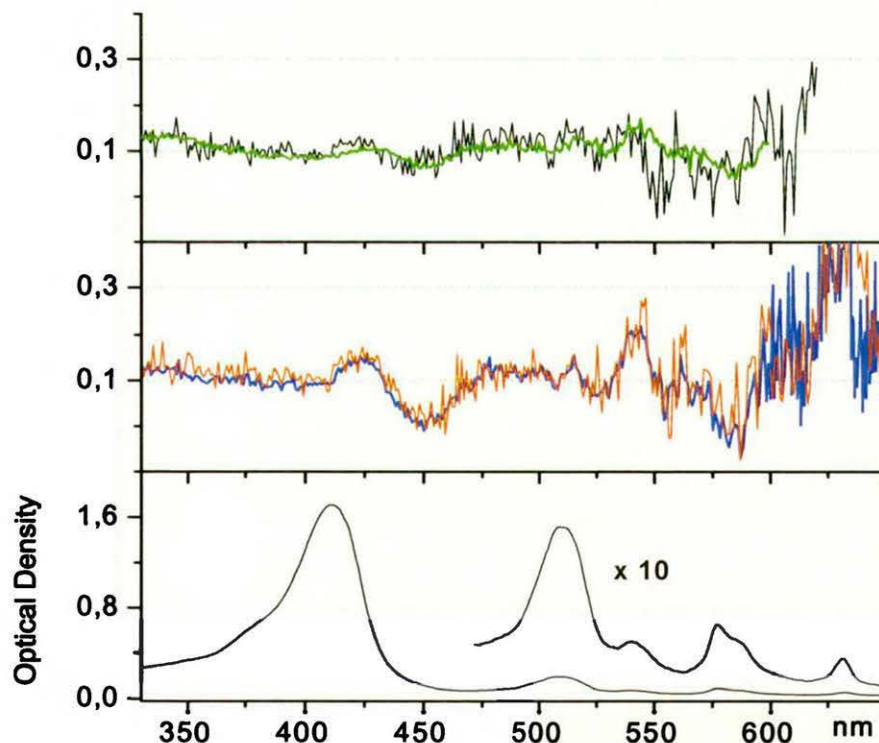
Figure 6.2.   Anisotropy of fluorescence excitation monitored at 635 nm for the octaethyl derivative of **2**: in PVB at 298 (green), 60 (red) and 25 (blue) K; in EPA at 77 (black) K. Bottom, absorption in EPA at 298 K.

6.3. Conclusions

The double hydrogen transfer was investigated in the lowest excited singlet state of corrphycene using methods of polarized spectroscopy from room to low temperatures. The process of DHT in the first excited state of **2** can be stopped at temperatures between 60 – 77 K. Good accordance between calculated and estimated experimentally directions of dipole moment transitions can be an additional proof that mostly *trans* tautomers of **2** are present. Thus, *cis* structures are not dominant or present at all.

The methods of polarized spectroscopy allow the investigation of the dynamics of hydrogen transfer in such special species as porphyrin-like molecules, where DHT corresponds to the rotation of molecule which is being chemically transformed into itself. These techniques can be extended to the studies of any rapid photochemical processes which involve structural changes of species and, in consequence, changes in the direction of the transition dipole moments of the product in comparison with the substrate. The used methodology provides not only information about the rate of the photoprocess, but also data about the structural and spectroscopic changes which accompany the phototransformation.

Chapter 7. Summary and future work

The methods of polarized spectroscopy: magnetic circular dichroism (MCD), linear dichroism (LD), and anisotropy of fluorescence were applied for the investigations of organic molecules belonging to different classes of aromatic compounds and photochromic β-thioxoketones. The described methodologies were based on a cooperative use of the polarized spectroscopy studies and theoretical calculations and were successively used as methods for the investigations of the spectroscopic properties of molecules and, in the following, structure elucidation.

1.   The power of the MCD spectroscopy combined with predictions and interpretation of the spectra based on a simple perimeter model was demonstrated for seven different organic compounds, varying in size and symmetry of the π-system.

Both experiment and theory reveal a soft character of the corrphycene chromophore and its spectral consequences, which place this molecule very close to porphyrin, and far from the negative-hard chromophores: porphycene or hemiporphycene.

The approximate equality of orbital splittings in corrphycene can be easily destroyed by structural perturbations, such as, e.g., substitution. The sign of the resulting ΔHOMO - ΔLUMO difference, should be strongly position-dependent. That could make MCD spectroscopy an attractive tool for further studies of corrphycene derivatives.

The negative-hard character of the hemiporphycene and isosmaragdyrin chromophores implies a relatively strong absorption in the visible region and thus predicts possible applications of these particular systems as sensitizers, e.g. in photodynamic therapy. On the other hand, some other conditions are required for a successful use in this particular application area, namely high yield of the triplet state and singlet oxygen formation, and photochemical stability. Unfortunately, a low stability of the neutral forms of

isosmaragdyrins precludes using these compounds in such an exciting area as photodynamic therapy. Nevertheless, the species that were investigated here by simple theoretical analyses could provide a starting point for the design of new substances with expected spectral and photochemical properties.

The cyclo[n]pyrroles exhibit perfect examples of molecules of high-symmetry. The application of the perimeter model leads to the prediction of two degenerate electronic transitions of comparable intensity for these species. Both transitions should exhibit a negative A terms, whereas the B terms should be positive for the L transition, and negative for the B transition. All these predictions are fully confirmed by experiment. The patterns expected for a planar chromophore are not changed even when the deviations from planarity are considered.

Thus, the MCD spectroscopy can be successfully used as a tool for systematization of aromatic compounds, with the crucial role played by their ΔHOMO - ΔLUMO splitting. The analysis of this splitting allows both to describe the electronic properties of molecules and to predict changes of these properties upon chemical or photophysical influences. In addition, basing on the perimeter model, it is possible to design various derivatives and isomers of the investigated molecules with well-defined properties obtained by appropriate changes in substitution. For example, the strong negative-hard character, and, in consequence, intense absorption bands in the visible region, should be expected for porphyrin-(2.2.0.0) and porphyrin-(4.0.0.0), as well as for the pentapyrrolic system, pentaphyrin-(0.0.0.0.0). These molecules remain yet to be synthesized and investigated.

2. The results of experimental IR and electronic spectral studies, along with the spectral patterns predicted by DFT calculations clearly demonstrate that the product of photoinduced transformation in all the investigated β-thioxoketones corresponds to the -SH exo-rotameric (Z)-enethiolic tautomer. This assignment was independently confirmed by

polarized spectroscopy studies in cooperation with the vibrational assignments. In addition, LD measurements allowed us to characterize the directions of the moments of the two lowest singlet electronic transitions for one of the β-thioxoketones within the molecular framework.

Further investigations of β-thioxoketones will be dedicated to the elucidation of the possible excited-state pathways in photoconversion phenomena in this class of photochromic molecules.

3.   Double hydrogen transfer (DHT) was detected and studied in the lowest excited singlet state of octaethylcorrphycene, a constitutional isomer of porphyrin. Since DHT corresponds to the rotation of the molecule, which is being chemically transformed into itself, it could be successfully investigated using methods of anisotropy of fluorescence in a wide range of temperatures. The process of DHT in the first excited state of corrphycene can be stopped at temperatures between 60 – 77 K. The agreement between calculated and experimentally estimated directions of dipole moment transitions provided an additional proof that mostly *trans* tautomers of corrphycene are present, while *cis* structures are not dominant or present at all.

The described techniques can be adapted to the studies of various photochemical and photophysical processes that involve structural changes or changes in the orientation of species and, in consequence, changes in the direction of the transition dipole moments of the product in comparison with the substrate. Polarized spectroscopy studies provide not only information about the rate of the photoprocess, but also reveal details about the structural and spectroscopic changes which accompany the phototransformation.

Further investigations of the dynamics and the mechanism of DHT in porphyrin-like molecules are planned for both singlet and the triplet excited states, as well as in the ground state. The methodologies of polarized spectroscopy which have been used before should

become even more fruitful when combined with theoretical quantum-dynamic calculations and the experiments of the time-resolved spectroscopy. The latter can, for instance, allow describing an influence of particular vibrations in porphyrin-like molecules on a photochemical process, such as DHT.

References

1. Thulstrup, E. W.; Michl, J.; Eggers, J. H., *J. Phys. Chem.* **1970**, *74*, 3868.

2. Platt, J. R., *J. Chem. Phys.* **1949**, *17*, 484.

3. Moffitt, W., *J. Chem. Phys.* **1954**, *22*, 320.

4. Gouterman, M., *J. Mol. Spectrosc.* **1961**, *6*, 138.

5. Michl, J., *J. Am. Chem. Soc.* **1978**, *100*, 6801.

6. Waluk, J.; Müller, M.; Swiderek, P.; Köcher, M.; Vogel, E.; Hohlneicher, G.; Michl, J., *J. Am. Chem. Soc.* **1991**, *113*, 5511.

7. Whittle, E.; Dows, D. A.; Pimentel, G. C., *J. Chem. Phys.* **1954**, *22*, 1943.

8. Kyrychenko, A.; Waluk, J., *J. Chem. Phys.* **2003**, *119*, 7318.

9. Bajema, L.; Gouterman, M.; Meyer, B., *J. Mol. Spectrosc.* **1968**, *27*, 225.

10. Bajema, L.; Gouterman, M.; Rose, C. B., *J. Mol. Spectrosc.* **1971**, *39*, 421.

11. Cook, G. A., *Argon, Helium and The Rare Gases*. Interscience (Wiley): New York, **1961**; Vol. 1,2.

12. Pollak, G. L., *Rev. Mod. Phys.* **1964**, *36*, 748.

13. Bolz, L. A.; Broida, H. P.; Peiser, H. S., *Acta Cryst.* **1962**, *15*, 810.

14. Schnepp, O.; Dressler, K., *J. Chem. Phys.* **1960**, *33*, 49.

15. Vogel, E.; Bröring, M.; Weghorn, S. J.; Scholz, P.; Deponte, R.; Lex, J.; Schmickler, H.; Schaffner, K.; Braslavsky, S. E.; Müller, M.; Pörting, S.; Fowler, C. J.; Sessler, J. L., *Angew. Chem. Int. Ed. Engl.* **1997**, *36*, 1651.

16. Callot, H. J.; Rohrer, A.; Tschamber, T.; Metz, B., *New. J. Chem.* **1995**, *19*, 155.

17. Sessler, J. L.; Davis, J., M.; Lynch, V. J., *Org. Chem.* **1998**, *63*, 7062.

18. Köhler, T.; Seidel, D.; Lynch, V.; Arp, F. O.; Ou, Z.; Kadish, K. M.; Sessler, J. L., *J. Am. Chem. Soc.* **2003**, *125*, 6872.

19. Duus, F.; Anthonsen, J., *Acta Chem. Scand., Ser. B* **1977**, *31*, 40.

20. Duus, F., *J. Org. Chem.* **1977**, *42*, 3123.

21. Jasny, J.; Waluk, J., *Rev. Sci. Instrum.* **1998**, *99*, 2242.

22. Velapoldi, R. A., *Natl. Bur. Stand.* **1972**, *378*, 231.

23. Jasny, J.; Sepioł, J.; Karpiuk, J.; Gilewski, J., *Rev. Sci. Instrum.* **1994**, *65*, 3646.

24. Holmquist, B., *Methods in Enzymology* **1986**, *130*, 270.

25. Becke, A. D., *J. Chem. Phys.* **1993**, *98*, 5648.

26. Lee, C.; Yang, W.; Parr, R. G., *Phys. Rev.* **1988**, *37B*, 785.

27. Jensen, F., *Introduction to Computation Chemistry*. Wiley: Chichester, **1999**.

28. Koch, W.; Holthausen, M. C., *A Chemist's Guide to Density Functional Theory*. Wiley-VCH: Weinheim, Germany, **2000**.

29. *Gaussian 98*, M. J. Frisch et al.: Pittsburgh, PA, **1998**.

30. *Gaussian 03, Revision B.03*, M. J. Frisch et al.: Pittsburgh, PA, **2003**.

31. Ridley, J. E.; Zerner, M. Z., *Theor. Chim. Acta* **1973**, *32*, 111.

32. Dewar, M. J. S.; Zoeblisch, E. G.; Healy, E. F.; Stewart, J. J. P., *J. Am. Chem. Soc.* **1985**, *107*, 3902.

33. Gust, D.; Moore, T. A.; Moore, A. L.; Lee, S.-J.; Bittersmann, E.; Luttrull, D. K.; Rehms, A. A.; DeGraziano, J. M.; Ma, X. C.; Gao, F.; Belford, R. E.; Trier, T. T., *Science* **1990**, *248*, 199.

34. Imahori, H.; Arimura, M.; Hanada, T.; Nishimura, Y.; Yamazaki, I.; Sakata, Y.; Fukuzumi, S., *J. Am. Chem. Soc.* **2001**, *123*, 335.

35. Deviprasad, G. R.; D'Souza, F., *Chem. Commun.* **2000**, 1915.

36. Wagner, R. W.; Lindsey, J. S.; Seth, J.; Palaniappan, V.; Bocian, D. F., *J. Am. Chem. Soc.* **1996**, *118*, 3966.

37. Reddy, D. R.; Maiya, B. G., *Chem. Commun.* **2001**, 117.

38. Drobizhev, M.; Sigel, C.; Rebane, A. J., *Luminescence* **2000**, *86*, 391.

39. Collman, J. P.; McDevitt, J. T.; Yee, G. T.; Leidner, C. R.; McCullough, L. G.; Little, W. A.; Torrance, J. B., *Proc. Natl. Acad. Sci.* **1986**, *83*, 4581.

40. Bonnet, R., *Chem. Soc. Rev.* **1995**, 19.

41. Abels, C.; Szeimies, R.-M.; Steinbach, P.; Richert, C.; Goetz, A. E., *J. Photochem. Photobiol. B* **1997**, *40*, 305.

42. Waluk, J.; Michl, J., *J. Org. Chem.* **1991**, *56*, 2729.

43. Michl, J., *J. Am. Chem. Soc.* **1978,** *100,* 6819.

44. Michl, J., *Tetrahedron* **1984,** *40,* 3845.

45. Keegan, J. D.; Stolzenberg, A. M.; Lu, Y.-C.; Linder, R. E.; Barth, G.; Bunnenberg, E.; Djerassi, C.; Moscowitz, A., *J. Am. Chem. Soc.* **1981,** *103,* 3201.

46. Borowicz, P.; Gil, M.; Dobkowski, J.; Vogel, E.; Waluk, J., *unpublished results.*

47. Bremm, D.; Hohlneicher, G., *J. Mol. Struct.* **1999,** *591,* 480.

48. Djerassi, C.; Lu, Y.; Waleh, A.; Shu, A. Y. L.; Goldbeck, R. A.; Kehres, L. A.; Crandell, C. W.; Wee, A. G. H.; Knierzinger, A.; Gaete-Holmes, R.; Loew, G. H.; Clezy, P. S.; Bunneberg, E., *J. Am. Chem. Soc.* **1984,** *106,* 4241.

49. Gouterman, M.; Wagniere, G. H.; Snyder, L. C., *J. Mol. Spectrosc.* **1963,** *11,* 108.

50. Dobkowski, J.; Galievsky, V.; Starukhin, A.; Vogel, E.; Waluk, J., *J. Phys. Chem. A* **1998,** *102,* 4996.

51. Hasegawa, J.; Ozeki, Y.; Ohkawa, K.; Hada, M.; Nakatsuji, H., *J. Phys. Chem. B* **1998,** *102,* 1320.

52. Sundholm, D., *Chem. Phys. Lett.* **2000,** *317,* 392.

53. Keegan, J. D.; Stolzenberg, A. M.; Lu, Y. C.; Linder, R. E.; Barth, G.; Moscowitz, A.; Bunnenberg, E.; Djerassi, C. J., *J. Am. Chem. Soc.* **1982,** *104,* 4317.

54. Lament, B.; Dobkowski, J.; Sessler, J. L.; Weghorn, S. J.; Waluk, J., *Chem. Eur. J.* **1999,** *10,* 3039.

55. Lament, B.; Karpiuk, J.; Waluk, *Photochem. Photobiol. Sci.* **2003,** *2,* 267.

56. McHugh, A.; Gouterman, M.; Weiss, C., Jr., *Theor. Chim. Acta* **1968,** *24,* 132.

57. Barth, G.; Linder, R.; Bunnenberg, E.; Djerassi, C., *J. Chem. Soc., Perkin Trans. 2* **1974,** 696.

58. Seidel, D.; Lynch, V.; Sessler, J. L., *Angew. Chem. Int. Ed. Engl.* **2002,** *41,* 1422.

59. Köhler, T.; Seidel, D.; Lynch, V.; Arp, F. O.; Ou, Z. P.; Kadish, K. M.; Sessler, J. L., *J. Am. Chem. Soc.* **2003,** *125,* 6872.

60. Cox, M.; Darken, J., *Coord. Chem. Rev.* **1971,** *7,* 29.

61. Livingstone, S., *Coord. Chem. Rev.* **1971,** *7,* 59.

62. Duus, F., *J. Am. Chem. Soc.* **1986,** *108,* 630.

63. Carlsen, L.; Duus, F., *J. Am. Chem. Soc.* **1978,** *100,* 281.

64. Carlsen, L.; Duus, F., *J. Chem. Soc., Perkin Trans.* **1980**, *2*, 1768.

65. Andresen, B.; Duus, F.; Bolvig, S.; Hansen, P. E., *J. Mol. Struct.* **2000**, *552*, 45.

66. Hansen, P. E.; Skibsted, U.; Duus, F., *J. Phys. Org. Chem.* **1991**, *4*, 225.

67. Berg, U.; Sandstrom, J.; Carlsen, L.; Duus, F., *J. Chem. Soc., Perkin Trans. 2* **1983**, 1321.

68. Hansen, P. E.; Duus, F.; Schmitt, P., *Org. Magn. Res.* **1982**, *18*, 58.

69. Jorgensen, F. S.; Brown, E. A.; Carlsen, L.; Duus, F., *J. Am. Chem. Soc.* **1982**, *104*, 5922.

70. Jorgensen, F. S.; Carlsen, L.; F. Duus, *J. Am. Chem. Soc.* **1981**, *103*, 1350.

71. Norskov-Lauritsen, L.; Carlsen, L.; Duus, F., *J. Chem. Soc. Chem. Comm.* **1983**, 496.

72. Gonzalez, L.; Mo, O.; Yanez, M., *J. Phys. Chem. A* **1997**, *101*, 9710.

73. Fabian, J., *Tetrahedron* **1973**, *29*, 2449.

74. Doslic, N.; Sundermann, K.; Gonzalez, L.; Mo, O.; Giraud-Girard, J.; Kuhn, O., *Phys. Chem. Chem. Phys.* **1999**, *1*, 1249.

75. Gonzalez, L.; Mo, O.; Yanez, M., *J. Org. Chem.* **1999**, *64*, 2314.

76. Gębicki, J.; Krantz, A., *J. Am. Chem. Soc.* **1981**, *103*, 4521.

77. Gębicki, J.; Krantz, A., *J. Chem. Soc., Chem. Commun.* **1981**, 486.

78. Power, L.; Turner, K.; Moore, F., *J. Chem. Soc., Perkin Trans.* **1976**, *2*, 242.

79. Hatchard, C. G.; Parker, C. A., *Proc. R. Soc. London, Ser. A* **1956**, *235*, 518.

80. Noe, E., *J. Am. Chem. Soc.* **1977**, *99*, 2803.

81. Posokhov, Y.; Gorski, A.; Spanget-Larsen, J.; Duus, F.; Hansen, P. E.; Waluk, J., *Chem. Phys. Lett.* **2001**, *350*, 502.

82. Posokhov, Y.; Gorski, A.; Spanget-Larsen, J.; Duus, F.; Hansen, P. E.; Waluk, J., *ChemPhysChem* **2004**, *5*, 495.

83. Posokhov, Y.; Gorski, A.; Spanget-Larsen, J.; Duus, F.; Hansen, P. E.; Waluk, J., *in preparation.*

84. Alparone, A.; Millefiori, S., *Chem. Phys. Lett.* **2003**, *290*, 15.

85. Michl, J.; Thulstrup, E. W., *Spectroscopy with Polarized Light*. VCH: New York, **1986**.

86. Raabe, G.; Vančik, H.; West, R.; Michl, J., *J. Am. Chem. Soc.* **1986**, *108*, 671.

87. Roubin, P.; Chiavassa, T.; Verlaque, P.; Pizzala, L.; Bodot, H., *Chem. Phys. Lett.* **1990**, *175*, 655.

88. Wehrle, B.; Limbach, H.-H.; Köcher, M.; Ermer, O.; Vogel, E., *Angew. Chem. Int. Ed. Engl.* **1987**, *26*, 934.

89. Völker, S., *Molecular Physics* **1977**, *32*, 1703.

90. Brown, S. B.; Brown, E. A.; Walker, I., *Lancet Oncology* **2004**, *5*, 497.

91. Butenhoff, T. J.; Moore, C. B., *J. Am. Chem. Soc.* **1988**, *110*, 8336.

92. Vogel, E.; Köcher, M.; Schmickler, H.; Lex, J., *Angew. Chem. Int. Ed. Engl.* **1987**, *25*, 257.

93. Sessler, J. L.; Brucker, E. A.; Weghorn, S. J.; Kisters, M.; Schäfer, M.; Lex, J.; Vogel, E., *Angew. Chem. Int. Ed. Engl.* **1994**, *33*, 2308.

94. Kyrychenko, A.; Gorski, A.; Waluk, J., *J. Chem. Phys.* **2004**, *121*, 12017.

95. Шпольский, Э.; Ильина, А.; Климова, Л., **1952**, *87*, 935.

96. Gil, M. Tautomeryzacja w izomerach porfiryny. Ph. D. thesis, Warsaw, **2004**.

97. Гуринович, Г.; Севченко, А.; Соловьев, К., *Оптика и Спектроскопия* **1961**, *10*, 750.

98. Waluk, J., *Acta Phys. Pol. A* **1999**, 95.

The data presented in this thesis have been published so far in the following papers:

1. Gorski, A.; Lament, B.; Davis, J.M.; Sessler, J.; Waluk, J., *J. Phys. Chem. A* **2001**, *105*, 4992.

2. Posokhov, Y.; Gorski, A.; Spanget-Larsen, J.; Duus, F.; Hansen, P. E.; Waluk, J., *Chem. Phys. Lett.* **2001**, *350*, 502.

3. Gorski, A.; Vogel, E.; Sessler, J.L.; Waluk, J., *Chem. Phys.* **2002**, *282*, 37.

4. Gorski, A.; Vogel, E.; Sessler, J.L.; Waluk, J., *J. Phys. Chem. A* **2002**, *106*, 8139.

5. Posokhov, Y.; Gorski, A.; Spanget-Larsen, J.; Duus, F.; Hansen, P. E.; Waluk, J., *ChemPhysChem* **2004**, *5*, 495.

6. Gorski, A.; Kohler, T.; Seidel, D.; Lee, J.T.; Orzanowska, G.; Sessler, J.L.; Waluk, J., *Chem. Eur. J.* **2005**